UNIVERSITÀ
degli STUDI
di CATANIA

Dipartimento
di Fisica
e Astronomia
"Ettore Majorana"

PhD programme in physics

Yara De Leo

The in-flight radiometric calibration of the Metis coronagraph on-board Solar Orbiter. First results from calibrated images.

PhD thesis

Supervisors:

Prof.ssa F. Zuccarello

Dr. L. Teriaca

Co-Supervisors:

Prof. M. Romoli

Dr. D. Spadaro

---

academic year 2022/2023

Contents

Abstract **3**

1 Introduction **5**

1.1 The most external layer of the Sun atmosphere: the solar corona 5

1.2 Brief history of space-based coronagraphs 16

1.3 Solar Orbiter and its scientific goals 22

1.3.1 Solar Orbiter characteristics 22

1.3.2 *Payload* 24

1.3.3 Scientific objectives 26

2 The Metis coronagraph and the observation of the extended solar corona **32**

2.1 Metis scientific objectives and its performances 32

2.1.1 Metis maps and diagnostic techniques 34

2.2 Instrument description 37

2.2.1 The telescope 39

2.2.2 The Metis field of view 43

2.2.3 Metis detectors 44

2.2.4 Electronics 45

2.3 Data processing 45

2.4 Observation planning and Metis operations 47

3 In-flight radiometric calibration of the VL channel of Metis **51**

3.1 Introduction 51

3.2 The VL channel radiometric calibration factor . . . 52
3.2.1 Availability of the stellar targets . . . 53
3.2.2 Aperture photometry . . . 55
3.2.3 The Metis photometric response . . . 58
3.2.4 On-ground calibration . . . 60
3.2.5 Data inversion and calibration across the FoV . . . 61

4 In-flight radiometric calibration of the UV channel of Metis 63
4.1 Introduction . . . 63
4.2 The Metis UV channel radiometric calibration . . . 64
4.2.1 Availability of the stellar targets . . . 64
4.2.2 UVDA dark optimization . . . 66
4.2.3 Vignetting function correction . . . 68
4.2.4 Aperture photometry . . . 68
4.2.5 Metis UV photometric response . . . 69
4.2.6 Correction for spatial disuniformity and data inversion . . . 72
4.2.7 Refining the spatial correction across the FoV . . . 74
4.3 UVDA anomalies . . . 79

5 First analyses of the calibrated data 83
5.1 Comparing coronal VL images of Metis and COR2 . . . 83
5.2 Comparing coronal UV images of Metis and UVCS data . . . 89
5.2.1 Radial profiles of UVCS . . . 89
5.2.2 Average radial intensity profiles of Metis UV images . . . 91
5.3 Six eruptive events seen by Metis . . . 96
5.3.1 Kinematics . . . 98
5.3.2 Intensity radial profiles . . . 100

6 Conclusions 105
6.1 Conclusions . . . 105

Bibliography 116

Acknowledgements 117

Abstract

Solar Orbiter is a space mission with two important unique characteristics: it approaches the Sun with an elliptic orbit, up to a perihelion of 0.28 au, never reached before by solar missions carrying remote-sensing instrumentation, and it will observe the Sun and its atmosphere exiting the ecliptic plane (in 2025, up to about 30° of heliolatitude). It is included in the Cosmic Vision 2015-2025 program of ESA and it is in collaboration with NASA. The launch of the spacecraft happened successfully on 10 February 2020.

One of the scientific goals of the mission is the study of the solar corona, which represents the outermost layer of the solar atmosphere and which extends to the edges of our planetary system (the heliosphere) in the form of solar wind. The heliosphere provides a unique context for the observation of fundamental physical phenomena common to various disciplines such as solar physics, astrophysics, and plasma physics.

The observations of Solar Orbiter are the key for linking the structures of the solar wind to the regions where they originate on the Sun and to achieve one of the scientific objectives of the mission, understanding the mechanism of creation and control of the heliosphere by the Sun, as the results from the Nominal Mission Phase have already shown. This and the other scientific objectives, together with a description of the mission, are the subject of the first chapter of this work.

To achieve its scientific objectives, Solar Orbiter is equipped with 10 instruments, four for in-situ measurements and six for remote-sensing: the second category includes Metis, the coronagraph aboard, which for the first time provides simultaneous maps of the extended solar corona in the two main components of the plasma, hydrogen and electrons. In fact, Metis is equipped with two observation channels, one for measurements of total

and polarized visible light (VL, pass band: 580-640 nm) and the other, the UV channel, in the narrow band at 121.6 ± 10 nm around the H I Ly-α line. In the second chapter, I describe the scientific goals of Metis, its observation channels, and other features of the coronagraph.

My main activity within the Metis team is the development of diagnostic tools useful to perform the radiometric calibration of the two channels and the analysis of acquired data. Thus, the third chapter is dedicated to the radiometric calibration of the VL channel I performed by using star observations, which is fundamental not only for producing calibrated data but also for understanding the performance of the channel. In fact, the radiometric calibration is necessary to obtain the absolute brightness of the solar corona from the imaging data acquired. Furthermore, it allows us to monitor the aging of the channel and to gain information on its *point spread function* (PSF).

In the fourth chapter I describe the radiometric calibration of the UV channel, which exploits the same methodology.

The topic of the fifth chapter is a first analysis of data calibrated using my measurements and results. I show the comparison between the total and polarized VL images of the solar corona acquired by Metis and STEREO-A/COR2 in November 2020 (superior conjunction of the instruments), and similarly, the comparison between the UV images acquired by Metis in 2020-2021 and UVCS aboard SOHO during the activity minimum of solar cycle 22 in 1996. I also describe the study of six eruptive events with exceptionally bright emission in H I Ly-α observed by Metis in 2021.

In the last chapter, I summarize the work carried out and comment on the main results.

Chapter 1

Introduction

1.1 The most external layer of the Sun atmosphere: the solar corona

The Sun is classified as a G2V star[1]. Schematically summarizing its structure, the following parts are indicated, starting from the center: nucleus, radiative zone, and convective zone that ends forming the photosphere.
The temperature is 10^7 K in the nucleus, and then gradually decreases up to approximately 5800 K in the photosphere, where the radiation stops interacting tightly with the plasma and propagates freely into space. In this step the medium becomes from optically thick to thin and the photosphere represents the visible surface of the star.
The solar atmosphere begins above the convective zone and the photosphere, in conjunction with a strong increase in temperature, and it is divided into progressively hotter temperature regions: chromosphere, transition region (TR) and corona (Figure 1.1).
The Sun has a magnetic field generated by a dynamo mechanism inside the star, that, together with the convection, is responsible of the variability and of the periodic cycle of activity.

The corona is historically defined as the part of the solar atmosphere visible during total solar eclipses. Its plasma is a completely ionized mix of: hydrogen (protons), electrons,

[1] Class G stars have a surface (photosphere) temperature between 5,200 and 6,000 K and a mass between 0.8 and 1.04 $M_\odot$, where $M_\odot = 1.989 \cdot 10^{30}$ kg is the mass of the Sun. The Roman letter indicates the luminosity class and in particular the "V" class corresponds to the class of a main sequence star.

helium ($\sim 8\%$) and heavier ions ($\sim 0.03\%$). It is characterized by a temperature of about 1-$2{\cdot}10^6$ K and a density of about 10^9 particles$/\mathrm{cm}^3$ at the base of the corona, which decreases of two orders of magnitude at 1.8 $R_\odot$ from the solar surface. The decrease of the corona density $\mathrm{N_e}$ follows the empirical law:

$$\mathrm{N_e}(\rho) = \mathfrak{C}\left(\frac{1.55}{\rho^6} + \frac{2.99}{\rho^{16}}\right), \tag{1.1}$$

where $\mathfrak{C} = 10^8$ cm^{-3}, $\rho = \frac{r}{R_\odot}$ and r is the distance from the Sun center (Landi degl'Innocenti 2007). It is an optically thin medium.
The rise in temperature of the corona, up to two orders of magnitude higher than for the photosphere, is known as the "coronal heating problem". The currently accepted theories propose explanations based either on the reconnection of the magnetic field lines in the corona or on the transport of energy by magnetohydrodynamic waves which dissipate in the outer solar atmosphere.

The study of the Sun has always been the "Rosetta stone" to interpret the behaviour and the evolution of stars, but its importance has also a direct impact on a knowledge that concerns us much more closely, since the Sun and its activity have a strong impact on the life on Earth. In addition to the more obvious phenomena, such as radiation and climate, the Sun and its transient phenomena are linked to events such as geomagnetic storms, that cause aurorae, variations in the trajectories and damages on artificial satellites (for example, those of our geolocation system).

The field of study that deals with the influence of solar variations on the Earth system is called *space weather* and represents a field on which attention and resources are recently being conveyed. Geomagnetic storms, induced by particularly intense solar phenomena such as flares and *Coronal Mass Ejections* (CMEs), release charged particles that penetrate the Earth magnetosphere and can cause various types of disturbances to human activities: disturbances and/or power outages (mainly in the circumpolar regions), radio communications disturbances (at all latitudes), shifts in satellite orbits and damage to their electronics. Furthermore, they can cause radiation damage to astronauts and to those traveling on transpolar routes, forcing major route changes to airlines, with a consequent increase in operating times and costs.

[2] `https://solar-c.nao.ac.jp/en/science.html`

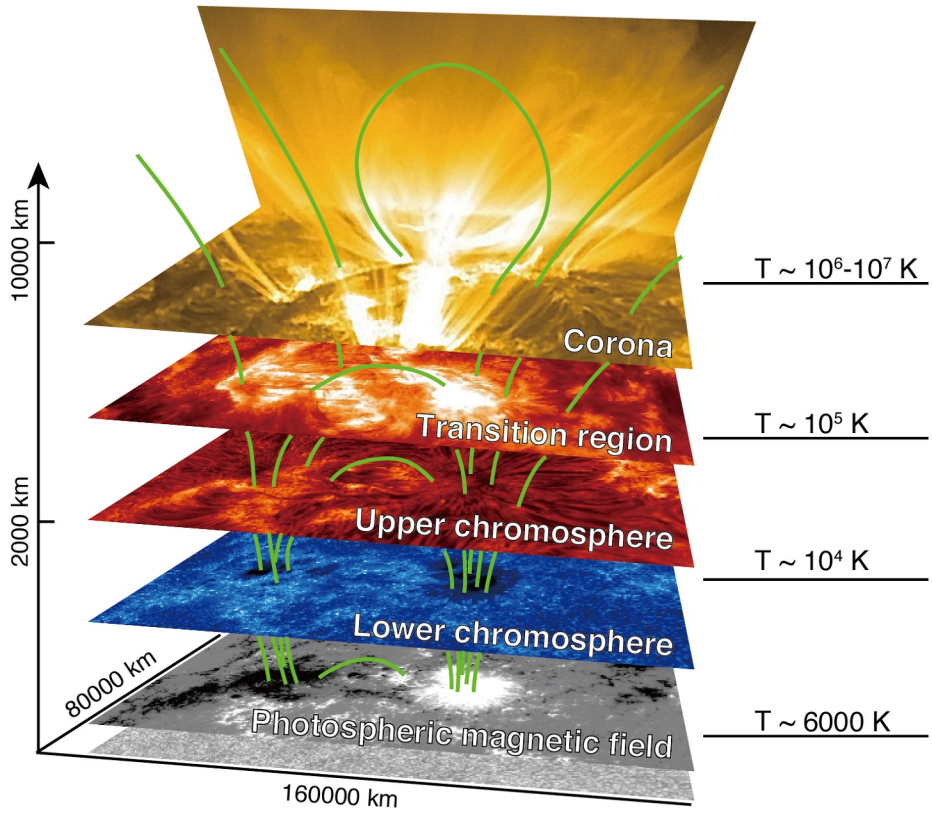

Figure 1.1: The layers of the solar atmosphere from the photosphere: chromosphere, transition region, corona. The structure of the solar atmosphere is connected by magnetic field lines. Image from the SOLAR-C website[2].

In this context, the study of the magnetic field plays a primary role in the analysis of the physics of the Sun and, in particular, of the corona: in the photosphere and in the underlying convective region the field is "dominated" by the plasma (this means that the ionized gas forces magnetic field lines to follow its own motion). Emerging from the photosphere, up to the corona, the situation changes rapidly, the lines of force of the magnetic field trap the plasma, giving rise to the main coronal structures: streamers, coronal holes, prominences and fast transients. The interaction between the magnetic field and the solar plasma is regulated by the parameter β of the solar plasma, defined by the relation:

$$\beta = \frac{P}{P_{mag}} = \frac{8\pi P}{B^2} \tag{1.2}$$

where P is the plasma pressure and $P_{mag}=\frac{B^2}{8\pi}$ is the magnetic pressure. The content of the energy tells us that the plasma dominates the evolution of physical phenomena when $\beta > 1$ (inside the Sun up to the photosphere and in the solar wind). The heterogeneous aspect of the solar atmosphere (chromosphere, TR, and corona) corresponds to the $\beta < 1$ case, where the stratification imposed by gravity is dominated by the structures that follow the magnetic field lines.

The solar corona reaches the boundaries of our planetary system expanding in the form of solar wind. This is a stream of charged particles (electrons, protons and α particles) continuously emitted and accelerated by the Sun that is measured locally by in-situ instrumentation at several distances from the Sun, up to the edges of the solar system (by Voyager 1 and Voyager 2[3]). These measurements did show that the expansion region of the solar wind, known as the "heliosphere", extends to the edges of the solar system and is delimited by a *termination shock* called "heliopause". The heliopause is the theoretical boundary where the dynamic pressure of the solar wind flow is in equilibrium with the thermal pressure of the interstellar medium. The solar wind density in the heliopause is greater than the density of the interstellar medium, as generally it occurs in areas subjected to shocks. The Voyager 1 spacecraft crossed the heliopause in august 2012, at a distance of about 121 au from the Sun: this was indicated by a new measurement of the density of low-energy particles surrounding the probe, which showed a sharp increase compatible with the theoretical predictions of the crossing of the shock front (Krimigis et al. 2013). Voyager 2 crossed the heliopause in 2018 (Burlaga et al. 2019).

Two types of solar wind are distinguished, in relation to different origin zones and propagation speeds (see Figure 1.2):

- the **slow wind**: its origin is still being investigated, but it seems to arise at the boundary of coronal structures with closed magnetic field lines (streamers), at low latitudes during solar minimum; this component is extremely variable, and has an average speed of $300 \div 400$ km/s at 1 au;

[3] Voyager 1 and Voyager 2 are probes sent into space, in 1977, for exploration of the outer solar system (Stone 1977). Both Voyager spacecraft continue to transmit data to Earth stations as they travel out of the solar system. On the 27 March 2023, at a distance of 159.20 au, Voyager 1 is the most distant human-made object from Earth.

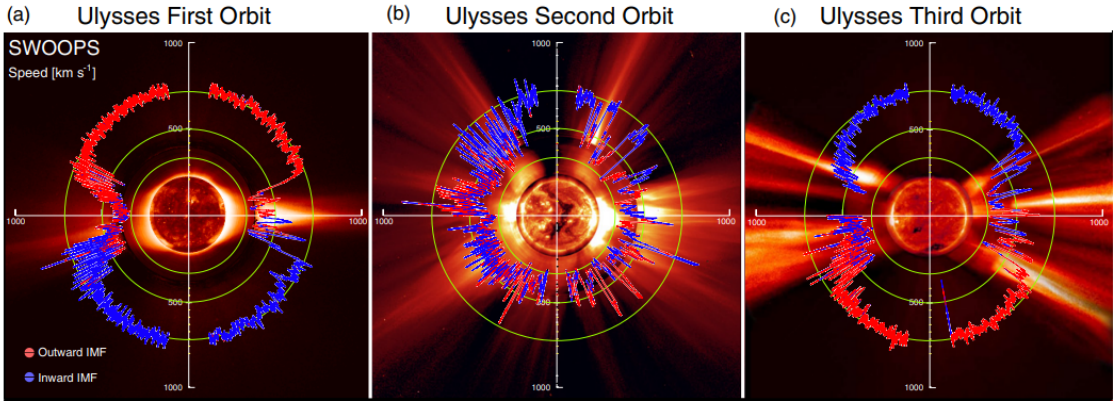

Figure 1.2: Polar plots of the solar wind speed as measured by the *Ulysses* mission. The outward interplanetary magnetic field is in red the inward in blue. The figures displaying the solar and coronal structures are taken from SOHO's Extreme ultraviolet Imaging Telescope, the Mauna Loa K coronameter and SOHO's LASCO C2, on 1996 August 17, 2000 December 7, and 2006 March 28 respectively. Adapted from (McComas et al. 2013) with permission © AAS.

- the **fast wind**: it comes from areas of open magnetic field topology, such as coronal holes, regions present mainly at high heliolatitudes at solar minimum; it is characterized by a greater stability than the slow wind and by a speed of about 700 km/s at 1 au.

In both cases, the physical processes responsible for the solar wind acceleration have yet to be understood.

In solar physics there are characteristic natural times that are very different, for example the time of the solar rotation, with an average value of 28 days, or the period of variation of magnetic phenomena, known as the solar cycle, which is around eleven years.
In addition, the Sun is subject to a differential rotation, it rotates differently depending on the latitude: faster at the equator than at the poles. The rotation period varies between 25 days at the equator and 33 days at the poles. Differential rotation, combined with the convective layer, causes the so-called dynamo effect that perturbs and amplifies the poloidal field of the Sun following a 22 year cycle. The dynamo creates the about 11 years solar activity cycle during which the magnetic field variates from a simpler poloidal configura-

tion (solar activity minimum) to a more complex multipolar configuration (solar activity maximum).

The magnetic flux tubes that forms in the convection zone are brought to the surface by magnetic buoyancy where, being the field divergence free, emerge forming magnetic arcades or loops that connect opposite polarity regions. Loops can be considered as the building blocks of the solar atmosphere and are visible in all magnetically dominated regions of the atmosphere (see Figure 1.3).

The most visible (and longer studied) global manifestation of the activity cycle consists in the variation of the number of sunspots on the surface of the Sun. During the minimum of the cycle the sunspots[4] are practically absent, while in the periods of maximum they cover up to 0.5 % of the visible hemisphere.
The dynamic events that modify the structure of the solar corona develop over time intervals ranging from minutes to days. Thus it is easy to understand that to study the coronal physics is necessary to extend the observation time beyond that allowed by natural total eclipses.

Active regions and coronal holes are the most prominent features of the solar corona. The first are regions of elevated magnetic field concentrations, often including one or more sunspots. They are very bright in the far and vacuum ultraviolet[6] and in X-rays and may host solar flares, the most energetic solar activity events where energies up to 10^{25} J can be released on very short timescales (seconds to minutes). Coronal holes are, on the opposite,

[4]Sunspots are phenomena on the photosphere that appear as temporary spots darker than the surrounding areas. These are regions of reduced surface temperature due to the concentrations of magnetic flux which inhibit convection.

[5]`http://www.jhelioviewer.org/`

[6]For clarity I introduce the nomenclature of the UV band subdivisions here:

- Soft X-ray = 1 – 10 nm
- Extreme Ultraviolet (EUV) = 10 – 122 nm
- Far Ultraviolet (FUV) = 122 – 200 nm
- Vacuum Ultraviolet (VUV = EUV+FUV) = 10 – 200 nm
- Middle Ultraviolet (MUV) = 200 – 300 nm
- Near Ultraviolet (NUV) = 300 – 400 nm

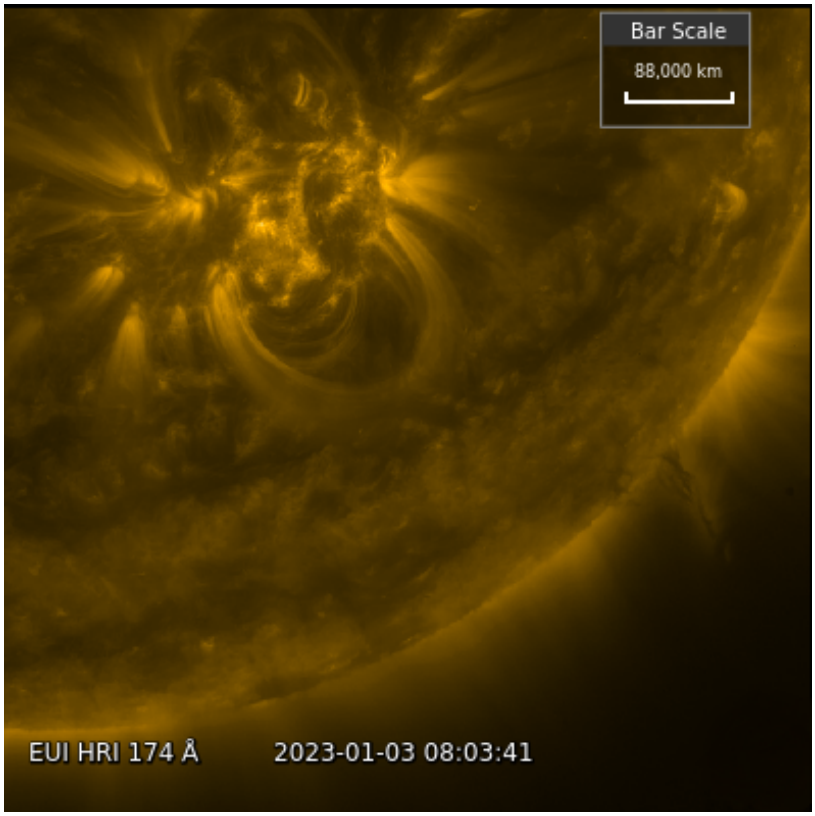

Figure 1.3: Coronal loops complex observed by EUI HRI_{EUV} 174 Å on January 3, 2023, at 08:04 UT. Image created with JHelioviewer[5](Müller et al. 2017).

regions of mostly open and weaker magnetic field that appear dark in the EUV and in X-ray (see Figure 1.5). Large coronal holes appear at the poles of the Sun during solar minimum. The rest of the solar surface is covered by mixed polarity weaker field that forms the so-called “quiet Sun”.

Other large to medium scale phenomena are: sunspots and faculae[7] (in the photosphere of active regions), filaments and plages (cromospheric counterparts of faculae), prominences and flares. Here only the most relevant to this work are mentioned:

- **Prominences and solar filaments**

  They are arch-shaped plasma features, supported by the magnetic field. They grow from the photosphere to the solar corona and reach lengths of about $2{\cdot}10^5$ km in length. There are two types of prominences: “quiescent prominences" and “eruptive

[7]The facula is a bright region of the Sun observed on the photosphere (called *plage* when seen in chromospheric emission), produced by a concentration of magnetic field lines.

prominences". The former are stable and visible for a very long time, more than a week, while the latter disappear in a few hours (a coronal mass ejection is often associated with these). If the velocity of the plasma is lower than a certain value, the prominences can fall back into the solar photosphere, otherwise they disperse into the interplanetary environment. In both cases they have average dimensions of about $3{\cdot}10^4$ km in height above the photosphere and $5{\cdot}10^3$ km in thickness.
Historically, two different names have been attributed to the same phenomenon, due to how it is observed: they are called “bright prominences" when we observe them above the limb of the Sun because they are denser and brighter in Hα with respect to the background. But they are also called “filaments" when they are observed over the solar disk because they are darker than the background. Magnetometric measurements show that the filaments are positioned along a neutral line of the magnetic field. For more details see also the review by Parenti 2014.

- **Flares**
  They are sudden increases of the radiation and take place in active regions (regions overlying sunspots where strong magnetic fields connect the photosphere to the corona), but they affect all layers of the solar atmosphere. The energy released by flares can be of the order of 10^{25} J. They are caused by phenomena of reconnection of magnetic field lines. An earlier flare classification in intensity was based on Hα spectral observations. That scheme uses both the intensity (’f’-faint,’n’-normal,’b’-brilliant) and emitting surface. The modern classification system for flares uses letters (A, B, C, M, X) according to the peak flux in watts per square metre in defined soft X-rays band passes. See also the review by Benz 2017.

- **Coronal Mass Ejections (CMEs)**
  These are spectacular features, often associated with flares, in which large quantities of plasma are expelled (see Figure 1.4). These events produce a mass ejection of the order of 10^{12}kg - 10^{14}kg. The speed of the plasma is between 20 km/s and 3200 km/s with an average speed of 500 km/s. During periods of maximum solar activity the rate of CMEs is more than one event/day, while during solar minimum the rate is 0.1 - 0.2 event/day. A further description of these phenomena is also reported in Section 5.3. Comprehensive reviews about the topic can be found in Chen 2011, Kilpua et al. 2017 and Webb & Howard 2012.

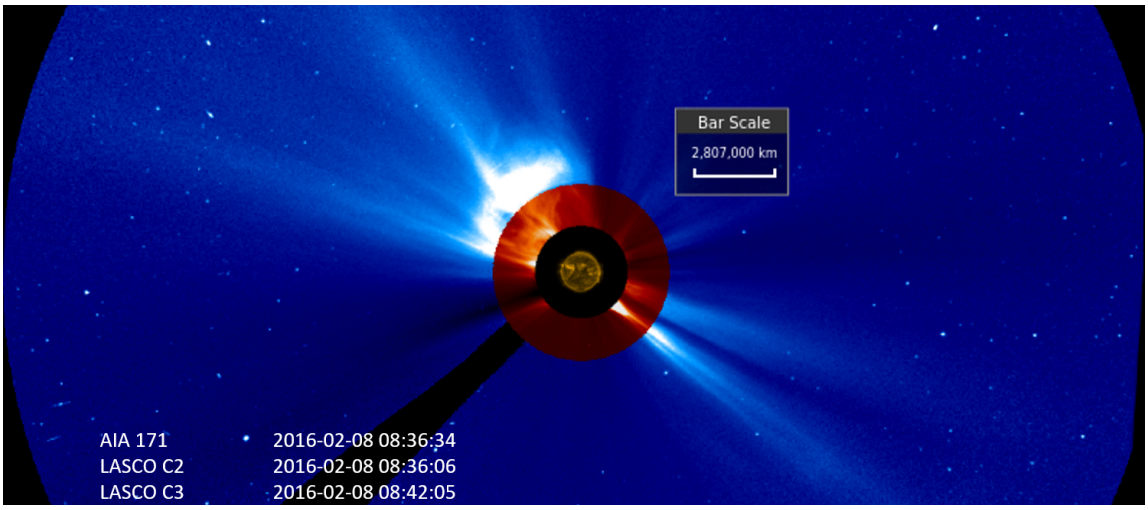

Figure 1.4: Spectacular CME observed by SDO/AIA 171 and SOHO/LASCO-C2 and C3 on February 8, 2016, at around 08:36 UT. Image created with JHelioviewer (Müller et al. 2017).

- **Streamers**

  They are luminous arch-shaped structures that develop above the active regions of the Sun. They correspond to a magnetic field topology with closed lines, which trap the plasma in shapes resembling plumes.

  They constitute the brightest stable coronal structure; they are variable in height and can reach tens of solar radii in altitude. Their density is from 3 to 10 times greater than that of the average solar corona surrounding them (see Figure 1.6).

  The acceleration of the slow wind happens in correspondence of the boundaries of these structures. See also the review by Koutchmy & Livshits 1992.

- **Coronal holes**

  As briefly mentioned before, coronal holes are regions in which there is substantially reduced coronal emission and appear dark in the images, since both their density and temperature are lower than those of the solar corona. These zones are associated with a topology of open magnetic field lines. During solar minimum the coronal holes are found in the polar regions of the Sun, while during solar maximum they are small and sometimes present in equatorial regions. From these features, the fast component of the solar wind originates (see the review by Cranmer 2009).

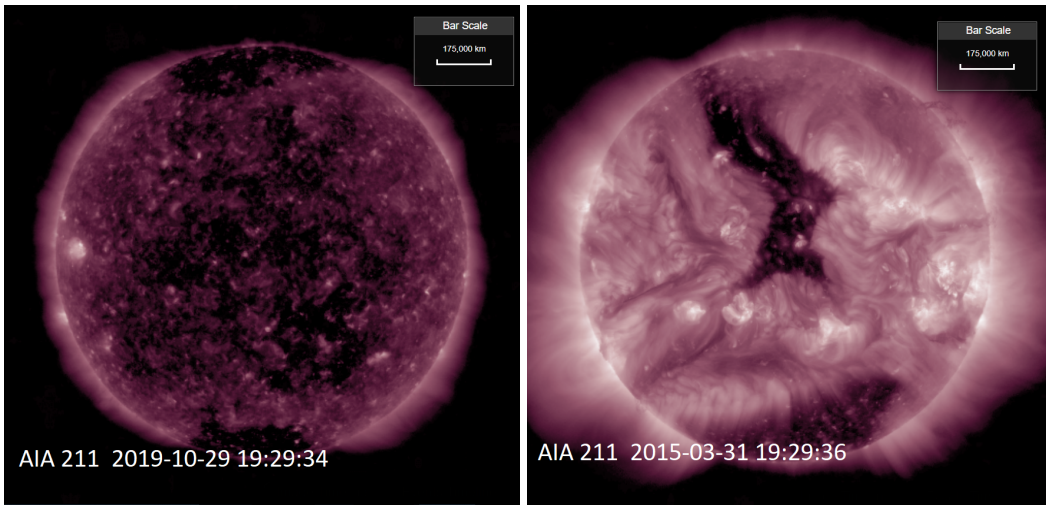

Figure 1.5: The Sun disk observed by SDO/AIA 211 during solar minimum (left panel) and during solar maximum (right panel). At solar minimum two coronal holes are visible at the poles, while in the image of the solar maximum a large equatorial coronal hole is present. Images created with JHelioviewer (Müller et al. 2017).

The solar corona is extremely dynamic and in continuous expansion, it does not follow the spherical symmetry characterizing the innermost regions of the Sun and varies with the solar activity. During minimum periods the visible light corona has a reduced extension, with streamers extending at low latitudes (see left panel Figure 1.6). On the other hand, in periods of maximum the corona has a more complex shape with streamers at all latitudes (see right panel of Figure 1.6).
From an observational point of view, two types of the extended corona visible during eclipses are historically distinguished in the visible light (VL) spectrum, a continuous spectrum called “K corona" and a line spectrum called “E corona". The F corona is superimposed on these components, but it is generated, like the zodiacal light, by the interplanetary dust.

- **K corona**

  It is predominant up to 2-3 $R_{\odot}$, and is the brightest coronal component during a total solar eclipse. It has a continuous spectrum (*Kontinuierliche*, hence the initial

[8] `http://www.zam.fme.vutbr.cz/~druck/`

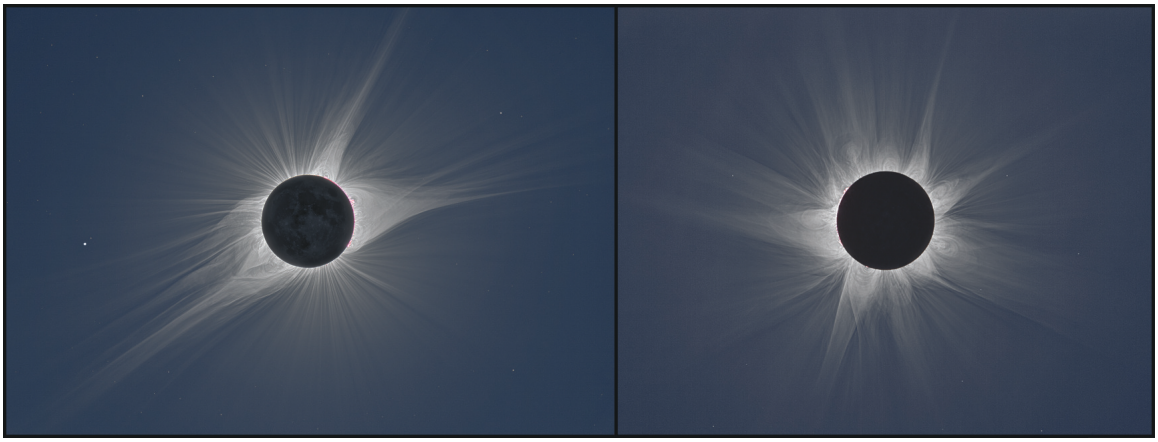

Figure 1.6: Left panel: corona observed from Earth during solar minimum (solar eclipse of 2017, Whiskey mountain, Wyoming, USA). Right panel: corona during solar maximum (solar eclipse of 2012, Queensland, Australia). Credits: Miloslav Druckmüller [8].

"K") and is partially linearly polarized. Its brightness is due to the photospheric radiation scattered by free electrons due to the Thomson effect[9]. Due to their coronal temperature, 10^6 K, they move at an average speed of $5{\cdot}10^3$ km/s; this speed causes a Doppler broadening of the absorption lines of the photospheric spectrum sufficient to make the absorption line disappear from the spectrum, hence the name "continuous". The electron density decreases as the distance increases, from $5{\cdot}10^8$ cm^{-3} at the base of the corona, by two orders of magnitude at a distance from the surface of about 1.8 $R_\odot$.

- **E corona**

  This is a component due to the emission lines (hence corona "E") of highly ionized ions such as Fe, Ni and Ca. The intensity of this corona, like for K corona, decreases very rapidly with increasing solar distance. In the visible band pass the so-called "green" (FeXIV, 530.3 nm), "yellow" (CaXV, 569.4 nm), "red" (FeX, 637.4 nm) and "infrared" (FeXIII , 1074.7 nm) spectral lines are particularly intense.

- **F corona**

  F corona dominates starting from 2-3 $R_\odot$ especially in the plane of the ecliptic, the

[9] *Thomson scattering* is an elastic scattering of electromagnetic radiation by a free charged particle. The electromagnetic field of the incident wave accelerates the particle causing the emission of radiation at the same frequency as the incident wave along a random direction.

spectrum is the photospheric one with the presence of Fraunhofer lines (hence the name of "F" corona) and is weakly polarized. Its brightness is due to the scattering of photospheric light by dust particles (Mie scattering and diffraction) of the interplanetary medium; this component decreases very slowly as the solar distance increases. The average speed of the dust particles is much lower than that of the electrons, since particles are more massive and colder, so the Fraunhofer lines are preserved in the scattering of photospheric light.

Figure 1.7 shows the trends of these components in the visible light.

The depiction of the solar corona in this section summarizes contents of general knowledge with the aim of introducing this thesis work, for a better description of the topic please see Landi degl'Innocenti 2007, Carroll & Ostlie 2007 and Stix 2002.

1.2 Brief history of space-based coronagraphs

The first studies of the solar corona, in visible light, took place during total solar eclipses. They were limited in time as total solar eclipses are short in duration (7 minutes maximum). Furthermore, if we consider that this type of eclipse occurs every 18 months on average and that most of them happens over the oceans, we understand the difficulty in documenting them. Scientifically exploitable eclipses occur every two to three years.
In 1930 the French astronomer Bernard Lyot devised the coronagraph, an instrument capable of simulating solar eclipses by means of an opaque disk, called the occulter, positioned on the focal plane of the primary objective of a telescope (Lyot 1939).
The occulter blocks the photospheric radiation of the Sun as the Moon does during a total solar eclipse. This allows the corona to be observed continuously and, from space, in all wavelengths.
Lyot's instrument undoubtedly represented a breakthrough in coronal physics, but unfortunately ground-based observations are limited by the diffused sunlight from the atmosphere (as can be seen from the "Blue sky" level in Figure 1.7) (Shopov et al. 2008). The only currently operational ground-based coronagraph is located on Mauna Loa in Hawaii. The radiance of the clearest sky (like in certain high mountain astronomical sites) allows to reveal the corona up to 1.5 $R_\odot$ at the most: observations from space overcome the problem.

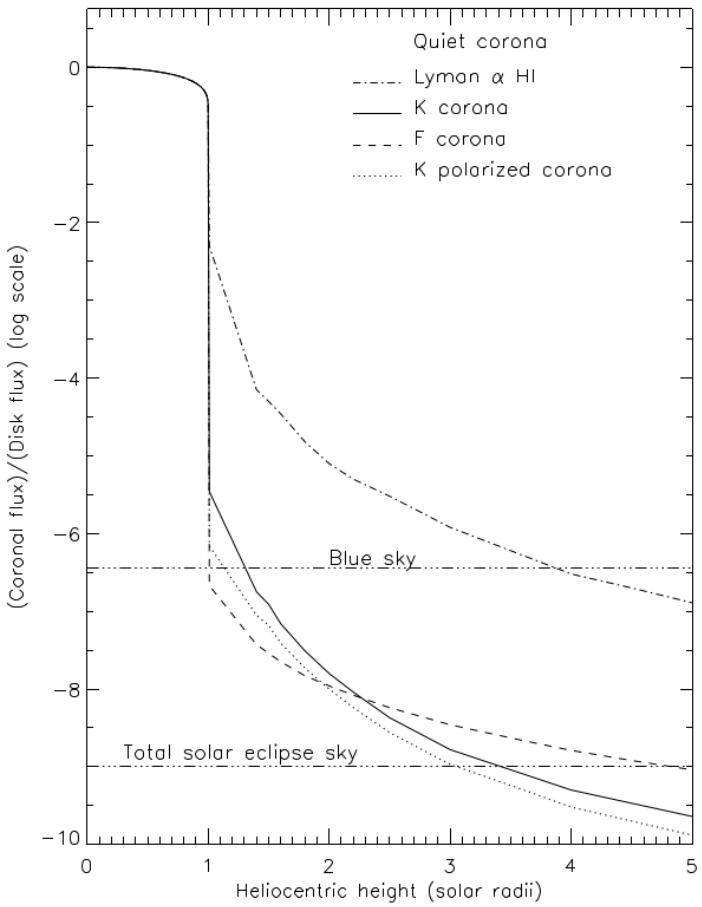

Figure 1.7: Intensity of the solar disk and of the corona components with respect of heliocentric heights in solar radii. Courtesy of Marco Romoli.

Due to its temperature, the corona has a maximum emission at X and EUV wavelengths. These are spectral bands absorbed by the Earth's atmosphere, and therefore the use of space telescopes is required. Space coronagraphs allow us to observe the outer corona.
There are two categories of coronagraphs, distinguished according to the position of the occulter: in the *internally occulted* coronagraphs the occulter is placed downstream of the primary objective, while in the *externally occulted* ones the occulter is in front of the primary objective.

The first observation of the solar disk in the ultraviolet was carried out on 10/10/1946 by means of a US sounding rocket launched (Durand et al. 1949). The rocket reached a height of 175 km. However, this kind of experiments had a limit: the observations lasted only few minutes.

In the early '60s Newkirk and Eddy created the first space coronagraph: by means of an aerostatic balloon they sent the instrument about 25 km high (it was an externally occulted coronagraph) (Newkirk & Eddy 1962). Unfortunately the instrument was not optimized to reduce the stray light from the edges of the optical elements, and therefore the experiment failed. The lesson learned was a hint for a group of the *Naval Research Laboratory* (NRL), which in 1963, under the guidance of R. Tousey, obtained the first image of the extended corona without an eclipse. The instrument was a small rocket borne externally occulted coronagraph.

The OSO-2 (*Orbiting Solar Observatory*) satellite provided the first images of the Sun in VUV, in 1965. Then OSO-3 and OSO-4 performed the Sun imaging in coronal lines (e.g., Mg X) for the first time. The first coronagraph capable of monitoring the corona for a long period of time flew aboard the OSO-7 satellite: it was in orbit around the Earth from October 1971 to June 1974 and yielded the first observation of a CME (Koomen et al. 1975).

On board the first Skylab space station, launched on 14/5/1973 and re-entered the atmosphere on 11/7/1979, the various crews took images of 8 solar flares, confirming the existence of coronal holes. They observed the transition region and the ultraviolet emissions

of the solar corona. These studies were carried out by using eight instruments on board the station including a white light coronagraph, externally occulted, built by the *High Altitude Observatory* (HAO). Thanks to it, about 35000 photos of the solar corona were collected, far more than what had been cataloged since the beginning of the observations up to that moment (MacQueen 1974; MacQueen et al. 1974, 1976).

The Solar Maximum Mission, SMM or SolarMax (Chipman 1981), was launched on 14/2/1980 and re-entered the atmosphere on 2/12/1989. The experiment studied flares and showed that during the maximum of the solar cycle, when the number of sunspots reaches its peak, the Sun is as bright as during the minimum (if not more). This is because the spots are surrounded by brighter structures than the disk, the faculae, which basically reverse the dimming effect of the sunspots themselves. This mission continued the research on the physical properties of coronal eruptions using the NRL's white light coronagraph (MacQueen et al. 1980). This instrument, flown on the SMM, was based on the optical design of the Skylab one, with the addition of some improvements including the use of a *Vidicon*[10] in place of the photographic plate. Thanks to a repairing mission in 1984, SMM remained active until 1989, collecting a large amount of data.

The first coronagraph which used a *Charged Coupled Device* (CCD) detector was a VL externally occulted one (Fisher & Guhathakurta 1994), which remained in orbit for 40 hours on the Spartan-201 mission in 1993. The Spartan (Kohl et al. 1995b) was launched four times, the first and third mission coincided with the passage of Ulysses[11] on one of the solar poles.

The VL coronagraph of the Spartan-201 mission was accompanied by a prototype of the *Ultraviolet & Visible-light Coronagraph Spectrometer* (UVCS), the coronagraph-spectrometer aboard the *SOlar & Heliospheric Observatory* (SOHO) (Domingo et al. 1995).

[10]The Vidicon tube was a type of vacuum tube and was used for the production of digital images.

[11]The probe Ulysses went, for the first time, to study the polar regions of the Sun. It was launched in 1990 and thanks to the slingshot effect of the planet Jupiter Ulysses left the plane of the ecliptic and reached an orbit with a nearly 90° inclination with respect to this plane. This orbit was specially achieved in order to analyze in-situ the plasma emanating from the polar regions of the Sun. The mission obtained important results on the nature of the solar wind, revealing the two regimes, fast and slow (see Figure 1.2).

UVCS was the first instrument to obtain VUV spectra of the extended corona emission.
SOHO was launched in 1995 and is still partially operational. The spacecraft carries 12 instruments for observing the Sun and for detecting solar wind particles; it is stationed in a gravitationally balanced orbit around the Lagrangian point L1, allowing uninterrupted observation of the Sun, and has literally rewritten solar physics.
The set of coronagraphs that compose the *Large Angle Spectrometric COronagraph* suite (SOHO/LASCO) (Brueckner et al. 1995), have made continuous observations of the corona, between 2 and 30 $R_{\odot}$, and have allowed to monitor coronal activity without interruption since 1996. The major contributions have been obtained in the study of the propagation and evolution of coronal eruptions beyond 2 $R_{\odot}$. The high sensitivity of the instruments and the continuity of observation have also allowed to systematically record the weak *halo* eruptions, which are those directed towards the Earth, which can induce geomagnetic storms when they collide with our magnetosphere. LASCO's coronagraphs have contributed to the study of slow solar wind physics through coronal tracers.
Aboard SOHO there is also the *UltraViolet Coronagraph Spectrometer*, UVCS (Kohl et al. 1995a), shut down in 2013. It made it possible to measure the profiles of many coronal VUV lines, including the hydrogen lines Ly-α and Ly-β and the O VI doublet lines (103.2 and 103.7 nm).

In general, the spectrum contains much more information about the plasma than the images alone and this is particularly true for the extended solar corona observed by UVCS. If the plasma has high density, then there are very frequent collisions between the various atoms, ions and electrons. These collisions create a state of equilibrium between the different types of particles, which share their energy and reach common speeds and temperatures. However, the outer solar corona has a very low density, so collisions are so rare that each type of particle can have its own speed and temperature, depending on the process that is accelerating or heating it. Lines ratios and measurement of the spectral line profiles permit to obtain numerous physical parameters of the coronal plasma, for example the temperature. Withbroe's work (Withbroe 1972) makes use of the latter UV spectroscopy diagnostics to determine the ion temperature (e.g., from H I Ly-α line).

The SOHO mission was carrying also a set of helioseismological instruments to measure continuously the oscillations of the Sun in order to reveal the elusive g-modes.

A further step in the study of solar eruptions was possible thanks to the coronagraphs aboard the twin spacecrafts *Solar TErrestrial RElations Observatory* (STEREO, Kaiser et al. 2008), launched on 26/10/2006 (only STEREO-A still operational at the time of writing). STEREO consisted of two twin spacecraft which, moving along the Earth's orbit (one faster and one slower than Earth), did observe the corona from different points of view, allowing the reconstruction of the three-dimensional structure of the coronal eruptions and the corona. The STEREO coronagraphs compose the *Sun Earth Connection Coronal and Heliospheric Investigation* (SECCHI) suite (Howard et al. 2000), and perform the imaging and stereoscopy in total and polarized visible light from 1.5 $R_\odot$ up to 15 $R_\odot$.

In 2009, a sounding rocket carrying the *HElium Resonant Scattering in the Corona and HELiosphere* (HERSCHEL) instrument suite was successfully launched. The payload included a coronagraph devoted to the observation of the corona in the He II 30.4 nm line (HeCor) and a prototype of the Solar Orbiter/Metis coronagraph (SCORE, *Sounding CORonagraph Experiment*), capable of making multiband images (VL, H I Ly-α at 121.6 nm and He II at 30.4 nm) of the extended corona (Romoli et al. 2007). The mission produced the first global map of the solar corona in the He II line (Moses et al. 2020).
HERSCHEL performed the first measurements of the helium abundance in corona (and therefore in the solar wind), based solely on the detected intensity.
Both the He II Ly-α 30.4 nm and H I Ly-α 121.6 nm emission lines are mainly formed by resonant scattering[12] of the chromospheric radiation by the atoms present in the corona. The scattering efficiency depends on the number density of the particles along the line of sight (LoS), and on the intensity of the chromospheric radiation. Furthermore, the efficiency decreases proportionally to the plasma outflow speed. In fact, in a static atmosphere the central wavelength of the coronal absorption is identical to that of the chromospheric emission; whereas with the expanding plasma the excitation profile is shifted by the Doppler effect with respect to the absorption wavelength and thus the diffusion process is less efficient: this means a lower intensity of the coronal line.
The effect just described is known as *Doppler dimming* (Noci et al. 1987) and allows us to measure the speed of the solar wind. The influence of Doppler dimming on a line gener-

[12]The atoms of the extended corona are excited by radiative or collisional mechanisms: the re-emission of radiation occurs by spontaneous de-excitation. The resonant scattering is when an ion (or an atom) radiatively excited re-emits energy at the same wavelength of the incident radiation.

ated by resonant scattering can be determined on the basis of the relationship between the intensity of that line and the intensity of the K corona in the VL (see Section 2.1.1).

Although each of these missions had a specific goal, none of them was able to fully explore the region where the solar wind originates and where heliospheric structures form. This is one of the goals of the Solar Orbiter mission.

1.3 Solar Orbiter and its scientific goals

Following the great success of the SOHO mission, described in the previous section, and the extraordinary step forward in our understanding of the Sun, it was clear to the scientific community that the next required step was to observe the atmosphere of the Sun from different view points: closer to the Sun, to obtain high resolution images of the solar structures while probing the plasma coming from them before its properties could evolve significantly; from above the ecliptic plane, to get a better look at the polar regions of the Sun which are largely unobservable from Earth. The Solar Orbiter mission profile fulfills these requirements.
Another mission devoted to the study of the solar corona and of the solar wind by taking in-situ measurements from distances very close to the regions where the acceleration processes take place is *Parker Solar Probe* (PSP, Fox et al. 2016), a NASA mission launched in august 2018. The orbit of PSP is in the ecliptic plane and already at the end of 2018 the probe reached an eccentric orbit with a perihelion distance of about 10 $R_{\odot}$. The primary science goals for the mission are to track the flow of energy, understand coronal heating, and explore what accelerates the solar wind. PSP does not carry remote-sensing instruments observing directly the Sun. The observations of this probe can be coordinated with those of Solar Orbiter in order to have a global understanding of our star.

1.3.1 Solar Orbiter characteristics

Solar Orbiter is the first mission that will go out of the ecliptic plane (reaching about 33° of heliolatitude, with an elliptical orbit) and approach the Sun reaching 0.28 au. It was conceived to explore, for the first time, both the poles of the Sun and the circumsolar

Parameter	Value
Total mass	1800 kg
Science payload mass	209 kg
Dimensions	2.5 m x 3.1 m x 2.7 m
Total length with solar arrays deployed	18 m
Solar panels	6, each 2.1 m x 1.2 m
Payload power	180 W
Instrument boom	4.4 m
3 × radio and plasma wave antennas	6.5 m each
Probe orientation	pointed to the Sun
Telemetry band	Dual X-band
Data downlink	150 kbit/s (at 1 au)
Launch	10 February 2020 04:03 UTC
Vehicle	Atlas V 411
Perihelion	0.28 au
Maximum heliolatitude	18°(nominal mission) 33° (extended mission)
Nominal mission duration	7 years (including *Cruise phase*)
Extended mission duration	3 years

Table 1.1: Parameters of the Solar Orbiter mission (García Marirrodriga et al. 2021, Müller et al. 2020).

regions. The Solar Orbiter mission is a collaboration of ESA and NASA and is the first mission of ESA's Cosmic Vision 2015-2025 program (Müller et al. 2013).

Solar Orbiter points the Sun, is stabilized on three axes and has a heat shield to protect the payload from the harsh radiative environment. The solar arrays provide the required power throughout the mission over a wide range of distances from the Sun and they can be rotated around their longitudinal axis to manage their temperature, especially as they approach the Sun. A high-gain antenna provides nominal communication with ground stations while one medium-gain antenna and two low-gain antennas are used as backup. Table 1.1 summarizes the Solar Orbiter spacecraft and mission characteristics.

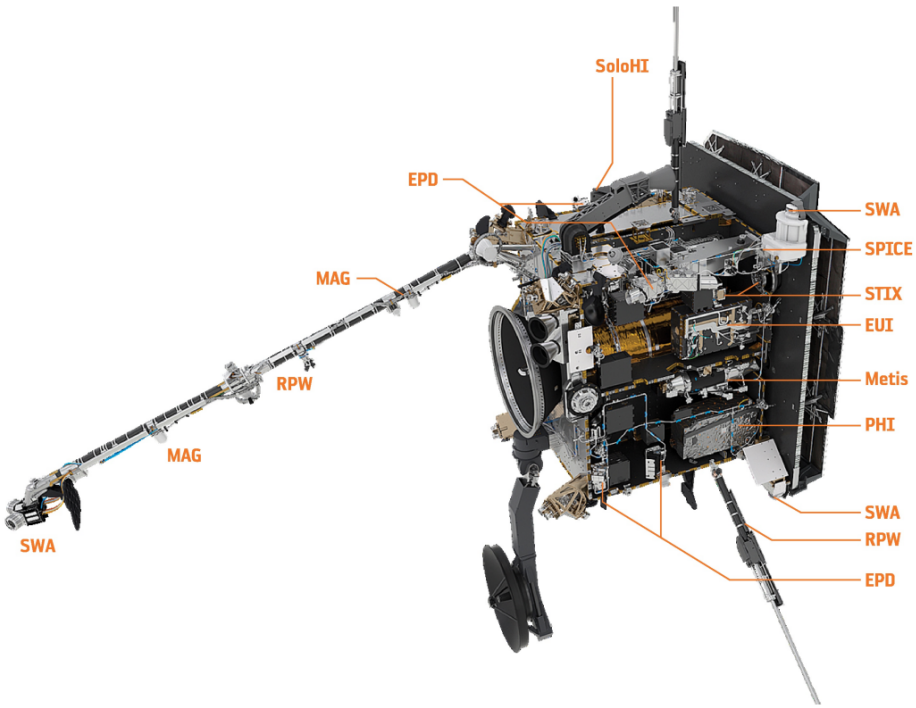

Figure 1.8: Payload of the Solar orbiter mission (Müller et al. 2020)[13].

1.3.2 *Payload*

The Solar Orbiter scientific payload consists of four instruments for *in-situ* measurements and six *remote-sensing* instruments. Figure 1.8 shows the instruments location aboard (Müller et al. 2020).

The in-situ instruments are:

- *Energetic Particle Detector* (EPD, Spain, Rodríguez-Pacheco et al. 2020). It measures the properties of superthermal ions and energetic particles in the energy range of a few keV for relativistic electrons and high energy ions (100 MeV protons, 200 MeV heavy ions).

- *Magnetometer* (MAG, United Kingdom, Horbury et al. 2020). It provides detailed in-situ measurements of the heliospheric magnetic field.

- *Radio and Plasma Wave analyzer* (RPW, France, Maksimovic et al. 2020). It measures both magnetic and electric fields with high time resolution and determines the

[13]Taken from Müller et al. 2020 with permission © ESO.

characteristics of electromagnetic and electrostatic waves in the solar wind up to 20 MHz.

- *Solar Wind Analyzer* (SWA, UK, Owen et al. 2020). It characterizes the main constituents of the solar wind plasma (protons, α particles, electrons, heavy ions) between 0.28 and 1.2 au.

The remote-sensing instruments are:

- *Extreme Ultraviolet Imager* (EUI, Belgium, Rochus et al. 2020). It is composed by three telescopes. Two telescopes observe the Sun (one in H I Ly-α and the other in the EUV around 17.4 nm) with high spatial and temporal resolution, the third telescope observes the full disk and the low solar corona either around 30.4 nm (He II Ly-α) or around 17.4 nm (Fe IX-X) via a filter wheel, to provide a coverage starting from the chromosphere.

- *Metis* (Italy, Antonucci et al. 2020). It is the coronagraph aboard Solar Orbiter. It performs imaging of the extended corona from 1.6° to 2.9°, in polarized brightness (*pB*) and total brightness (*tB*) in broad band between 580 and 640 nm and in HI Ly-α (121.6±10 nm) narrow band.

- *Polarimetric and Helioseismic Imager* (PHI, Germany, Solanki et al. 2020). It provides high-resolution and full-disk measurements of the photospheric magnetic field and the solar photosphere LoS velocity and continuum intensity.

- *Solar Orbiter Heliospheric Imager* (SoloHI, USA, Howard et al. 2020). It is a visible light telescope, copy of the SECCHI/Heliospheric Imager (HI) currently flying on the STEREO mission. It tracks density fluctuations in the inner heliosphere by looking at visible light scattered by electrons in the solar wind.

- *Spectral Imaging of the Coronal Environment* (SPICE, ESA, SPICE Consortium et al. 2020). This instrument characterizes spectroscopically the plasma properties of the solar atmosphere, in two bands 70.4 – 79.0 nm and 97.3 – 104.9 nm.

- *Spectrometer/Telescope for Imaging X-rays* (STIX, Switzerland, Krucker et al. 2020). It will provide spectroscopic images of solar thermal and non-thermal X-ray emission in the range 4-150 keV.

1.3.3 Scientific objectives

Despite many and continuous improvements in understanding the mechanisms governing the solar corona and its dynamics, none of the previous missions has been able to fully explore the region where the solar wind originates and where heliospheric structures are formed. A detailed description of the Solar Orbiter science can be found in (Müller et al. 2013) and (Müller et al. 2020) and in the references therein, thus in this work I only summarize the main important scientific objectives focusing on the Metis contribution.
The Solar Orbiter mission, thanks to the powerful combination of in-situ and remote-sensing instruments, has the aim of answering the scientific central question: How does the Sun create and control the heliosphere?
Answering this fundamental question also means addressing the four interconnected scientific questions, all highly relevant to the theme of the *Cosmic Vision* programme (from Müller et al. 2013):

1. What drives the solar wind and where does the coronal magnetic field originate from?
2. How do solar transients drive heliospheric variability?
3. How do solar eruptions produce energetic particle radiation that fills the heliosphere?
4. How does the solar dynamo work and drive connections between the Sun and the heliosphere?

To answer the first question Solar Orbiter measures, in-situ, both the plasma of the solar wind and the magnetic field and at the same time it carries out measurements of the photosphere and the corona with the remote-sensing instruments. This allows to correlate the properties of the solar wind (velocity, mass flow, composition, charge states and wave amplitudes), measured in-situ, and those measured in corona.
The spacecraft observes, for several days, during the quasi-corotation periods, the different regions of origin of the solar wind: active regions, quiet Sun and coronal holes.
Solar Orbiter can also determine magnetic connectivity by measuring energetic electrons, X-rays and radio emissions. These measurements trace magnetic field lines that have crossed the spacecraft's trajectory back to the the regions on the Sun where they have origin.

The measurements of the photospheric magnetic field, together with those in-situ, allow to reconstruct the coronal magnetic field by extrapolation with well-defined boundary conditions.

EUV imaging and spectroscopy provide the diagnostics needed to characterize the state of the plasma in coronal structures. They can indicate magnetic reconnection in the solar transition region and corona by observing jets[14] and other explosive events.

By combining in-situ and remote-sensing data it is possible to determine the relative contribution of plumes, jets and spicules[15] to the fast wind .

Metis provides global maps of the hydrogen flux velocity, by applying the *Doppler dimming* technique to the component of the outer corona emission line, H I Ly-α at 121.6 nm (see also Section 2.1.1), thus providing information on the coronal acceleration, for the principal component constituting the solar wind (protons).

Furthermore, the large overlap between EUI's Full-Sun Imager (FSI) and Metis helps to connect off-disc coronal structures to the lower corona. Anyway, from an operational point of view this is the most difficult science goal to achieve because the right region of the Sun to be observed has to be pre-selected. This means that precursor observational data (called low-latency data) and the runnings of connectivity models are needed.

The Sun exhibits many transient phenomena such flares, CMEs, eruptive prominences and shock waves (see also Section 1.1). Many of these directly affect the structure and dynamics of the solar wind and, consequently, the Earth's magnetosphere and upper atmosphere. To answer the second question: "How do transient solar phenomena drive heliospheric variability?" Solar Orbiter has many ways to track the changes related with the solar transients. Combined observation of SO/PHI, EUI, SPICE and STIX provide information about the boundary condition of the beginning expansion phase of a CME, while the in-situ in-

[14] Coronal jets are transient, small-scale, surges of plasmas occurring in the solar atmosphere. During a typical event, about 1x10^9 kg of matter is ejected at speeds reaching 400 km/s in a matter of minutes. The jets are believed to contribute significantly to the stream of mass constantly ejected from the Sun, known as the solar wind.

[15] A spicule is a dynamic jet about 500\1000 km in diameter on the surface of the Sun moving at a speed of about 20\50 km/s from the photosphere. They can reach a height of 15,000 km. Spiculae have an average life of just 5-10 minutes; appear elongated and are usually associated with regions of high magnetic flux. Their mass flux is about 100 times greater than that of the solar wind, meaning that even if only a tiny fraction could escape into the wind, they may play an important role in the solar wind.

struments can measure the physical parameters of *interplanetary coronal mass ejection* (ICMEs) when they pass the spacecraft. In principle the imaging spectrograph SPICE can be used to determine the composition of the CMEs in the lower corona and the energy partition within a CME, once released, although the probability that SPICE can observe a CME is very low. Metis can observe in detail how CMEs expand and rotate (see also Section 5.3).

To fully understand the physical system surrounding the CMEs ejection, their shocks and current sheets[16], they must be monitored from their formation in the corona to their expulsion in the solar wind. During the phases of the mission in which the spacecraft is approaching the Sun, Solar Orbiter continuously observes individual active regions for periods longer than those possible from Earth orbit, thus it is able to monitor the development of magnetic fields and to track the flux of magnetic energy in the corona.

Solar Orbiter can even diagnose the magnetic connectivity of the solar wind and CME plasma by using measurements of energetic particles: these flow rapidly along the magnetic field from the Sun and indicate whether a tube of magnetic flux is connected to the Sun at one end, at both ends, or not at all. Suprathermal particles disappear if the field is completely disconnected or may flow in the reverse direction if an interchange reconnection happens. Parker Solar Probe can also provide simultaneous measurements to complete the scenario.

Distribution and temporal variation of the plasma parameters such as density, temperature and magnetic field are necessary to study the formation and the evolution of shocks throughout the corona. Remote-sensing measurements, in particular electron density maps, provide improved coronal plasma models, thus the Alfvén velocity and magnetic field direction can be reconstructed over the distance from the Sun to the spacecraft. Remote-sensing also provide observations of shock drivers such as flares and manifestation of CMEs (waves and dimmings) in the low corona with high resolution (few hundred km) and high cadence (few minutes). The passage of a CME produces shock-accelerated electron beams and, consequently, a warning of a shock approaching the in-situ instruments. The in-situ measurements can fully characterize the upstream and downstream plasma and

[16] A current sheet is an electric current confined to a surface (rather than in a volume of space). The increasing energy density of the magnetic field in current sheets can store energy in plasma. Strong current sheets are sources of many instabilities in plasma, they cause magnetic reconnection with a rapid release of the stored energy. This process is the cause of solar flares, for instance.

magnetic conditions and so the shocks themselves.
Thanks to Solar Orbiter's proximity to the Sun, measurements of the plasma, electric field and magnetic field are not contaminated by the dynamical wind interaction pressure effects due to solar rotation. Thus the first reliable data on the magnetosonic velocity, spatial variation, plasma pressure and magnetic field variation in the inner heliosphere can be provided.

The Sun is the most powerful accelerator of particles in our solar system. It routinely produces energetic particle radiation at speed close to the speed of light, sufficiently energetic to evade the protection of the Earth's magnetosphere and atmosphere and be detected on ground.
For the third question: "How do solar eruptions produce energetic particle radiation found in the heliosphere?" the whole Solar Orbiter's payload contributes to improving information on the origins of the *Solar Energetic Particles* (SEP). The VL, UV and X-rays imaging provide data of coronal loops, flares and CMEs with their location and timing; this kind of data combined with radio signature of coronal shock and escaping electrons, and in-situ measurements of turbulence or shocks passages, provides critical constraints on shock evolution models in regions very close to the Sun. Furthermore it will be possible to infer the SEP seed population from heavy ions abundances and suprathermal particles.

SEPs can mainly be accelerated via CME driven shock or along loops and reconnecting regions. In the first case, Solar Orbiter will observe how shocks evolve (with remote-sensing) and if they are still accelerating the particles when they pass the spacecraft. It will simultaneously measure the turbulence properties in the shock acceleration region (in-situ), and so it will be possible to construct a complete model of the acceleration process.
For the latter case, Solar Orbiter will see the coronal location from UV and X-rays, and then trace the released electrons by radio emission (that will drift from the plasma frequency at the level of the spacecraft for the bursts that pass by). This allow us to trace the magnetic field lines up to the spacecraft position by means of the in-situ instrumentation.

To answer the last question: "How does the solar dynamo work and relate the Sun to the heliosphere?" it is important to consider that the Sun is a self-sustained dynamo, which converts the convective motion from its interior and the differential rotation into electromagnetic energy, generating the global magnetic field. For long the dynamo was believed to

be located in the *tachocline*, a shear layer at the base of the convection zone. More recently, other possibilities have been taken into account, as dynamos located lower in the convection zone, distributed dynamos, and dynamos around the near-surface shear layer. The global dynamo, presumably due to the differential rotation and the meridian flux near the base of the convection zone, leads to the appearance of large bipolar magnetic regions (active regions) on the solar surface at latitudes between 5° and 30° and smaller and ephemeral regions active over a wider range of latitudes, but also concentrated at low latitudes. In addition to the global dynamo, turbulent convection could generate a local dynamo that is thought to be responsible for generating the observed small-scale internetwork field, which is ubiquitous across the solar surface and dominates the emergent unsigned flux. This local component is expected to enhance field more uniformly across the surface. To distinguish a global and a local dynamo it is necessary to study the distribution of small elements of emerging magnetic flux on a given heliographic latitude.

Observations made on the ecliptic plane cannot quantitatively determine the distribution of the magnetic flux as a function of latitude and in particular the emergence of small-scale magnetic features (internetwork fields). Solar Orbiter, flying above the ecliptic, is able to measure weak magnetic features at both low and high latitudes. If the number and size of such features differ significantly at high latitudes, then the weak features are likely due to the global dynamo. If, however, they are evenly distributed, the evidence for a significant role of a local dynamo will be greatly strengthened.

Solar Orbiter resolves small-scale magnetic features based on vector magnetographic measurements performed by SO/PHI. It measures also magnetic flux transport near the solar surface by combining the tracking of small features, the mapping of Doppler shifts and the helioseismic observations.

Exiting the ecliptic plane, remote-sensing instruments will characterise the Sun's polar region for the first time; by comparing the properties of the polar magnetic flux from different orbits, Solar Orbiter will provide a constraint on the strength and direction of the meridional flow, so far poorly characterized at high solar latitudes.

The observations campaigns performed at the highest heliographic latitudes will allow us to study the transport of the magnetic flux that drives the polarity reversal of the global magnetic field. The joint observations of Solar Orbiter and Parker Solar Probe on the ecliptic plane will enable coordinated investigation of the 3D structure of the inner heliosphere.

These observations reveal the links between the polar regions and the properties of the solar wind and the interplanetary magnetic field.
Furthermore Solar Orbiter, as it crosses the slow/fast wind boundary at mid-latitude, around 0.5 au, will measure the solar wind field and plasma properties. Using various magnetic field extrapolation methods these observations allow us, for the first time, to simultaneously study the photospheric and coronal magnetic fields in polar coronal holes and to study the evolution of the boundaries of polar coronal holes and other coronal structures.
In each orbit the spacecraft passes both north and south of the solar equatorial plane, therefore it follows the evolution of the solar wind and the interplanetary magnetic field.

Solar Orbiter, Parker Solar Probe with SOHO, STEREO and SDO[17] maintain that continuity of observations of our star, necessary to follow and understand its variability over time.
These missions are sentinels that contribute critically to our ability of predicting the changes in Earth's space environment, that affect so much life and technology on Earth. This topic is so important for the worldwide scientific community that several new solar missions are at the beginning of their journey, as the Chinese ASO-S (Gan et al. 2022) which just finished the Commissioning phase, or are planned to start soon, as the Indian ADITYA-L1 (Tripathi et al. 2022) and the NASA mission PUNCH (Deforest et al. 2022), whose launches are planned respectively on 2023 and 2025.
In the next chapter I will describe Metis, the coronagraph on board Solar Orbiter whose data I used to perform the data analysis, topic of this thesis work.

[17] The *Solar Dynamics Observatory* (SDO) was launched on February 2010, into a geosynchronous orbit (Pesnell et al. 2012). Its images are used to study solar variability, to characterize the interior of the Sun and the various components of magnetic activity.

Chapter 2

The Metis coronagraph and the observation of the extended solar corona

The Metis coronagraph is one of the six remote-sensing instruments aboard the Solar Orbiter spacecraft. The specific objective of Metis is to observe the solar corona in polarized brightness (pB[1]) and total brightness (tB[2]) visible light and in the integrated intensity of the H I Ly-α line. The faint emission of the solar corona, which is more than a million times weaker than the one from the solar disk, can be observed only by occulting the Sun disk. This chapter describes briefly the diagnostic techniques used on the Metis data to achieve its scientific objectives and how the instrument works. More details can be found in Antonucci et al. 2020 and in Fineschi et al. 2020 (and the references therein).

2.1 Metis scientific objectives and its performances

Metis was designed to combine and extend the imaging capabilities of SOHO and STEREO coronagraphs. It can simultaneously study the visible and ultraviolet emission of the solar corona and diagnose, with an unprecedented temporal resolution (as low as 1s), the struc-

[1] A sequence of Metis pB consists of 4 VL images, acquired at different polarization angles, e.g. 0°, 45°, 90°, 135°.

[2] Every Metis tB image is acquired switching the polarization angle (e.g. 180° and 360°) exactly in the middle of the detector integration time. After the acquisition, both pB and tB frames are produced by using the theoretical Müller demodulation matrix (Antonucci et al. 2020; Capobianco et al. 2018; Casti et al. 2019; Fineschi et al. 2020; Liberatore et al. 2021).

ture and dynamics of the corona over a field of view from 1.6° to 2.9° from the center of the Sun, which corresponds to 1.7 $R_\odot$ - 3.0 $R_\odot$ when the spacecraft is at minimum perihelion (0.28 au). The study of coronal properties is very important to achieve the scientific objectives of Solar Orbiter, especially if we consider that the region investigated by Metis is crucial for linking the phenomena of the solar atmosphere to their evolution in the inner heliosphere. Metis is an externally occulted coronagraph designed to perform simultaneous imaging of the off-limb solar corona in two channels: the ultraviolet (UV) channel in the narrow band H I Ly-α line at 121.6 ± 10 nm and the visible light (VL) channel in the broad band between 580 and 640 nm.
The instrument provides the following data:

- global maps of *pB* and *tB* emission (with 2048×2048 pixels frames);
- global maps of H I Ly-α emission (with 1024×1024 pixels frames).

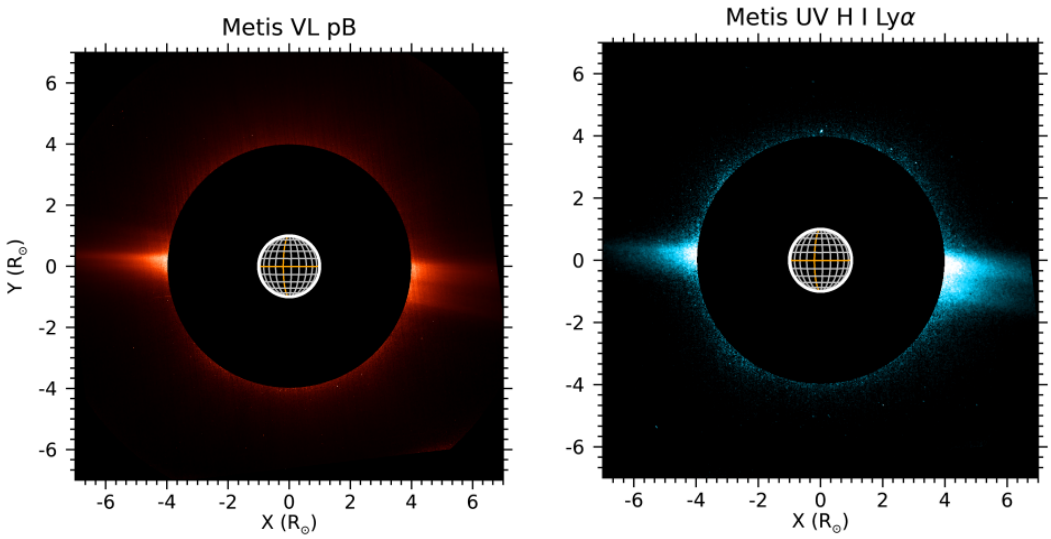

Figure 2.1: Metis first light VL polarized brightness (left panel) and H I Ly-α (right panel) emission, observed at 0.64 au on May 15, 2020, within a FoV ranging from 3.8 $R_\odot$ to 7 $R_\odot$ (from Romoli et al. 2021)[3].

These measurements allow a complete characterization of protons and electrons which are the most abundant components of the coronal plasma and solar wind. Furthermore, with

[3]Taken from Romoli et al. 2021 with permission © ESO.

Table 2.1: Metis' contribution to Solar Orbiter science.

Solar Orbiter scientific goals	Unique contribution of Metis
What drives the solar wind and where does the coronal magnetic field originate?	Investigation of the region from which the solar wind is accelerated up to approximately its asymptotic value
How solar transient phenomena drive the heliospheric variability ?	Investigation of the region where the first and more dramatic phase of the propagation of CMEs occurs.
How do solar eruptions produce the energetic particle radiation found in the heliosphere ?	Identification of the path of shock fronts which accelerates particles in the solar corona
How does the solar dynamo works and drive connection between the Sun and the heliosphere?	Study of the global magnetic configuration by identifying the closed and open magnetic field regions in the corona.

the analysis of these data, Metis is able to provide a unique answer to the science of Solar Orbiter summarized by the four questions reported in Table 2.1 (see also Section 1.3.3).

2.1.1 Metis maps and diagnostic techniques

One of the most important innovations introduced by Metis is that of being able to acquire simultaneous maps in polarized VL and in UV. The data obtained from one map, such as the electron density profiles from *pB* images, are used for the diagnostics of the other map (UV), allowing us to obtain information on the hydrogen outflow speed using the Doppler dimming technique (see the sections 1.2 and 1.3.3).

The acquisition of *pB* images ensures that the measured signal is caused by electron scattering (K corona) and not dust particle scattering (F corona), whose effect becomes prevalent with increasing heliocentric distance (Blackwell & Petford 1966). From the VL frames it is possible to derive maps of the coronal electron density profiles by using various techniques (see, e.g., van de Hulst 1950, Hayes et al. 2001, Quémerais & Lamy 2002 and reference

therein). In fact, simplifying, the intensity from the *pB* images I_K can be written as

$$I_K \sim \text{cost} \cdot < N_e > \tag{2.1}$$

where the constant depends on geometric factors which do not introduce other physical parameters of the plasma, and $< N_e >$ is the electron density averaged on the line of sight (see also Eq. 20 and Fig. 5 in van de Hulst 1950). $< N_e >$ represents the fundamental quantity for all coronal diagnostics.

The Metis UV channel maps the emission of the H I Ly-α line, another important quantity to investigate the extended corona (Withbroe et al. 1982). The excitation of an ion occurs radiatively by absorption or scattering of a photon or by collision with an electron, the subsequent emission occurs by spontaneous de-excitation, because the corona is an extremely thin medium.
Based on the type of excitation, the study of the spectroscopic lines provide different parameters, which reflect the physics of the process that promoted the electrons to higher energy levels.

The case in which a radiatively excited ion re-emits energy at the same wavelength as the incident radiation is called "resonant" scattering and is the physical process underlying the formation of the H I Ly-α line. Other two different phenomena contribute to the formation of this line, such as the collisional excitation of neutral hydrogen atoms by free coronal electrons, and the Thomson scattering of Ly-α chromospheric photons by free electrons in the corona. However, for hydrogen the latter two components are negligible.
Although only one proton out of 10^7 is found in the corona in the form of neutral hydrogen (due to high temperature and low density conditions), the H I Ly-α line is the most intense one of the EUV spectrum even at large distances from the solar surface, due to the large abundance of protons and the high intensity of Ly-α chromospheric radiation.

In a very schematic way the H I Ly-α intensity can be expressed as

$$I_{Lya} \sim \text{cost} \cdot R(T_e) \cdot D(w, T_k) \cdot < N_e > \tag{2.2}$$

where $R(T_e)$ the ionization balance of hydrogen which depends on the temperature of the electrons T_e and $< N_e >$ the average coronal electron density along the LoS. In the case of hydrogen $R = \frac{N_{H0}}{N_H} << 1$. The Doppler dimming factor $D(w, T_k)$ depends on the solar wind

speed w and on the kinetic temperature of the ions T_k. The radial variation of T_e in the outer corona is assumed to be an average of the electron temperature radial profiles derived at solar minimum by Gibson et al. 1999 for equatorial regions and by Vásquez et al. 2003 for polar regions. The T_k hydrogen kinetic temperature relative to a solar minimum epoch is obtained from UVCS Ly-α spectroscopic observations and is deduced from the H I Ly-α line broadening, determined by the velocity distribution of the hydrogen atoms along the LoS, which includes contributions due to non-thermal mechanisms. Both T_e and T_k are obtained according to the same approach used by Romoli et al. 2021.

$D(w, T_k)$ is always a factor ≤ 1 and represents the attenuation of the H I Ly-α emission from the expanding corona relative to a static one (Noci et al. 1987; Withbroe et al. 1982). The attenuation is caused by the Doppler shift of the chromospheric emission lines with respect to the coronal absorption lines and is tightly related to the presence of large-scale motions of the coronal plasma (e.g. the solar wind). In fact, in a static corona, the emission profile of Ly-α and the absorption profile of the neutral hydrogen atoms would be centered on the same wavelength of the line, thus maximizing the resonance and consequently the intensity of the line. In the presence of outflows, the intensity of the line decreases with the reduction of the overlapping of the absorption and emission line profiles. The decrease is a function of the outflow speed of the wind particles (w), therefore, by measuring the line attenuation it is possible to obtain the wind speed. The sensitivity interval of the Doppler dimming effect ranges from 0 to about 450 km/s, in fact H I Ly-α line is significantly reduced for outflow velocities higher than 100 km/s and appears to be completely dimmed for $w > 450$ km/s, while the line intensity reduction by a factor of 3% occurs for $w = 50 - 60$ km/s (Dolei et al. 2018). As it is possible to notice from the right panel of Figure 2.2 Metis can observe the accelerating region for the slow wind, while the fast component at the polar regions is already dimmed.

In summary, the data analysis on the Metis calibrated images allows to obtain respectively:

- global maps of mean electron density $< N_e >$ from *pB* images (see left panel of Figure 2.2),
- global maps of outflow velocity of the hydrogen N_{H^0} from UV images, by using the obtained electron density and exploiting the Doppler dimming effect (see right panel

of Figure 2.2).

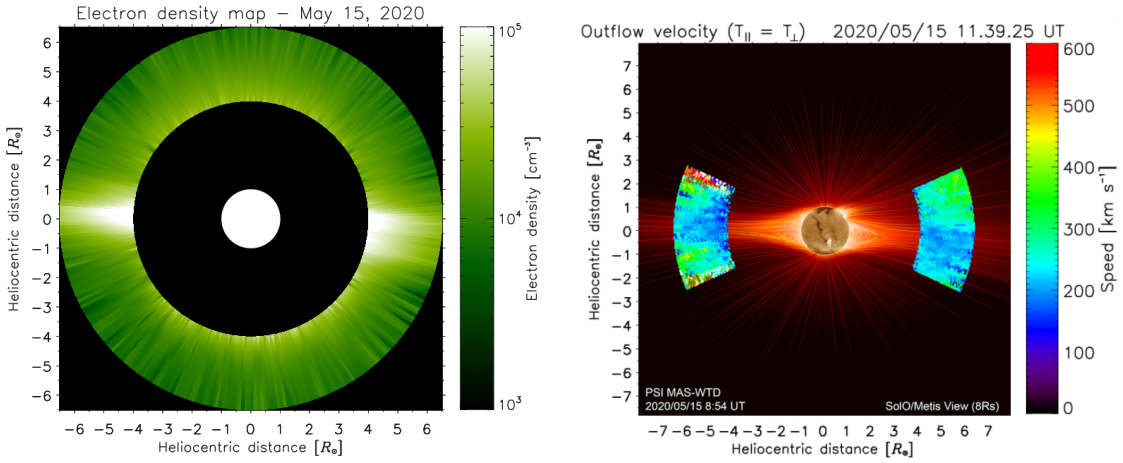

Figure 2.2: Left panel: electron density map obtained from *pB* frames acquired at 0.64 au on May 15, 2020, within a FoV ranging from 3.8 $R_\odot$ to 7 (courtesy of G. E. Capuano). Right panel: outflow velocity map (in case of isotropy of the neutral hydrogen kinetic temperature along the radial direction) for the same observations campaign (from Romoli et al. 2021)[4].

2.2 Instrument description

Metis is composed by four separate physical units: the *Metis Optical Unit* (MOU), the *Metis Processing and Power Unit* (MPPU), the *Camera Power Converter* (CPC) and the *High Voltage Unit* (HVU), shown in Figure 2.3. The MOU contains all the opto-mechanical elements and detectors that produce images of the solar corona in visible and ultraviolet light.

The MPPU contains the electronics that manage the instrument operations, acquire and process the data produced by the detectors. Moreover it converts and distributes the power received from the spacecraft and provides the data interface with Solar Orbiter.

The CPC supplies the low voltage power supply to the two detectors. The HVU generates the high voltages to power on the UV channel intensifier (see Section 2.2.3).

The *harness* provides all the electrical connections between the Metis units.

[4]Taken from Romoli et al. 2021 with permission © ESO.

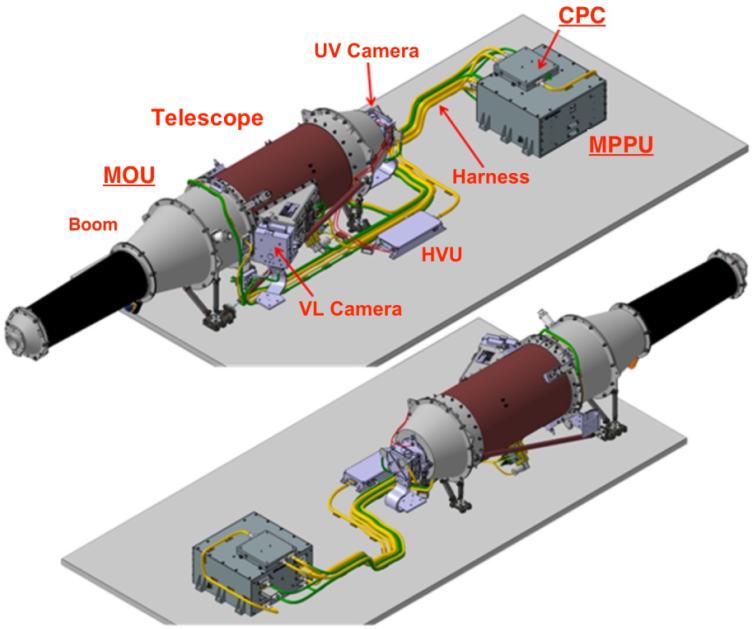

Figure 2.3: Metis coronagraph in its flight configuration, consisting of the Metis optical unit (MOU), the camera power converter (CPC), the Metis processing and power unit (MPPU) and the high voltage unit (HVU), which provides the high voltage to the UV detector (taken from Antonucci et al. 2020 with permission © ESO).

2.2.1 The telescope

Metis is an externally occulted coronagraph, consisting of an on-axis Gregorian telescope that feeds both the VL and the UV channels by means of a beam splitter. The telescope is coupled with a system of diaphragms to remove the light from the solar disk, which is called external occulter.

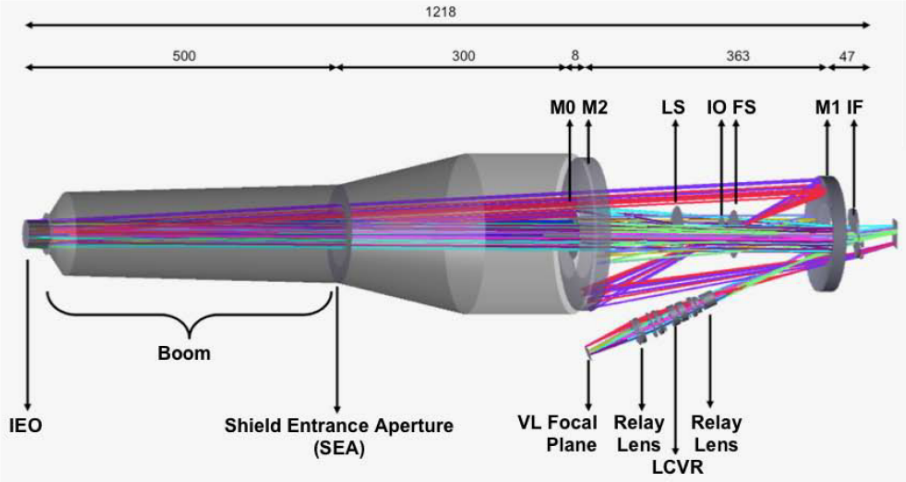

Figure 2.4: Optical layout of the VL and UV light paths in the coronagraph. IEO is the Inverted External Occulter, M0 is the disk-light rejection mirror, M1 and M2 the primary and secondary telescope mirrors respectively, LS is the Lyot Stop, IO the Internal Occulter, FS the Field Stop, IF the interferential filter and LCVR the Liquid Crystals Variable Retarders inside the polarimeter (see the text for more details). The measurements are in mm. Image adapted from Antonucci et al. 2020 with permission © ESO.

The optical design of Metis is innovative compared to previous coronagraphs. In the classic optical path of externally occulted coronagraphs, an occulter disk is the outermost element, that shadows the primary objective from the sun disk light. Metis telescope exploits an inverted scheme: the outermost element is the *Inverted External Occulter* (IEO), the entrance pupil of the telescope, and downstream it is located the occulter M0, the sun disk rejection mirror. This design minimises the thermal load on the instrument, which is necessary, given its close operational distance to the Sun. The optical paths of the two observation channels are shown in Figure 2.4, while Figure 2.5 shows an optomechanical exploded view of the telescope.

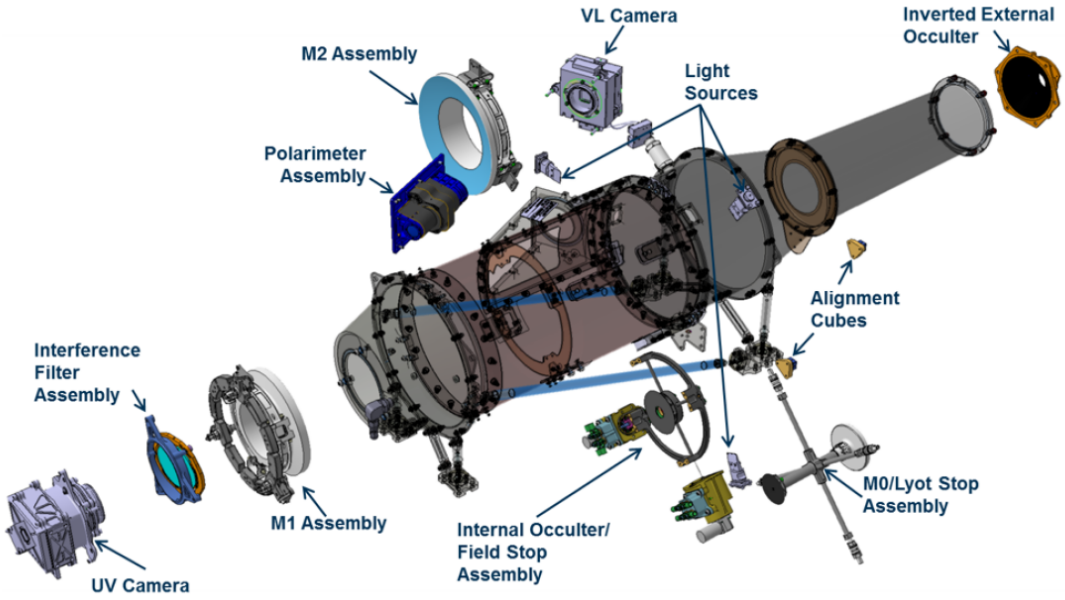

Figure 2.5: Opto-mechanical subsystems of the Metis telescope (taken from Antonucci et al. 2020 with permission © ESO).

The mirror M0 blocks the radiation from the solar disk nominally up to about 1.2° from the telescope optical axis, which nominally points to the Sun center: M0 is a spherical mirror with a focal length equal to its distance from IEO, in order to focus the image of the solar disk in one area of the entrance aperture thus ejecting the unwanted light with a minimal thermal impact on the instrument.

From a mechanical point of view, the boom consists of an opaque tube delimited at its ends by IEO and M0 and containing the *Shield Entrance Aperture* (SEA), which has the purpose of reducing the stray light[5] inside the tube. The IEO is mechanically supported by a special structure that protrudes from the chassis of the spacecraft through the heat shield. It has an optimized inverted truncated cone shape, to reduce the diffraction of a circular aperture, which is the major component of stray light inside the instrument.

The Metis telescope is composed of two concave mirrors (primary M1 and secondary

[5]Stray light is the unwanted light arriving on the detector and the main source of optical noise for a coronagraph. It is due to several contributions, the main being the diffracted light by the IEO, and the light scattered by the "nano-roughness" of the telescope mirrors.

M2) in Gregorian configuration, whose primary focus is accessible and where the *Internal Occulter* (IO) is placed.

Aiming to reduce the scattered light of the edges of IEO and M0 produced by M1, the *Internal Occulter* (IO) and the *Lyot stop* (LS) are placed along the optical path. IO is an aperture stop with $\oslash_{inside} = 5.0$ mm that occults the image of IEO inner edge. LS is an occulter disk which eliminates the image produced by M1 of the scattered light by the edge of M0, it is located immediately behind IO (see Figure 2.4). Combined together, IO and LS limit the inner FoV of Metis. It is a circular, smooth boundary at about 1.6°. The outer FoV is determined by using the *Field Stop* (FS) and by the detectors size. The detectors delimit a square of ±2.9° in width. The corners are vignetted by the round FS at 3.4°.

The simultaneous feeding of the channels is carried out by using an *Interference Filter Assembly* (IFA) which works as a beam splitter. The IFA separates VL and UV rays simultaneously since it consists of a magnesium fluoride window (MgF_2) with flat and parallel faces, with a coating of $Al + MgF_2$ which reflects the VL in the polarimeter and transmits within a bandpass of 121.6 nm ± 10 nm.

On the focal planes of the two optical paths there are the UV and VL detectors, behind the IFA and behind the polarimeter, respectively (see Figure 2.4).

The polarimeter assembly is used to carry out the measurements in polarized brightness, fundamental for the coronal diagnostics (see Section 2.1.1), and consists of the following elements:

- a collimating optical system CD (collimating doublet),
- a bandpass filter (BP) which selects the wavelength range 580-640 nm,
- a linear polarization analyzer,
- a focusing optical system on the detector plane of the visible channel, which provides a magnification of 0.67 of the original image.

The polarization analyzer is composed of a *Quarter Wave Retarder Plate* (QWP), two *Liquid Crystals Variable Retarder* (LCVR), organized in the *Polarimeter Module Package* (PMP) unit and a linear polarizer (LP).
Table 2.2 summarizes all the optical parameters of the telescope.

Table 2.2: Metis optical parameters (Antonucci et al. 2020; Fineschi et al. 2020).

Field of view	1.6° - 2.9° or 1.6 $R_\odot$- 3.0 $R_\odot$at 0.28 au ; 2.8 $R_\odot$- 5.5 $R_\odot$at 0.5 au
Telescope type	externally occulted, on-axis Gregorian
Effective focal length	UV: 300 mm , VL: 200 mm
F – number (without occultation)	UV: 7.5 - VL: 5
External Inverted Occulter (IEO)	Truncated Cone Occulter outer $\oslash = 40$ mm
Distance IEO-M0	800.0 mm
Sun disk light rejection mirror M0	Spherical: $\oslash = 71.0$ mm Curvature radius: 1600.0 mm
Distance M0-M1	370.6 mm
Primary mirror M1	Ellipsoid on axis: outer $\oslash = 163.0$ mm, inner $\oslash = 88.0$ mm Curvature Radius: 272.0 mm, conic: -0.662
Distance M1-M2	363.0 mm
Secondary mirror M2	Ellipsoid on axis: outer $\oslash = 219.0$ mm, inner $\oslash = 125.0$ mm Curvature Radius: 312.4 mm, conic: -0.216
Internal Occulter IO	Distance M1-IO: 153.9 mm $\oslash = 5.0$ mm
Lyot stop LS	Distance M1-LS: 219 mm Circular darkening: $\oslash = 47$ mm
Distance M2-focal plane UV	505.2 mm
Stray light level	UV: $<10^{-7}$, VL: $<10^{-9}$
Wavelength bandpass	UV: H I Ly-α (121.6 ± 10) nm VL: 580-640 nm
Detectors	UV: Intensified APS, Image size: 30.7 mm (1024 × 1024 pixels), scale factor: 20 arcsec/pixel, pixel size: 30 μm VL: APS, Image size: 20.5 mm (2048 × 2048 pixels), scale factor: 10.7 arcsec/pixel, pixel size: 10 μm

2.2.2 The Metis field of view

One of the important novelties introduced by Metis is the simultaneous acquisition of coronal emission maps in the VL and in the UV band pass, since the scientific data from a channel (pB) are fundamental for the diagnostics of the other channel data.

The regions investigated by Metis are crucial for determining the acceleration mechanism of the solar wind or for following the development of the CMEs. They are established by the coronagraph FoV, which is annular and centered on the Sun.

The FoV extends from 1.6° to 2.9° reaching 3.4° in the corners of the square outer shape provided by the detectors as shown in Figure 2.6. With this FoV Metis can observe the extended corona from 1.7 $R_\odot$ to over 9 $R_\odot$, based on the distance of the spacecraft from the Sun on its elliptical orbit. The panels in Figure 2.6 show the simulation of the Metis

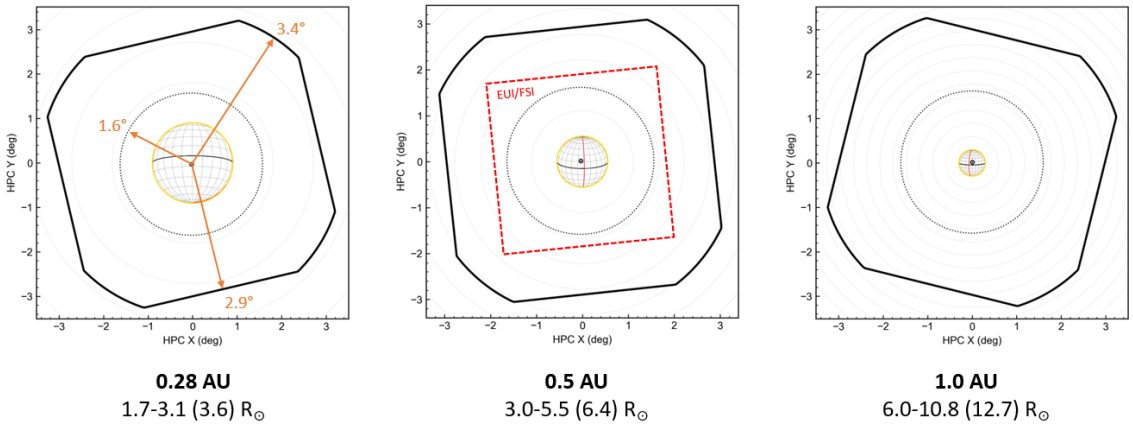

Figure 2.6: Simulation of the Metis FoV for three values of the instrument distance from the Sun: 0.28 au (minimum perihelion), 0.5 au and 1.0 au. The second panel shows the overlap between the FSI FoV and the Metis one. See the text for details. Courtesy of Roberto Susino.

FoV for three values of the distance d_{Metis}: 0.28 au (minimum perihelion), 0.5 au and 1.0 au. In the first case the FoV extends from 1.7 $R_\odot$ to 3.1 $R_\odot$ (3.4 $R_\odot$ in the corners), in the second case from 3.0 $R_\odot$ to 5.5 $R_\odot$ (6.4 $R_\odot$) and in the last case the FoV ranges from 6.0 $R_\odot$ to 10.8 $R_\odot$ (12.7 $R_\odot$).

2.2.3 Metis detectors

Both detectors of Metis were developed by MPS[6] specifically for the Solar Orbiter mission. Each of them consists of a *Complementary Metal-Oxide Semiconductor* (CMOS) *Active Pixel Sensor* (APS) detector: the dectection system for the VL channel is called *Visible Light Detector Assembly* (VLDA), and for the UV channel *UV Detector Assembly* (UVDA). The two channels are designed to work simultaneosly and independently and they have both the capability of acquisitions with 1s cadence, a novelty for space coronagraphs.

VLD Assembly

The VLD consists of a CMOS APS camera that acquires images in the selected 580-640 nm spectral range. The sensor is a 2048×2048 pixels matrix and the pixel size is equal to 10 μm, the scale factor is 10.7 arcsec pixel^{-1}. VLD operates in analog mode, which collects the charge created by the incoming photons during a planned integration time. The acquired data are transferred to the MPPU unit for subsequent processing.

UVD Assembly

The UVD is an *Intensified* APS (IAPS), consisting of a *Micro Channel Plate* (MCP) with photocathode coated with potassium bromide (KBr) and optically coupled, via a fiber optic taper, to a 1024×1024 pixels APS. The fiber optic taper serves to rescale the image arriving at the focal plane to the detector size. The scale is 2:1, so the pixel size of 15 μm results in an effective sampling element of 30 μm at the focal plane, the scale factor is 20 arcsec pixel^{-1}. The sensor is vacuum sealed and protected by a window in MgF_2. The use of the intensifier is necessary for the imaging in the H I Ly-α line because the UV coronal signal is too weak to be detected by a standard APS without suitable signal amplification.

The UVDA has two main possible operating modes: photon counting mode and analog mode.

The acquired data, as for the other channel, are transferred to the MPPU. The voltages required by the MCP and by the phosphor screen are supplied by the external unit HVU.

[6] Max Planck Institut für Sonnensystemforschung, in Göttingen, Germany.

2.2.4 Electronics

The detection subsystems includes also two services units: the CPC provides regulated power to both detectors, while the HVU provides the high voltages needed by the intensifier of the UVDA (see Figure 2.3).

The MPPU is the main electronic unit of the whole instrument. It supplies all the control and managements functions of the MOU. In particular, it operates the detectors and controls the telescope mechanisms and the thermal hardware in the MOU. Furthermore, it interfaces to the CPC, the HVU and the Solar Orbiter spacecraft for instrument power and data transmission (*telemetry and telecommands*, TM/TC, and science data). In the MPPU the Metis flight software is loaded, which implements the instrument operation, control, and fault detection, isolation and recovery (FDIR) functions.

The on-board software (OBSW) executes the telecommand sequences that correspond to the scientific and engineering activities. It manages the Metis communication with the Solar Orbiter platform services and the FDIR events and the thermal control, to grant autonomy in case of failure or instrument internal heating due to solar radiation. Finally, it is in charge of acquiring, processing, and compressing the scientific data (see Section 2.3).

2.3 Data processing

Both UV and VL acquired data undergo the on-board processing depicted by the data processing flow shown in Figure 2.7.

After the reading of the data, a dedicated algorithm is applied to each acquisition in order to remove signatures of cosmic rays (CR) and solar energetic particles (SEP).

The corrected acquisitions are then averaged for each channel in order to increase the signal-to-noise ratio (SNR) and limit the data volume.

Considering the telemetry limitations imposed by an interplanetary mission, it is necessary to reduce the size of the images as much as possible before their transmission. A *masking* procedure can therefore be applied to remove the pixels corresponding to the occulter shadow. If planned, also a *binning* procedure is applied to reduce the size of the matrix by summing a certain number of adjacent pixels.

Finally, a compression algorithm is used which further reduces the data to be transferred to ground (reducing the data volume of a factor up to 50). The algorithm is based on an ESA

standard and is predictive; it allows both *lossless* compression, which preserves the initial information completely, and *lossy* which instead degrades part of the original information in a controlled way to obtain a higher compression ratio.

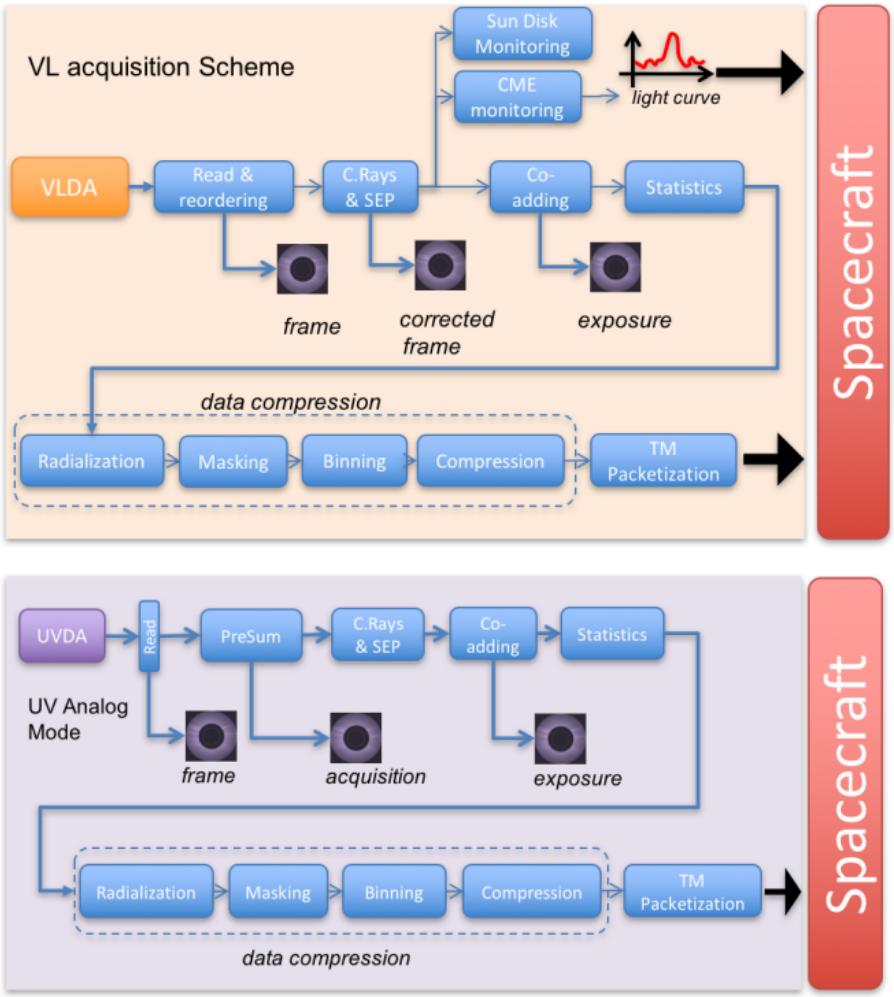

Figure 2.7: Top panel: Scheme of the VL channel data flow. Bottom panel: Scheme of the UV channel data flow. The blue boxes identify each step of the on-board data processing (taken from Antonucci et al. 2020 with permission © ESO).

2.4 Observation planning and Metis operations

Solar Orbiter is considered a *deep-space* mission. This means that it is not possible to operate the various instruments in real-time, but the observations have to be planned in advance. The need for planning comes out from the science goals of the mission (see Sec.1.3.3), the capabilities of the platform and the payload, and the telemetry constraints due to the orbit. To maximize the scientific return, it is necessary to coordinate the observation between the remote-sensing and in-situ payload.
Solar Orbiter is the first mission carrying Sun-observing telescopes so close to the Sun and in-situ instruments at the same time. The in-situ instruments can operate continuously, but this is not the case for the remote-sensing instruments. For each orbit, there are three 10-day windows during which the complete instrument suite operates (*Remote-Sensing Windows*, RSWs). The three windows are generally centered around the closest approach and the minimum and the maximum heliolatitudes (Zouganelis et al. 2020). However, an improvement of the telemetry at the beginning of the mission permitted the RS instruments to add a low telemetry synoptic program along all the orbit.

As explained in Auchère et al. 2020 and Zouganelis et al. 2020 the long term planning is performed at mission level rather than at instrument level. This planning is driven by six-month length periods and the mission planning cycles for the routine science operations consist of:

- Long-Term Planning (LTP): it covers a six-month period, which approximately corresponds to an orbit. The ten instruments build a coordinated plan to address the science objectives decided for that period at mission level.

- Short-Term Planning (STP): it covers approximately one-week timeframe and is the unit that composes the LTP. It results in a generation of detailed schedules of commands for the spacecraft and for the payload instruments.

The operations planning also applies to Metis and therefore specific observation methods have been defined to achieve the scientific objectives. In general, the Metis observations consist of global maps of the coronal emission in the VL and UV band pass, obtained with different spatial and temporal resolutions, depending on the observational target of interest .

The observation modes of Metis can be divided into *Standard* and *Special*. For the former (also called nominal methods) observing campaigns are carried out for the various "*case studies*", identified at a scientific level, thus the modes are distinguished on the base of the scientific objectives more than the acquisition parameters. The latter are methods that can be used in particular situations, with the occurrence of an event, for example during the transit of comets, planets and stars or during solar transient events like CMEs and eruptive prominences, or even to exploit joint observations with other missions, primarily Parker Solar Probe. These events are called *targets of opportunity*.

The nominal modes are as follows:

- **WIND** - It measures the electron density and speed of the expanding solar wind. Fast and slow solar wind fluxes are identified in the global maps based on the hydrogen flux velocity values.
- **MAGTOP** - It measures the solar wind speed and its relationship with the magnetic topology. It maps the velocity of the hydrogen flow along the streamer/coronal hole interfaces, above streamers cusps and inside streamers. This is the nominal mode with the highest spatial resolution (20 arcsec for both channels).
- **GLOBAL** - It performs global measurements of the corona configuration and evolution before, during and after CME events. With these measurements it is possible to infer the geometry of neutral hydrogen and coronal electrons and their evolution over time, having information on the timing, mass contained, and overall dynamics of CMEs.
- **Long-Term CONFIG** - It monitors the general evolution of the coronal configuration at large scales and during off-plane observation windows. With this mode it is possible to determine the longitudinal distribution of electron density in the solar corona, and the mass and the energy flux carried away by the solar wind. This mode has the highest exposition time (300-450 s) and the lowest cadence (20-30 min).
- **FLUCTS and TBF (*Total Brightness Fluctuations*)** - It provides spectra of brightness fluctuations. It is an optimized procedure for the perihelion. It has a high spatial

resolution and covers a range of distances from 1.6 $R_\odot$ to 5 $R_\odot$. The acquisitions are performed at the highest cadence (1 s for FLUCTS and 20 s for TBF).

The *Special* observation modes are:

- **CMEOBS** - It will track the eruption and propagation of CMEs, with the related erupted prominences, driven shocks, and accelerated SEPs. It will measure the electron density and the outward expansion rate gradient, both at high spatial and temporal resolution. This mode is activated by a CME event (with a special signal from the on-board software, called *flag*). The measurements obtained can be used to identify the path of the accelerated particles in the outer solar corona and, combined with radio observations, will help to distinguish the cause of the acceleration of the SEPs between flares and CMEs.
- **COMET** - It will map the comets and sungrazing comets emission and monitor their evolution along the trajectory near the Sun.
- **PROBE** - It will perform observations coordinated with Parker Solar Probe.

Each observational mode is conceived as a continuous repetition of a basic acquisition, suitably configured, of a duration equal to a planned cadence. The cadences for the *Standard* modalities range from 5 to 30 minutes and are usually iterated to cover observing campaigns of several hours (or days) during the different observing windows of the mission. Instead the *Special* modes are usually performed with reduced cadences, of about one minute, with overall durations of a few hours.

Beside these modes, as already mentioned, Metis can perform synoptic observations. This observation plan is executed along the spacecraft orbit, outside the RSWs. Depending on the heliocentric distance of the spacecraft d_{SO}, only VL images are acquired ($d_{SO} >$ 0.6 au), or both VL and UV images ($d_{SO} <$ 0.6 au). The synoptic plan provides four VL images per cadence to obtain *pB* or *tB* data, and when acquired, one UV image per cadence.

Currently the events that could modify the normal observation plan of Metis are mainly represented by the detections of transient events such as CMEs or over-illumination. The

first case permits to activate an observation mode suitable for capturing scientifically interesting phenomena whose occurrence cannot be planned in advance. On the other hand, the over-illumination, due to the entry of the image of the solar disk into the Metis FOV, is a symptom of incorrect pointing by the S/C and immediately triggers a safety procedure, which leads the instrument to interrupt normal acquisition and switch off the detectors in order to preserve their functionality (in particular for the UVDA intensifier).

Amongst the several observation modes, Metis performs in-flight calibration operations, including characterization and performance verifications activities. In particular, VL_RC and UV_RC are the operations devoted to perform the radiometric calibration of the two channels of the instrument.
The data obtained from these operations have been used for the analysis described in Chapter 3 and in Chapter 4, which respectively refer to the radiometric calibration of the VL and UV channels, main topics of this work.

Chapter 3

In-flight radiometric calibration of the VL channel of Metis

3.1 Introduction

This chapter is focused on the in-flight radiometric calibration of the VL channel of Metis described in De Leo et al. 2023, paper A[1]. The radiometric calibration is necessary to obtain the absolute brightness of the solar corona from the imaging data acquired with the VL channel during the several phases of the mission. Furthermore, it allows us to monitor the aging of the VL channel, starting from the beginning of the *Cruise Phase* of Solar Orbiter. Besides the calibration and characterization activities already performed on-ground, I used stellar target transits across the instrument field-of-view (FoV) to infer the radiometric calibration factor ϵ_{VL}.

Star observations have been extensively used to calibrate space-based instruments and a significant heritage exists on this topic, such as the in-flight calibration campaigns of the following coronagraphs: Large Angle Spectrometric COronagraph (LASCO-C2, Brueckner et al. 1995; Colaninno & Howard 2015) on board the Solar and Heliospheric Observatory (SOHO, Domingo et al. 1995), COR2 (Baldwin & Vourlidas 2008), LASCO-C3/SOHO (Thernisien et al. 2006) and UltraViolet Coronagraph Spectrometer/SOHO (UVCS, Romoli et al. 2002).

[1] Section 3.1 to Section 3.2.5 are Sect. 1 and Sect. 2 (after a rewording) in the peer reviewed publication De Leo et al. 2023, paper A, submitted to *Astronomy&Astrophysics* and accepted.

The procedure (*pipeline*) to obtain calibrated data (level 2 or L2 data), for both channels of Metis, consists of a "chain" of operations applied to the images acquired onboard (L0 data). The images are first corrected by dark, bias, and flat-field[2] (measured in-flight) and by the vignetting pattern (measured on ground). Then the signal is transformed into count rates by dividing by the exposure time. The obtained radiometric calibration factor ϵ_{VL} is finally used to convert the observed Digital Numbers (DNs) per pixel into photons and to express the calibrated frames in radiance (photons m^{-2} sr^{-1} s^{-1}). The L2 final data expressed in mean solar brightness (MSB) units are obtained by dividing the calibrated frames by the average surface brightness of the solar disk in the wavelength range of the instrument. The latter is provided in the header of the correspondent L2 data.

After this procedure, for the VL channel, the total brightness *tB* and the polarized brightness *pB* frames are produced by using the theoretical Müller demodulation matrix (Antonucci et al. 2020; Capobianco et al. 2018; Casti et al. 2019; Fineschi et al. 2020; Liberatore et al. 2023). The L2 data contain also the uncertainty matrix that takes into account the full error propagation from the steps mentioned above.

The calibration performed using star targets, with known and stable fluxes, is a way to measure the radiometric response and its variation over time of the VL channel in-flight with astronomical sources as "standard candles" and represents a key measurement to derive quantitative information from the solar corona observations. Furthermore stars, being point sources, are ideal to verify the instrumental spatial resolution by gaining information on its *point spread function* (PSF).

3.2 The VL channel radiometric calibration factor

This section explains the method used to infer the value of the radiometric calibration factor ϵ_{VL} (in DN/photon).

The data used for this analysis cover a time range from June 2020 (observations of α and ρ Leonis) until March 2021 (observation of θ Ophiuchi), as reported in Table 3.1. Figure 3.1 shows the position of Solar Orbiter along its orbit at the time of the star observations.

[2]Detector dark, bias and flat-field are measured in-flight during devoted calibration activities. For instance, the VL_BFF activity is devoted to the acquisition of bias and flat-field images for the VL channel and is performed by taking frames at the standard four polarization angles with a time exposition of 1 s plus two other quadruplets for two different integration times, while the Metis door is closed.

Table 3.1: Stellar targets used for the radiometric calibration

Star ID	Spectral type	V	R	Observation date	d_{Metis}	Coeff. $R_T \pm \sigma_{R_T}$	$\epsilon_{VL,*} \pm \sigma_*$
α Leonis	B8IVn	1.40	1.37	15 June 2020	0.51 au	1.14 ± 0.05	0.0126 ± 0.0007
ρ Leonis	B1Iab	3.87	3.90	17 June 2020	0.52 au	1.13 ± 0.04	0.0140 ± 0.0010
ν Scorpii	B2V	4.00	3.90	15 March 2021	0.64 au	1.16 ± 0.05	0.0141 ± 0.0006
β 01 Scorpii	B1V	2.62	2.60	15 March 2021	0.64 au	1.16 ± 0.05	0.0141 ± 0.0006
ω Scorpii	B1V	3.97	3.91	15 March 2021	0.64 au	1.16 ± 0.05	0.0128 ± 0.0014
λ Librae	B3V	5.03	$5.00^{(a)}$	15 March 2021	0.64 au	1.15 ± 0.05	0.0137 ± 0.0011
θ Ophiuchi	OB	3.26	3.38	25 March 2021	0.71 au	1.15 ± 0.04	0.0136 ± 0.0008

Notes: The Johnson-Cousins V, R apparent magnitudes of the target stars are listed in the third and fourth column. Starting date of the target observations is in the fifth column. Distances of Metis d_{Metis} to the Sun in astronomical unit (au), at the time of the observations, are in the sixth column. Values of the coefficient R_T and its σ_{R_T} (error propagation) in the seventh column (see Section 3.2.3). Values of the radiometric calibration factor for every star and its σ_* (standard deviation) are in the last column. Reported information is taken from the SIMBAD catalogue, with the exceptions of the last four columns.

$^{(a)}$: Value derived taking into account the spectral type of the star and the B and V apparent magnitudes. This magnitude is consistent with the value provided by the Gaia catalogue for the red band pass (Gaia Collaboration et al. 2016, 2022).

3.2.1 Availability of the stellar targets

The in-flight radiometric calibration of the two channels of Metis uses observations of stellar targets that pass across the FoV.

An accurate study on the availability of calibrating stellar targets was performed already before the launch of Solar Orbiter, on 10 February 2020. For this the Metis team took into account the peculiar orbit of Solar Orbiter by using the ESA/NASA SPICE (Spacecraft, Planet, Instrument, C-matrix (pointing), and Events) toolkit and considering the instrument characteristics (Focardi et al. 2014). Such analysis has to be refined after each spacecraft orbital correction (e.g., after gravity assisted maneuvers).

Due to its band pass (BP, 580-640 nm), the VL channel of Metis can be considered as a non-standard red filter and, thus, it is able to detect a significant amount of stars. As the instrument cannot acquire images at all times due to the telemetry constraints of an interplanetary mission, the choice of the available targets was driven by the overall needs of the Metis radiometric calibration campaigns, which prioritizes the observation of stars suitable for the calibration of the UV channel (see Chapter 4). Having a band pass of

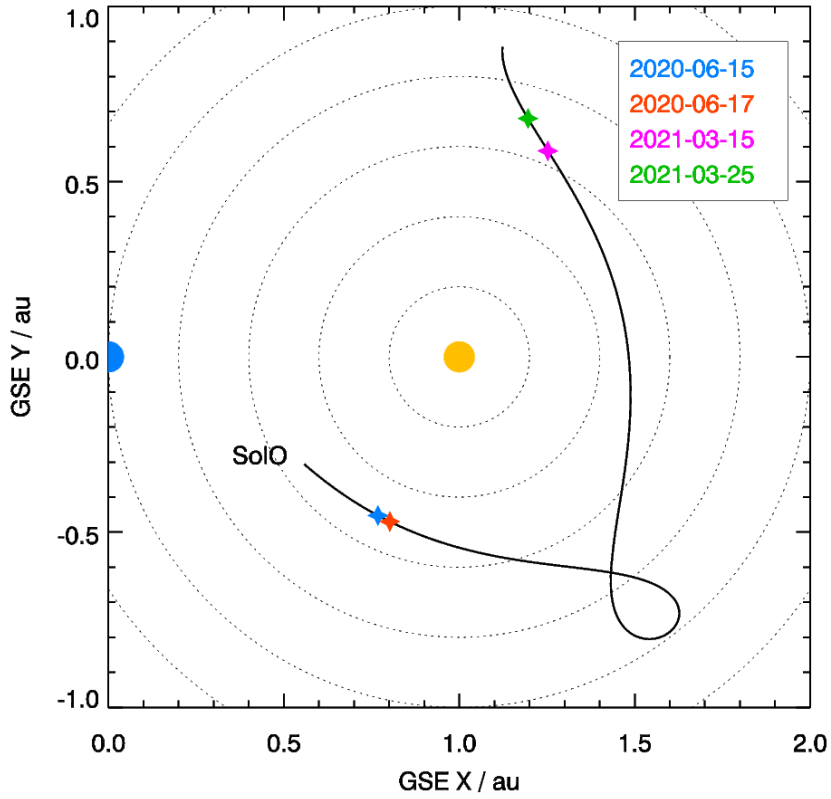

Figure 3.1: Position of Solar Orbiter for the star observations used, in Geocentric Solar Ecliptic (GSE) coordinate system: in this coordinate system, X is the Earth-Sun line, and Z is aligned with the north pole of the ecliptic. The dots representing Earth (blue) and Sun (yellow) are not in scale. The colored stars along the orbit mark the beginning of the Metis observations for each stellar target. See also Table 3.1.

121.6 ± 10 nm, Metis UV channel is expected to detect sufficient signal from bright stars of early spectral types: i.e. O and B. These stars have very stable UV spectra (Mihalas & Binney 1981) and, hence, are suitable for the calibration of UV instruments such as the Metis UV channel. Thus the few available calibration campaigns have been scheduled to cover the transits of this kind of stars.

The Metis team developed a tool for recognizing possible stellar targets, for plotting the expected stellar tracks on the FoV, and for retrieving useful quantities (stellar type, magnitude) via SIMBAD[3] (Wenger et al. 2000) queries. The tool uses the Metis boresight coordinates (RA and Dec) and the size of the square FoV (± 2.9 in width, ± 3.4 in the diag-

[3] https://simbad.u-strasbg.fr/simbad/sim-fid

onal directions) to query the SIMBAD catalogue and, then, it returns the stars coordinates in the sensor frame (2048 × 2048 pixels). The stellar objects observed during the Metis in-flight radiometric campaigns and used for the calibration of the VL channel are listed in Table 3.1, whereas their tracks within the FoV are shown in Figure 3.2. Some of the tracks are not complete due to limitations in the Solar Orbiter observing plan.

Besides the targets acquired during the dedicated calibration campaigns which are selected for their suitability, other stars are detected by the VL channel during normal science operations. Because these targets are acquired in observations not planned for calibration, they are of limited use and are not used for this analysis.

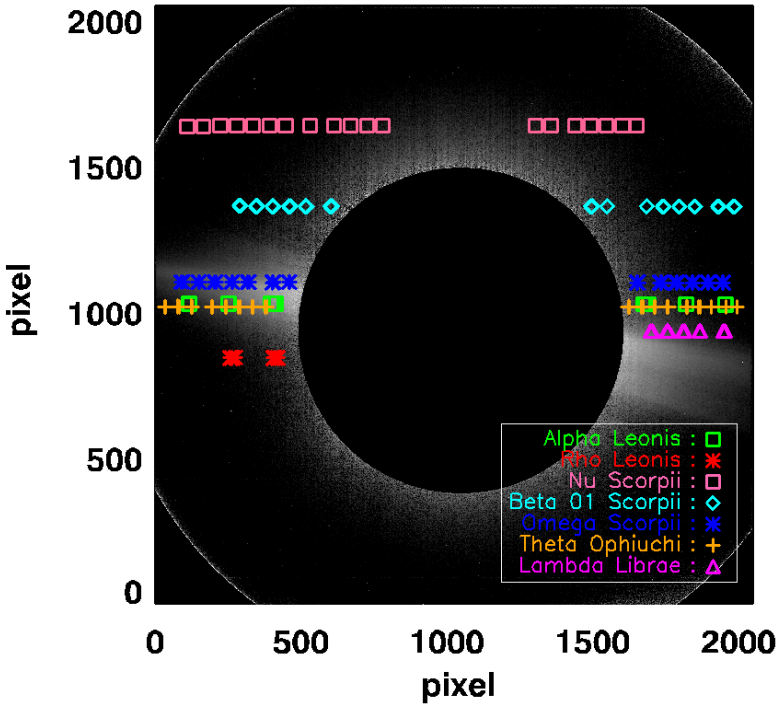

Figure 3.2: Map of the tracks of the stellar targets along the Metis VL field of view. The indicated stars compose the data set used to infer the radiometric calibration factor ϵ_{VL}. The backgroud image is the *pB* frame acquired on May 15, 2020, at 11:25 UT.

3.2.2 Aperture photometry

Once the frames from the radiometric calibration observations are acquired and pre-processed, it is possible to evaluate the star signal using the aperture photometry method. The frame

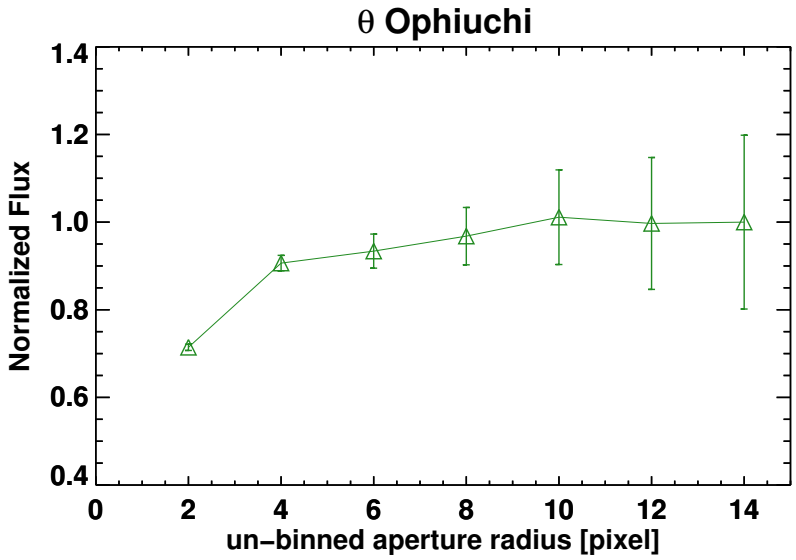

Figure 3.3: Measured flux of θ Ophiuchi as a function of the aperture radius in pixels. The image used was acquired on March 28, 2020, at 08:16 UT.

pre-processing consists of the removal of dark and bias, corrections for flat-field and "vignetting function" and the normalization for the exposure time.

The star count rate is obtained by summing the signal (DN) falling into a circular area of radius r_1 pixels around the center of the star image after subtracting the average coronal background (evaluated by averaging the signal in DN in the annular area of inner radius r_1 pixels and outer radius r_2 pixels).

The determination of the best choice for the circular area radius r_1 took into account the PSF of the instrument and, when applicable, the binning factor of the considered frame. Considering that the full width half maximum (FWHM) of the Metis PSF ranges from 1.5 to 3 pixels throughout the FoV in the VL channel (Da Deppo et al. 2021), I chose a radius r_1 of eight pixels for our measurements. In case of data binned aboard, r_1 and r_2 have been divided by the binning factor of the frame. The outer radius r_2 was set to 12 pixels (value for the case of no binning).

Figure 3.3 shows the stellar flux growth as a function of the photometry radius. The variation of the star signal is about few percent in the neighborhood (8 ± 2 pixels) of the chosen value of the aperture.

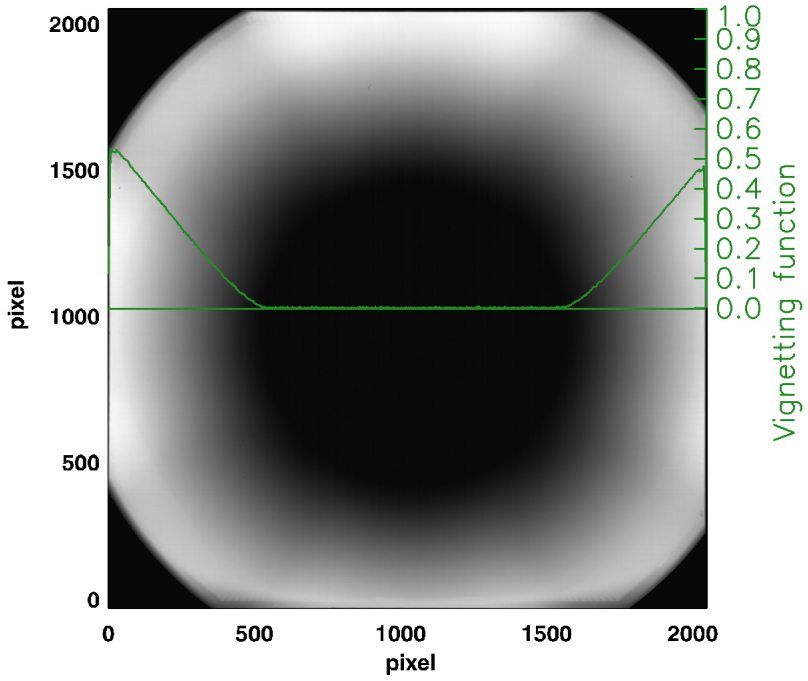

Figure 3.4: Map of the vignetting function measured on-ground and its trend along the equatorial direction (solid line in green).

Another important step of the frame processing before proceeding with the calibration is the vignetting function (VF) correction. One characteristic of externally occulted coronagraphs is that their FoV is highly vignetted (see Figure 3.4). Thus, a correction for the VF is required, to remove the artificial variation of the stellar flux along its track on the FoV. The VF map was measured during the on-ground calibration campaign (Antonucci et al. 2020) and was corrected after the in-flight adjustment of the internal occulter (Liberatore et al. 2021). I checked that the values of the star signal along the FoV are in good agreement with the VF trend for every considered data set. As an example, Figure 3.5 (left panel) shows the signal of β 01 Scorpii along the FoV of the VL channel and the values of the vignetting function. The right panel of Figure 3.5 shows the star signal corrected for the VF trend: the general trend is the expected one, except for a few points with a decreasing trend close to the inner limit of the FoV. The star observations give a relative measurement of the VF, and indeed a deviation from the pre-flight VF measurement is the likely explanation for the non-uniformities shown in Figure 3.5 (this effect will be discussed in Section 3.2.5).

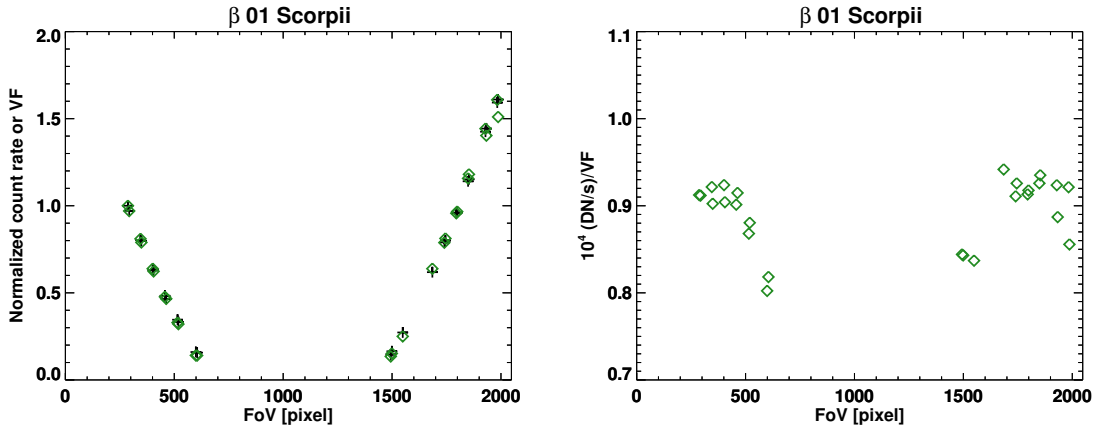

Figure 3.5: Left panel: Comparison between the normalized count rate (green diamonds) of β 01 Scorpii and the normalized VF (black crosses). The VF is evaluated in the same positions of the star, along the FoV. Both the trends have been normalized to the value of the first frame of this observation. Right panel: trend of the count rate corrected for the VF.

3.2.3 The Metis photometric response

As already explained in Section 2.2.3, the Metis VL detection system consists of a VL camera equipped with a CMOS APS, 2k $\times$ 2k, 10 μm pixel (VLDA), installed at the end of the visible light optical path, following the interferential filter assembly (IFA) and the polarimeter assembly. The IFA is an interferential Al/MgF_2 multilayer filter deposited on a MgF_2 crystal flat window, perpendicular to the optical axis. This element has the double purpose of selectively transmitting the H I Ly-α radiation to be detected by the UV detector assembly (UVDA), and of reflecting the visible light into the Metis polarimeter that selects the wavelength band 580-640 nm (Antonucci et al. 2020; Casti et al. 2019).

The VL channel can be assimilated to a non-standard red filter. Thus, in order to determine the fluxes of the radiometric stellar targets, it is necessary to determine the conversion factor between the Metis non-standard photometric system and a standard one (Johnson-Cousins system or JC system), for which stars photometric data are known (Bessell et al. 1998). The conversion coefficient called R_T is star dependent, and in first approximation, spectral type dependent. R_T is given by the ratio between the averaged flux emitted by the star in the Metis band pass and the averaged flux in the standard JC red filter band pass:

$$R_T = \frac{\overline{f}_{Metis}}{\overline{f}_R} \tag{3.1}$$

with averaged fluxes defined as follows:

$$\overline{f}_{Metis} = \frac{\int f_\lambda T_{Metis}\, d\lambda}{\int T_{Metis}\, d\lambda} \qquad \overline{f}_R = \frac{\int f_\lambda T_R\, d\lambda}{\int T_R\, d\lambda},$$

where T_{Metis}, T_R are the transmission curves of the Metis BP filter and of the JC red filter, respectively. The transmission curve of the Metis BP filter is reported in Figure 3.6. The

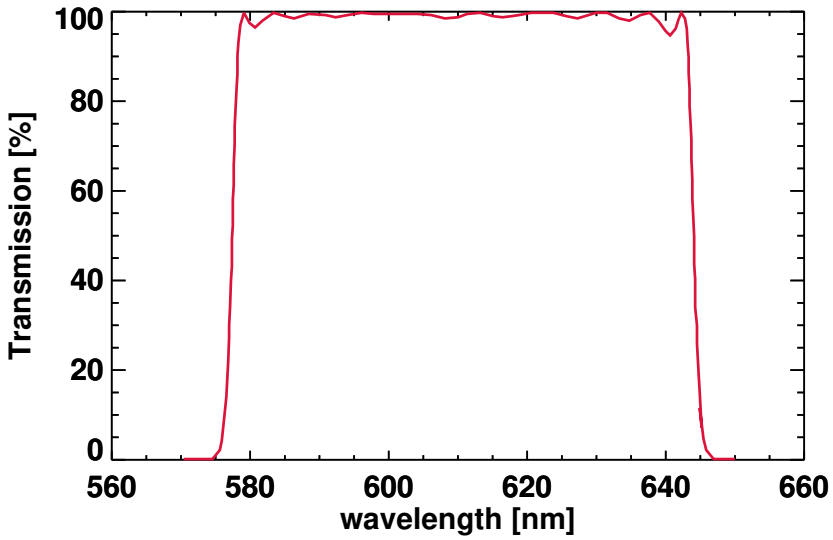

Figure 3.6: Transmission curve of the Metis VL band pass filter.

evaluation of the coefficient R_T was made by using about 50 synthetic star spectra f_λ from the ESO library of Stellar Spectra[4], with the aim of deriving the conversion coefficient R_T as a function of the spectral type. Detailed information about the stellar spectra in the catalogue can be found in Ivanov et al. (2004).

The interstellar extinction and reddening are neglected here because the stellar targets are all in the vicinity of Earth.

As a second step, I determined the star flux received by the instrument in the JC red filter band pass for a given star magnitude m_R. To do it we need to know the R band pass flux for stars with null red magnitude, the so-called *zero point*[5] flux. At this point, the JC

[4] `https://www.eso.org/sci/facilities/paranal/decommissioned/isaac/tools/lib.html`

[5] The *zero point* flux is the main star flux of a photometric calibration system evaluated for each band, that corresponds to the zero magnitude star.

red magnitude of a stellar target can be written as:

$$m_R - m_{R0} = -2.5 \log \frac{\overline{f}_R}{f_{R0}} \tag{3.2}$$

with $\overline{f}_R$ the received flux in the JC R and f_{R0} the zero point flux (Bessell et al. 1998). From Equations (3.1) and (3.2) the expected Metis flux for the star is obtained:

$$\overline{f}_{Metis} = R_T \cdot \overline{f}_R = R_T \cdot f_{R0} \cdot 10^{\frac{-(m_R - m_{R0})}{2.5}} . \tag{3.3}$$

Finally, the estimated count rate N_{VL} is

$$N_{VL} = \overline{f}_{Metis} \cdot A_{pup} \cdot VF\,(\mathrm{FoV}) \cdot \epsilon_{VL} \cdot \Delta\lambda_{VL}\,, \tag{3.4}$$

where A_{pup} is the pupil area of the telescope, VF is the value of the VF that depends on the pixel coordinates of the frame and $\epsilon_{VL} \cdot \Delta\lambda_{VL}$ is the overall efficiency of the VL channel times the band width defined by the transmission curve of the Metis BP filter.

3.2.4 On-ground calibration

The full system VL channel efficiency has been measured for the first time during the on-ground calibration campaign at the INAF Optical Payload Systems facility (Fineschi et al. 2019). The radiometric response and the vignetting function in the visible light were obtained using a LED flat-field source that illuminated uniformly the entrance pupil and the full Metis FoV. A diode calibrated at US National Institute of Standards and Technology (NIST), equipped with a Metis VL band pass filter, measures the Flat Field LED panel light intensity. By combining the measurements of the source with the diode and the Metis telescope, the product of the VF by the VL channel efficiency is obtained, $VF\,(\mathrm{FoV}) \cdot \epsilon_{VL}$. The vignetting function is an adimensional quantity that depends on the pixel coordinates on the frame. It is separated from the VL efficiency by using a VL efficiency value determined from the optical elements efficiencies measurements at sub-system level. The value for the VL efficiency is 0.118 ± 0.022 photo-electrons per photon impinging the entrance pupil (Antonucci et al. 2020). This value can be divided by the detector gain 8.4 ± 0.3 photo-electrons per DN to achieve the VL efficiency of 0.014 ± 0.003 DN/photon. The in-flight calibration aims at verifying, monitoring and possibly improving the accuracy of this number.

3.2.5 Data inversion and calibration across the FoV

By considering the star count rate N_{VL}, each star measurement provides the value of the coefficient ϵ_{VL} , which can be derived from Equation 3.4:

$$\epsilon_{VL} = \frac{N_{VL}(\text{FoV})}{\overline{f}_{Metis} \cdot A_{pup} \cdot VF\,(\text{FoV}) \cdot \Delta\lambda_{VL}}. \tag{3.5}$$

Figure 3.7 shows the results from the inversion of the data set, which consists of seven stars (see Table 3.1). For each of them I obtained the values of the ϵ_{VL} related to the positions across the FoV, as a function of radial distance from the center of the internal occulter. The error bars are the standard deviations σ_* of the radiometric calibration factor, computed from the data set of each stellar target. The horizontal gray solid line represents the ϵ_{VL} value from the on-ground campaign, the two gray dashed lines delimit the 1σ tolerance range around the central value. The red solid line indicates the ϵ_{VL} value estimated as the average of the whole data set. This value with its standard deviation 1σ is equal to 0.014 ± 0.001 DN/photon. The uncertainty of the radiometric calibration factor is evaluated as the standard deviation around the average value from the whole data set.
The radiometric calibration factor determined in the vicinity of the occulter (see the black vertical line in Figure 3.7) varies with approaching to the inner edge of the FoV. There is a hypothesis that might explain this effect, as described later on. I obtained that the two radiometric calibration factors values are consistent within the uncertainties.

Although the results from the on-ground and the in-flight calibration campaigns are in good agreement, some of the stellar targets, in particular β 01 Scorpii, ω Scorpii and θ Ophiuchi, present a clear decreasing trend in the zone nearby the occulter (within a distance of about 200 pixels from the edge of the occulter).

The most likely explanation of this unexpected trend is an overestimate of the VF, likely due to the presence of stray light nearby the occulter when the throughput of the instrument was measured on-ground. Infact, in the ideal case, a proper correction of the data with VF should result in a constant value of the flux of each star. In addition to this, the star signal is significantly distorted near the occulter due to diffraction making the estimate of the stellar flux more difficult.

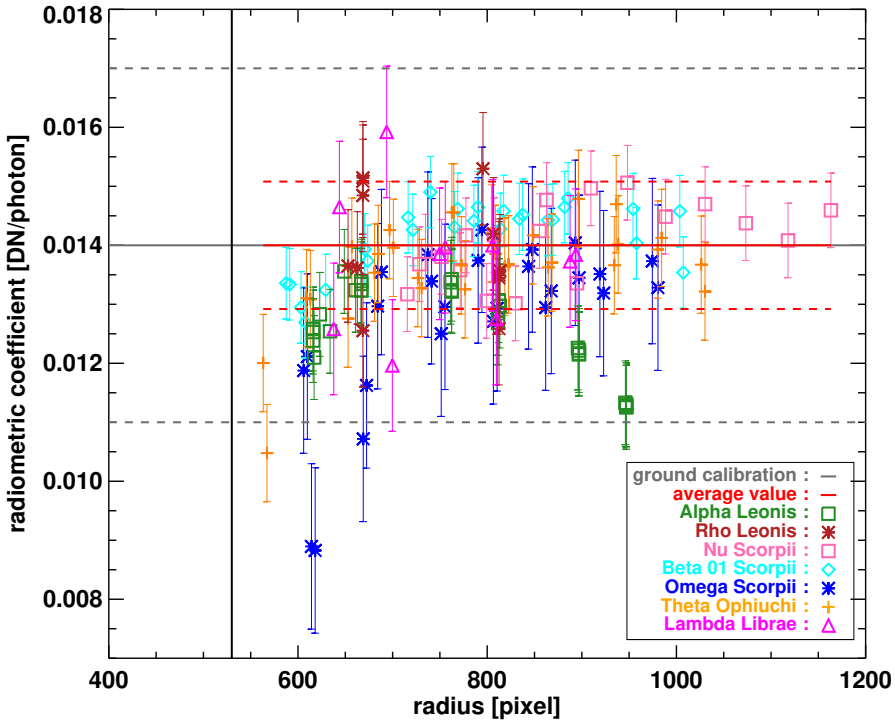

Figure 3.7: Radiometric calibration factors as a function of the radial distance of the star images from the center of the occulter. The solid red line is the average value of ϵ_{VL}. The solid gray line represents the on-ground value of the radiometric calibration factor. The gray and red dashed lines depict the uncertainties of the on-ground and in-flight radiometric factors, respectively (see the text for more details). The vertical black solid line is the radius of the internal occulter in pixels.

Chapter 4

In-flight radiometric calibration of the UV channel of Metis

4.1 Introduction

The topic of this chapter is the radiometric calibration I performed for the UV channel of Metis. The analysis is taken from De Leo et al. 2023, paper B[1].

As already remarked, the radiometric calibration is a necessary procedure for obtaining the absolute brightness data of the solar corona from the images acquired with the UV channel during the mission. The in-flight radiometric calibration presented here is based on the observation of stellar targets transiting Metis FoV and it is aimed at inferring the radiometric calibration factor ϵ_{UV}. Stars with known and stable fluxes are ideal targets to verify the radiometric response of the instrument and monitor it over time. Moreover stars, being point sources, are very useful to characterize the instrumental spatial resolution by gaining information on its *point spread function* (PSF). The obtained radiometric calibration is then used to convert the observed Digital Numbers (DNs) per pixel into photons and to express the calibrated UV frames in radiance (photons cm^{-2} sr^{-1} s^{-1}).

[1] Section 4.2 to Section 4.3 are Sect. 1, Sect. 2 and the Appendix (after a rewording) in the peer reviewed publication De Leo et al. 2023, paper B, to be submitted to *Astronomy&Astrophysics*.

4.2 The Metis UV channel radiometric calibration

The approach presented below is similar to that used for the calibration of the Metis VL channel, which is described in De Leo et al. 2023, paper A and in Chapter 3 of this thesis. The images are first corrected by removal of dark and bias signal and for flat-field and vignetting patterns. Then the signal is transformed into count rates by dividing for the exposure time. After these passages, the count rates from calibration stars should be constant across the field of view (as it is the case for the VL channel). Instead, the observations reveal a marked response disuniformity across the FoV. This was corrected by applying a further spatial correction before inverting the star data, as described in Section 4.2.6. Finally, I optimized the correction by performing a statistical analysis on the star data set, as explained in Section 4.2.7.

The application of the radiometric calibration factor is the final passage that transforms the count rates in DN/s into physical units (photons cm^{-2} sr^{-1} s^{-1}). The produced L2 data contain also the uncertainty matrix that takes into account the full error propagation from the steps mentioned above.

The data used for this analysis cover a time range from June 2020 (observations of α and ρ Leonis) until August 2021 (observation of 121 Tauri), as reported in Table 4.1. In Figure 4.1 the positions of Solar Orbiter along its orbit at the time of the star observations are shown.

4.2.1 Availability of the stellar targets

The method to perform the radiometric calibration of the two channels of Metis exploits observations of stellar targets transiting the FoV. As anticipated in Section 3.2.1, an accurate study on the availability of calibrating stars was performed before the launch of Solar Orbiter, on 10 February 2020. The Metis team made use of the ESA/NASA SPICE (Spacecraft, Planet, Instrument, C-matrix (pointing), and Events) toolkit considering the peculiar orbit of Solar Orbiter and the instrument characteristics (Focardi et al. 2014). Such analysis has to be refined after every spacecraft orbital correction (e.g., after gravity assisted maneuvers). Furthermore, as Metis cannot acquire images at all times due to the telemetry constraints of an interplanetary mission, the choice of the available targets was driven by the overall needs of the radiometric calibration campaigns, which prioritizes the observa-

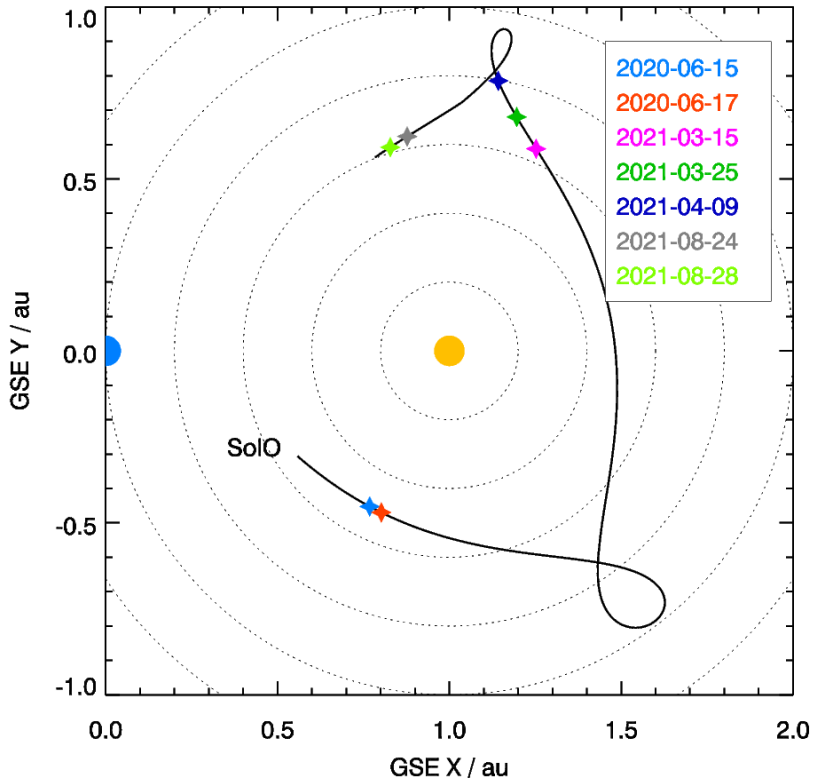

Figure 4.1: Position of Solar Orbiter for the star observations used, in Geocentric Solar Ecliptic (GSE) coordinate system. The dots representing Earth (blue) and Sun (yellow) are not in scale. The colored stars along the orbit mark the beginning of the Metis observations for each stellar target. See also Table 4.1.

tion of stars suitable for the calibration of the UV channel (as those are in most of the cases also suitable for the calibration of the VL channel).

Having a band pass of 121.6 ± 10 nm, Metis UV channel is expected to detect sufficient signal from bright stars of early spectral types, like O and B stars. These stars have very stable UV spectra (Mihalas & Binney 1981) and, hence, are suitable for the calibration of UV instruments such as the Metis UV channel. Therefore calibration campaigns have been scheduled to cover the transits of these targets.

The recognition of possible stellar objects, the expected stellar track on the FoV, and the retrieving of useful quantities (stellar type, magnitude) is performed by a tool developed by the Metis team, via SIMBAD queries. The tool uses Metis square FoV ($\pm 2.9°$ in width) and

Table 4.1: Stellar targets used for the radiometric calibration of the UV channel

Star ID	Spectral type	U	V	Observation date	d_{Metis}	flux $f_* \pm \sigma_{f_*}$	$\epsilon_{UV,*} \pm \sigma_*$
α Leonis$^{(a,b)}$	B8IVn	0.88	1.40	15 June 2020	0.51 au	$(31 \pm 2) \times 10^3$	0.23 ± 0.03
ρ Leonis$^{(b)}$	B1Iab	2.78	3.87	17 June 2020	0.52 au	$(15 \pm 2) \times 10^3$	0.22 ± 0.02
ν Scorpii$^{(b)}$	B2V	3.42	4.00	15 March 2021	0.64 au	$(8.9 \pm 0.9) \times 10^3$	0.19 ± 0.03
β01 Scorpii$^{(b)}$	B1V	1.68	2.62	15 March 2021	0.64 au	$(68 \pm 8) \times 10^3$	0.23 ± 0.06
δ Scorpii$^{(a)}$	B0.3IV	1.30	2.32	15 March 2021	0.64 au	$(119 \pm 9) \times 10^3$	0.23 ± 0.04
ω Scorpii$^{(b)}$	B1V	3.10	3.97	15 March 2021	0.64 au	$(16 \pm 2) \times 10^3$	0.23 ± 0.04
λ Librae$^{(b)}$	B3V	4.43	5.03	15 March 2021	0.64 au	$(3.5 \pm 0.6) \times 10^3$	0.21 ± 0.01
θ Ophiuchi$^{(b)}$	OB	2.18	3.26	25 March 2021	0.71 au	$(48 \pm 6) \times 10^3$	0.26 ± 0.07
σ Sagittarii$^{(a)}$	B2V	1.06	2.07	09 April 2021	0.80 au	$(126 \pm 10) \times 10^3$	0.20 ± 0.08
τ Tauri$^{(b)}$	B3V	N.A.	4.26	24 August 2021	0.63 au	$(9 \pm 1) \times 10^3$	0.17 ± 0.02
121 Tauri$^{(b)}$	B2.5IV	4.67	5.38	28 August 2021	0.62 au	$(3.4 \pm 0.4) \times 10^3$	0.15 ± 0.02
							0.21 ± 0.03

Notes: The Johnson-Cousins U, V apparent magnitudes of the target stars are listed in the third and fourth columns. Starting date of the target observations is in the fifth column. Distances of Metis d_{Metis} to the Sun in astronomical unit (au), at the time of the observations, are in the sixth column. Values of the UV H I Ly-α flux f_* (in photons cm^{-2} s^{-1}) and its uncertainty σ_{f_*} are in the seventh column (see Sect. 4.2.5). Values of the radiometric calibration factor for every star and its σ_* (standard deviation) are in the last column. Reported information is taken from the SIMBAD catalogue, with the exceptions of the last four columns. The Metis radiometric calibration factor ϵ_{UV} (in DN/photon) is obtained as the average of the calibration factors obtained for the individual stars (last column) and it is reported beneath the last column together with its standard deviation.
$^{(a)}$: SPICAM, $^{(b)}$: IUE.

the boresight coordinates (RA and Dec) to query the SIMBAD[2] catalogue (Wenger et al. 2000) and, then, returns the stars coordinates in the sensor frame (1024 × 1024 pixels). The stellar targets used for the calibration of the UV channel are listed in Table 4.1, whereas their tracks within the FoV are shown in Figure 4.2.

4.2.2 UVDA dark optimization

At the time of the radiometric calibration observations used in this work the UV detector was affected by a transient effect at the beginning of each acquisition sequence. An exhaustive description of this effect can be found in Andretta et al. 2021 and Russano et al. 2023.

[2] `https://simbad.u-strasbg.fr/simbad/sim-fid`

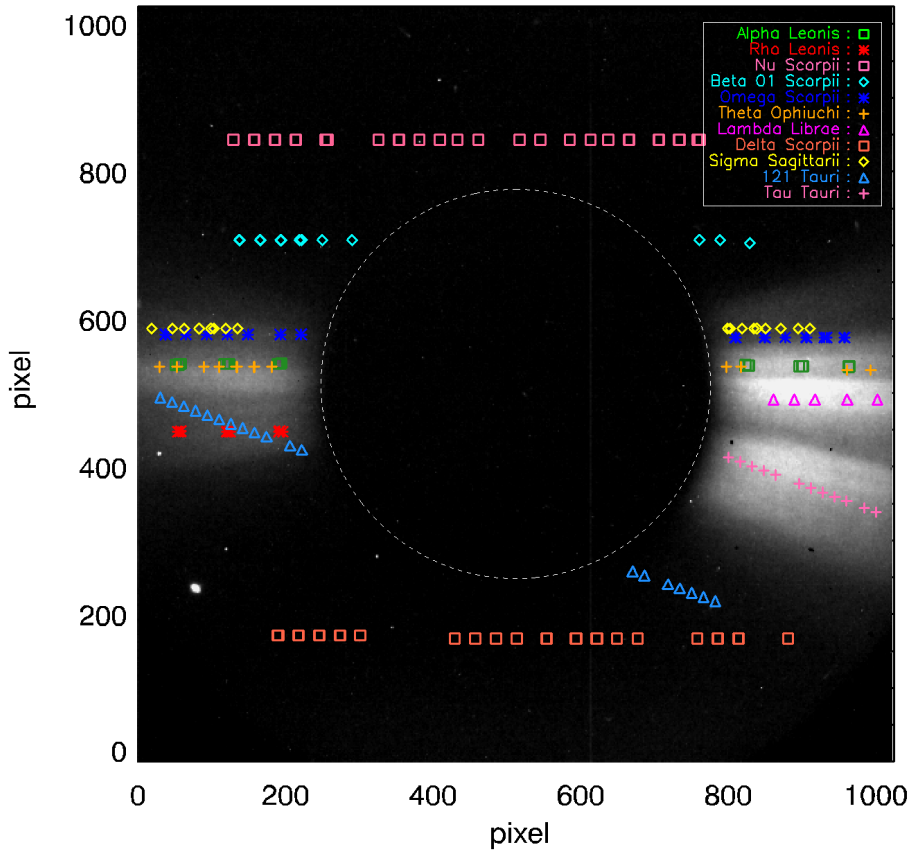

Figure 4.2: Map of the tracks along the Metis UV field of view of the stellar targets used to infer the radiometric calibration factor ϵ_{UV}. The background UV image was acquired on January 16, 2021, at 12:31 UT.

Thus, I discarded the very first frame of each radiometric calibration sequence.

This effect afflicts only few images if the frames are acquired individually, while it compromises all the images averaged on board. In the latter case the effect depends on the combination of the used acquisition parameters (as the cadence, the exposure time DIT, or the number of on board averaged images NDIT) and the acquisitions of set of dark frames were planned with the same parameters used for science observations. The correction for the dark counts was done using the suitable dark frames closer in time to the analyzed radiometric calibration observations.

However, variations in the dark level on short time were also noticed. This could explain why dark frames acquired even few hours later may not properly correct the images. An accurate analysis showed that the variations are not consistent with purely offset or purely

gain variations, but with a linear combination of them. Using the average values of five boxes located in the non-illuminated areas of the detector (in addition to the area behind the occulter, there are four corners not illuminated by the round fiber optic taper which connects the intensifier to the sensor), it was possible to compute the optimal dark subtraction for each calibration image, since these boxes do not contain signal during observations. Most of these problems have been solved or strongly mitigated by a software update in mid-2022.

4.2.3 Vignetting function correction

Before proceeding with the calibration, I performed another important step of the frame processing: the vignetting function (VF) correction. The FoVs of externally occulted coronagraphs are highly vignetted (see Figure 4.3). Thus, a correction for the VF is required to remove the artificial variation of the stellar flux along its track on the FoV. The VF map used for the UV channel is the one used for the VL channel, after a proper shift necessary to align its center with the in-flight center of the Internal Occulter (IO) and rebinning its size in order to match that of the UV frame. During the on ground calibration campaign of the instrument (Antonucci et al. 2020), the VF map was measured and then was corrected after the in-flight adjustment of the internal occulter (Liberatore et al. 2021).

4.2.4 Aperture photometry

Once the frames from the radiometric calibration observations are acquired and pre-processed, it is possible to evaluate the star signal using the aperture photometry method as explained in detail in Section 3.2.2. Briefly, it consists in making the difference between the signal measured over a circle of radius r_1 centered on the star and the corresponding background, proportionally calculated over an annular region with the same center, inner radius r_1 and outer radius r_2.

The best choice for the aperture radii r_1 and r_2 used for the background subtraction took into account the PSF of the instrument and the binning factor of the considered frame (when applicable). Considering that the full width half maximum (FWHM) of the Metis PSF ranges from 4 to 6.5 pixels throughout the FoV in the UV channel (Da Deppo et al. 2021), for our measurements we chose a radius r_1 of 12 pixels and r_2 of 16 pixels. In case of data binned aboard, r_1 and r_2 have been divided by the binning factor of the frame.

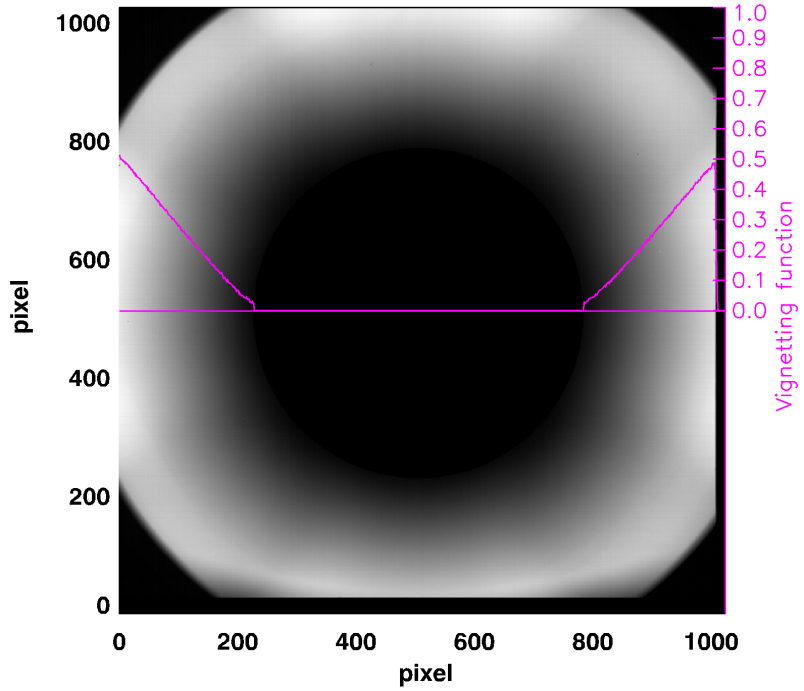

Figure 4.3: Map of the VL vignetting function measured on-ground and adapted to the UV channel characteristics. The solid line in magenta is the trend along the equatorial direction. Image is in detector (pixels) coordinates.

Figure 4.4 shows the stellar flux growth as a function of the photometry aperture radius r_1. The variation of the star signal is about few percent for aperture radii larger than 10 pixels.

4.2.5 Metis UV photometric response

As described in Section 2.2.3, the Metis UV detector assembly (UVDA) consists of three main elements: (1) an intensifier, consisting of a micro channel plate (MCP) with KBr photocatode and a phosphor output screen, in optical contact with (2) a fiber optics 2:1 de-magnifying coupler connected to (3) a CMOS APS STAR1000 (1k $\times$ 1k format, 15 μm square pixel). The UVDA is installed at the end of the Metis UV channel optical train consisting of the occulting sub-system, the telescope and the interferential filter assembly

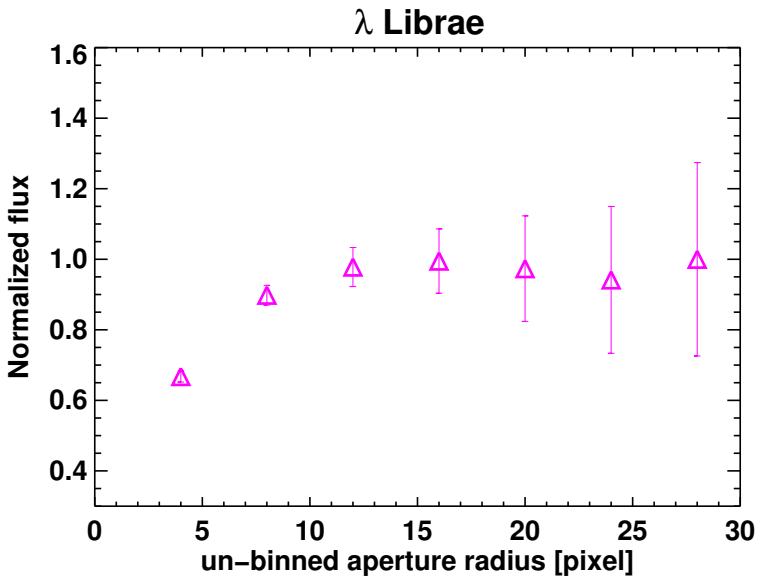

Figure 4.4: Measured flux of λ Librae as a function of the aperture radius in pixels. The image was acquired on November 19, 2021, at 19:32 UT.

(IFA, Antonucci et al. 2020, Fineschi et al. 2020). The IFA is an interferential Al/MgF_2 multilayer filter deposited on a MgF_2 crystal flat window, perpendicular to the optical axis. This element has the double purpose of selectively transmitting the H I Ly-α radiation to be detected by the UVDA, and of reflecting the visible light into the Metis VL channel. The High Voltage Unit (HVU) provides the high voltages required by the intensifier.

In order to determine the fluxes f_* of the radiometric stellar targets in the UV narrow band, I calculated the results of the convolution of the UV spectra with the transmission curve of the interferential filter and the spectral response of the detector.
In fact, the count rate N_{UV} for each star is given by the equation:

$$\begin{aligned} N_{UV} &= \left[\int f_{*,\lambda}\cdot\epsilon_{F,\lambda}\cdot\epsilon_{UVD,\lambda}\,d\lambda\right]\cdot{\epsilon_M}^2\cdot A_{pup}\cdot VF\,(\mathrm{FoV}) = \\ &= \left[\int f_{*,\lambda}\cdot\phi_F(\lambda)\cdot\phi_{UVD}(\lambda)\,d\lambda\right]\cdot\epsilon_{F,121.6}\cdot\epsilon_{UVD,121.6}\cdot \\ &\cdot{\epsilon_M}^2\cdot A_{pup}\cdot VF\,(\mathrm{FoV}) = \\ &= f_*\cdot\epsilon_{UV}\cdot A_{pup}\cdot VF\,(\mathrm{FoV}) \end{aligned} \tag{4.1}$$

where $f_{*,\lambda}$ is the star spectrum, $\epsilon_{F,\lambda} = \epsilon_{F,121.6}\cdot\phi_F(\lambda)$ is the spectral profile of the filter transmission and $\phi_F(\lambda)$ the spectral profile normalized to the filter transmission at H I Ly-

α 121.6 nm, $\epsilon_{UVD,\lambda} = \epsilon_{UVD,121.6} \cdot \phi_{UVD}(\lambda)$ is the MCP spectral response and $\phi_{UVD}(\lambda)$ is the spectral profile normalized to the UVD quantum efficiency at H I Ly-α 121.6 nm (see Fig.15 of Antonucci et al. 2020), ϵ_M is the reflectivity of the telescope mirrors that can be assumed constant within the band pass, A_{pup} is the telescope aperture, given by the external occulter stop, and $VF\,(\mathrm{FoV})$ is the vignetting function, whose values depend on the position across the FoV.

The star spectra, $f_{*,\lambda}$, in the UV band pass, that can be observed only from space, are from the International Ultraviolet Explorer (IUE) experiment (Willis 2013), and from the SPectroscopy for the Investigation of the Characteristics of the Atmosphere of Mars (SPICAM) experiment (Bertaux et al. 2006). In Equation 4.1, the Metis efficiency (or

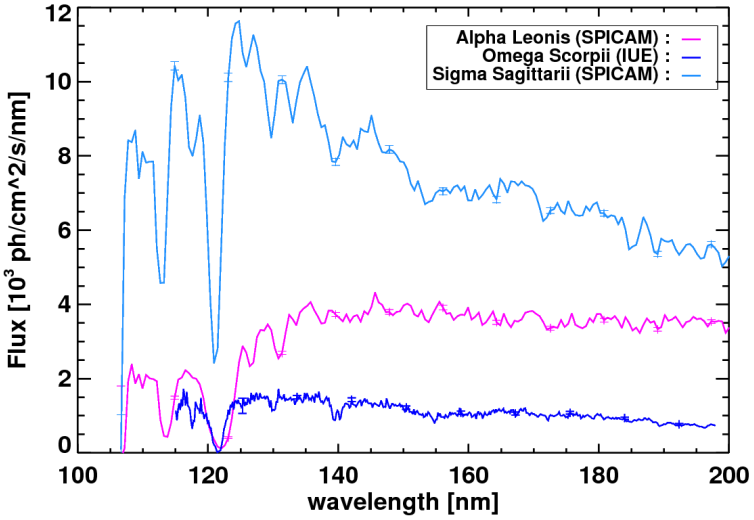

Figure 4.5: Spectra of α Leonis, ω Scorpii and σ Sagittarii. Not all the error bars are shown for plot clarity.

radiometric calibration factor) at H I Ly-α 121.6 nm is defined as

$$\epsilon_{UV} = \epsilon_{F,121.6} \cdot \epsilon_{UVD,121.6} \cdot {\epsilon_M}^2 \tag{4.2}$$

and the star flux integrated in the UV pass band as

$$f_* = \int f_{*,\lambda} \cdot \phi_F(\lambda) \cdot \phi_{UVD}(\lambda)\, d\lambda. \tag{4.3}$$

In Table 4.1 the values of the fluxes f_*, for each measured star, are reported with their uncertainties from error propagation (which takes into account the uncertainties of the spectrum,

of the filter trasmission curve and of the MCP spectral response). Figure 4.5 shows some of the UV stellar spectra used in this analysis.

4.2.6 Correction for spatial disuniformity and data inversion

The radiometric calibration factor ϵ_{UV} (in DN/photon) is estimated by inverting the star signal N_{UV} obtained from the aperture photometry, as follows:

$$\epsilon_{UV}(\mathrm{FoV}) = \frac{N_{UV}\,(\mathrm{FoV})}{f_* \cdot A_{pup} \cdot VF\,(\mathrm{FoV})}. \tag{4.4}$$

In the ideal case (like for the VL channel), the vignetting function correction removes completely the dependency of the star count rate on the position across the FoV and the radiometric calibration factor has a constant value. As an example of our observations, Figure 4.6 (left panel) shows the signal of β 01 Scorpii along the FoV of the UV channel and the corresponding values of the vignetting function. The right panel of Figure 4.6 shows the star signal corrected for the VF trend.

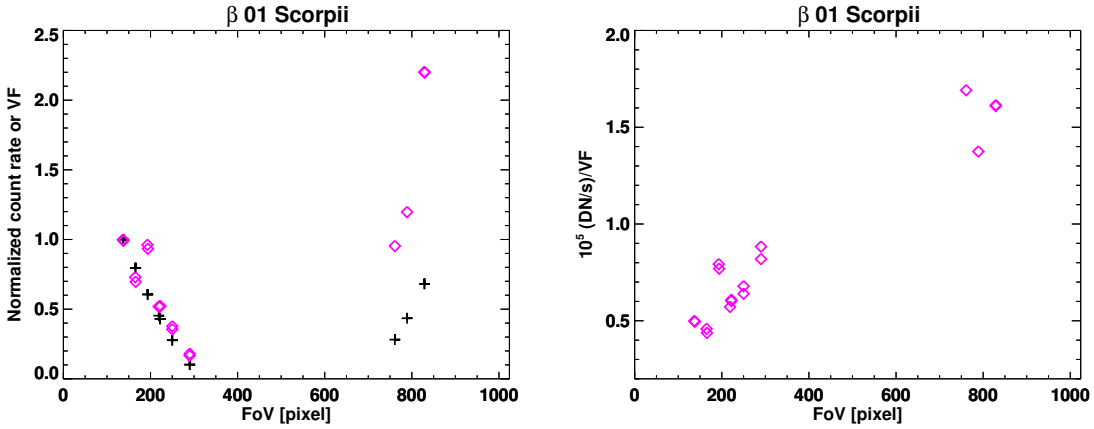

Figure 4.6: Left panel: Comparison between the normalized count rates (magenta diamonds) of β 01 Scorpii and the normalized VF (black crosses). The VF is evaluated in the same positions of the star along the FoV. Both the trends have been normalized to the value of the first frame of this observation. Right panel: Trend of the count rates corrected for the VF. In both panels a discrepancy between the star signal and the VF trend is evident, on the East and the West sides of the UV detector.

A discrepancy in the response is evident between the East side and the West side of the detector. It reflects the fact that the radiometric factor depends on the position across the

FoV. This unexpected result has been extensively investigated and is present in all of the stars data analyzed.

Thus, it is necessary to correct spatially the trend of the data to proceed with their inversion.

As explained in Andretta et al. 2021, to correctly account the evident disuniformity of the stars signal across the FoV, we applied the results of an investigation of the relative efficiency of the VL and UV channels of Metis. The adopted method exploits the fact that the Metis heat shield (HS) door is not light-tight. Even when it is closed a significant amount of light diffuses into the instrument. Thereafter, the Metis team modeled the spatial correction mentioned above by using the back-illuminated door frames first obtained as a flat field test, then used specifically to monitor the variation of the UV channel efficiency across the detector. By assuming that the ratio of brightness of the UV and VL closed-door frames is approximately constant in every point across the FoV, the ratio of the images of both channels provides the map, $M_{UV2VL}\,(\mathrm{FoV})$, of the variability of the relative efficiency over the FoV. The back-illumination of the Metis door mainly comes from the light diffused by the heat shield, and in particular by its multilayer surface. Since it is a single type of surface that diffuses light on the back of the door, then we can assume that the ratio of the VL and UV intensities is uniform. The map $M_{UV2VL}\,(\mathrm{FoV})$ is obtained as the ratio of the fitting of the original VL and UV back-illuminated door frames, averaged on the radial direction to reduce small-scale variability. $M_{UV2VL}\,(\mathrm{FoV})$ shows an evident gradient in the azimuthal direction (see Figure 4.7). This model is applied as an improvement of the standard UV vignetting function for every star of the data set. The map is normalized in the small square region of 65×65 pixels shown in Figure 4.7. This area was originally selected for normalization because it is the region that was measured during the on ground calibration campaign and would make the comparison between flight and on ground calibration easier. The results from these calibration campaigns are different and the comparison with the on ground calibration campaign is still under investigation.

The four panels in Figure 4.8 show a comparison between the star count rates of β 01, ν, ω Scorpii, and 121 Tauri, corrected with the standard and spatially corrected VF.

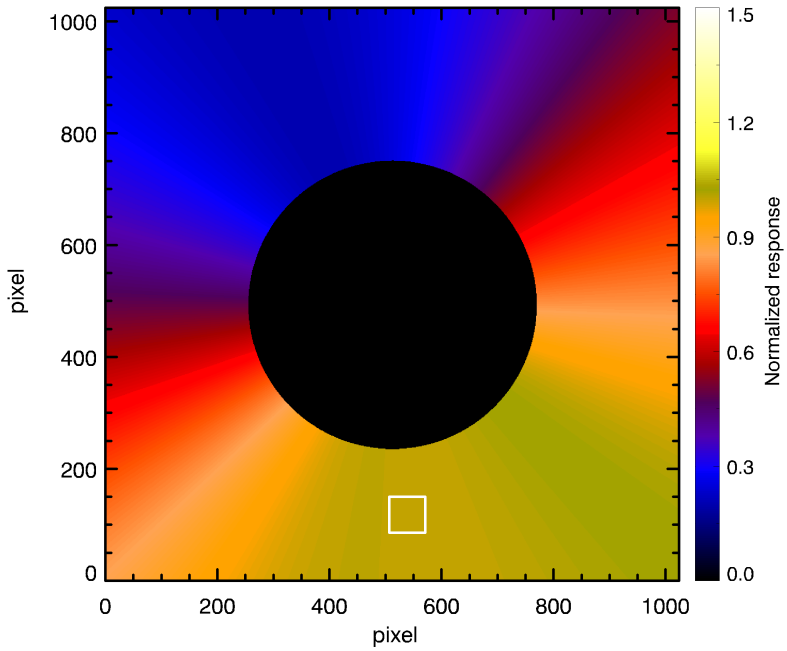

Figure 4.7: Spatial correction map $M_{UV2VL}\,(\mathrm{FoV})$ modeled by using the back-illumination door frames. The white square indicates the normalization region. See the text for more details. Image is in detector (pixels) coordinates.

4.2.7 Refining the spatial correction across the FoV

With the scope of optimizing the spatial correction used, I performed a statistical analysis of the obtained values of the radiometric calibration from each image of the star data set. Figure 4.9 (left panel) shows a spatial distribution of the absolute differences between the radiometric calibration factors (evaluated in the positions of each star within the detector frame) and the average radiometric calibration factor from the whole data set. A visual analysis of the left panel of Figure 4.9 shows a systematic trend in the differences distribution. To minimize it, I applied a linear correction to the UV-to-VL ratio map $M_{UV2VL}\,(\mathrm{FoV})$. Given the relatively few star points across the FoV, there are not enough constraints to attempt using a more complex surface. The linear correction was applied to the vertical direction only and was set to be equal to 1 in the region chosen for normalization. Thus,

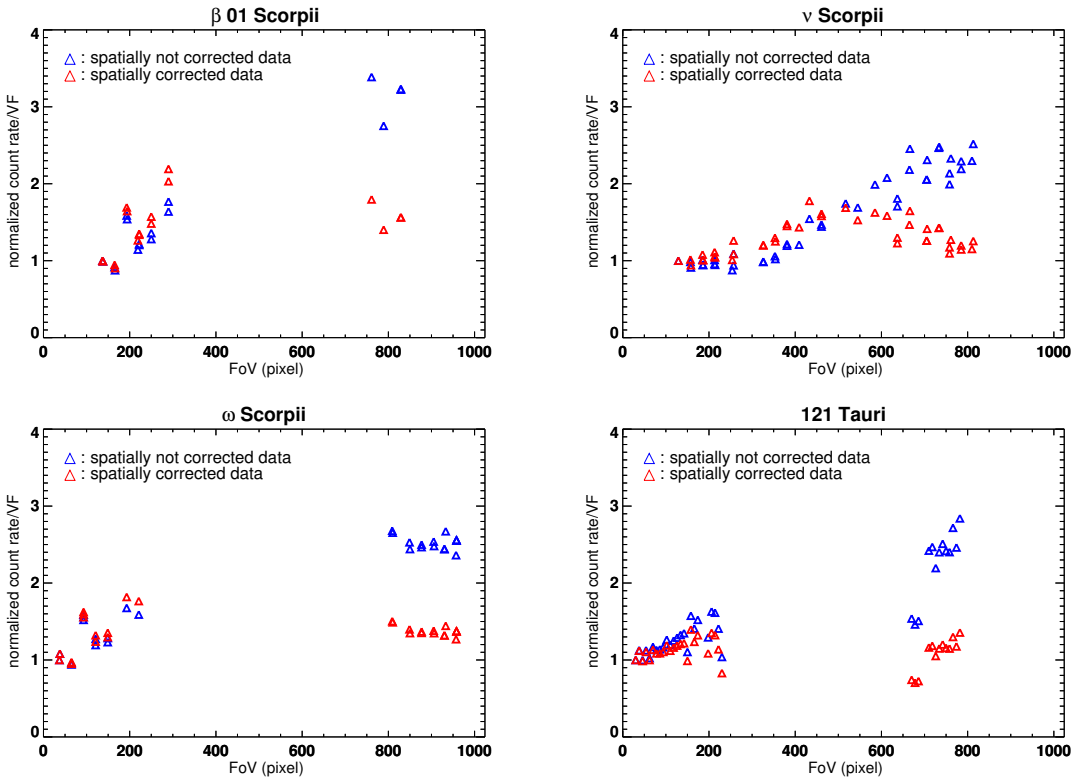

Figure 4.8: Comparison between the star count rate corrected with the standard VF (blue triangles) and the count rates corrected with the spatially corrected VF (red triangles). The four stars of the panels are β 01, ν, ω Scorpii, and 121 Tauri. See the text for details.

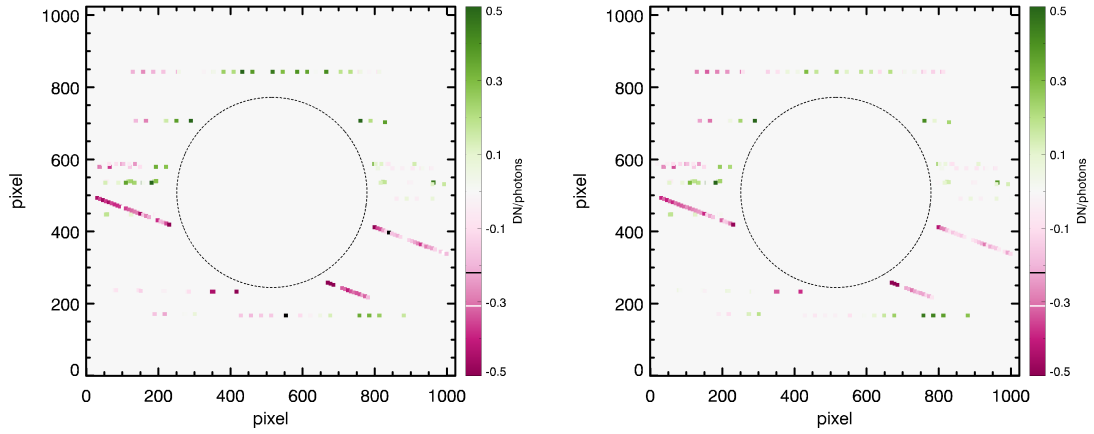

Figure 4.9: Left panel: map of the spatial distribution of the absolute differences between the radiometric calibration factors $\epsilon_{UV}(\mathrm{FoV})$ and the average radiometric calibration factor from the all the stars. Right panel: same map after the minimization of the differences. Images in detector (pixels) coordinates. See the text for details.

the linear correction can simply be expressed as:

$$z = z_1 + \frac{p \cdot (y - y_1)}{800} \tag{4.5}$$

with $z_1 = 1.0$ and $y_1 = 100$ (the normalized box is centered on this y-coordinate). Equation 4.5 depends on the p parameter, that represents the fractionary correction the plane applies to the stars count rates. Then I performed a χ^2 test on the differences (between the values across the FoV and the average value) to find the p parameter value which minimizes them. This value is $p = -0.24$, that means the count rates with y-coordinate equal to 900 pixels have to be decreased by a factor 0.76.

Figure 4.10 shows the χ^2 test results for the single stellar targets and for the entire data set (red squares) with respect to the p parameter. In the calculation of the global χ^2 test I excluded four targets (β 01 Scorpii, θ Ophiuchi, τ Tauri and 121 Tauri) whose data were affected by a large scatter from the beginning of the radiometric calibration procedure. Possible explanations of the data scatter are given in Section 4.3.

Thus, Equation 4.4 becomes:

$$\epsilon_{UV} = \frac{N_{UV}\,(\mathrm{FoV})}{f_* \cdot A_{pup} \cdot VF\,(\mathrm{FoV}) \cdot (M_{UV2VL}\,(\mathrm{FoV})/z)} \tag{4.6}$$

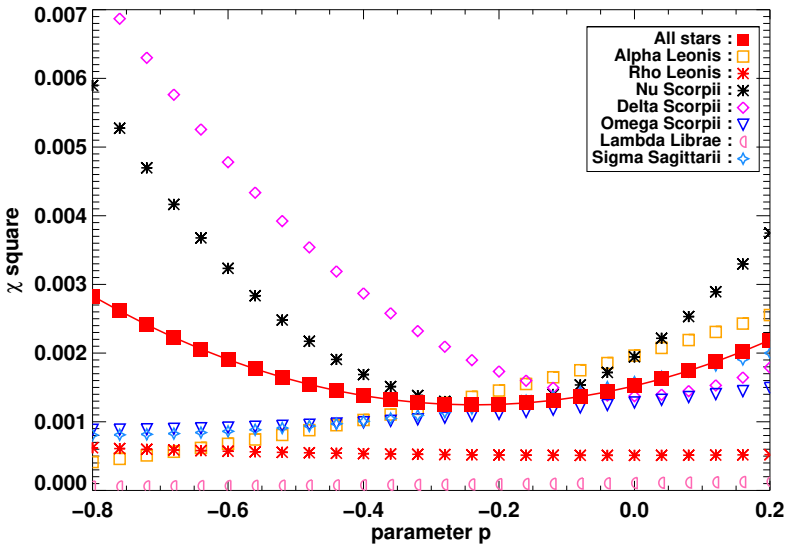

Figure 4.10: Values of the χ^2 test with respect to the p parameter for each star and for the entire data set (red squares). See the text for details.

where $M_{UV2VL}\,(\mathrm{FoV})$ is the spatial correction map described in Section 4.2.6 and z the linear correction defined by Equation 4.5. The right panel of Figure 4.9 shows the differences after the application of the linear correction.

Figure 4.11 shows the results after performing all the corrections and the inversion of the data set, which consists of eleven stars. For each target we calculated the values of the radiometric calibration factor related to the position across the FoV, as a function of the radial distance from the center of the internal occulter. The error bars are the standard deviations σ_* associated with the average value for each stellar target $\epsilon_{UV,*}$ (values reported in Table 4.1). The horizontal red solid line represents the $\overline{\epsilon}_{UV}$ value estimated as the average of the whole data set. This value with its standard deviation 1σ is 0.21 ± 0.03 DN/photon (see also Table 4.1).

Figure 4.12 shows the spatial correction map $M_{UV2VL}\,(\mathrm{FoV})$ divided by the linear correction z. With this additional linear correction, the spatial correction map $M_{UV2VL}\,(\mathrm{FoV})$ is now optimized by removing a residual systematic spatial trend observed in the calibration coefficients of the individual stars. The systematic trend is still remaining after multiplying simply the vignetting function by $M_{UV2VL}\,(\mathrm{FoV})$, thus the radiometric calibration here pro-

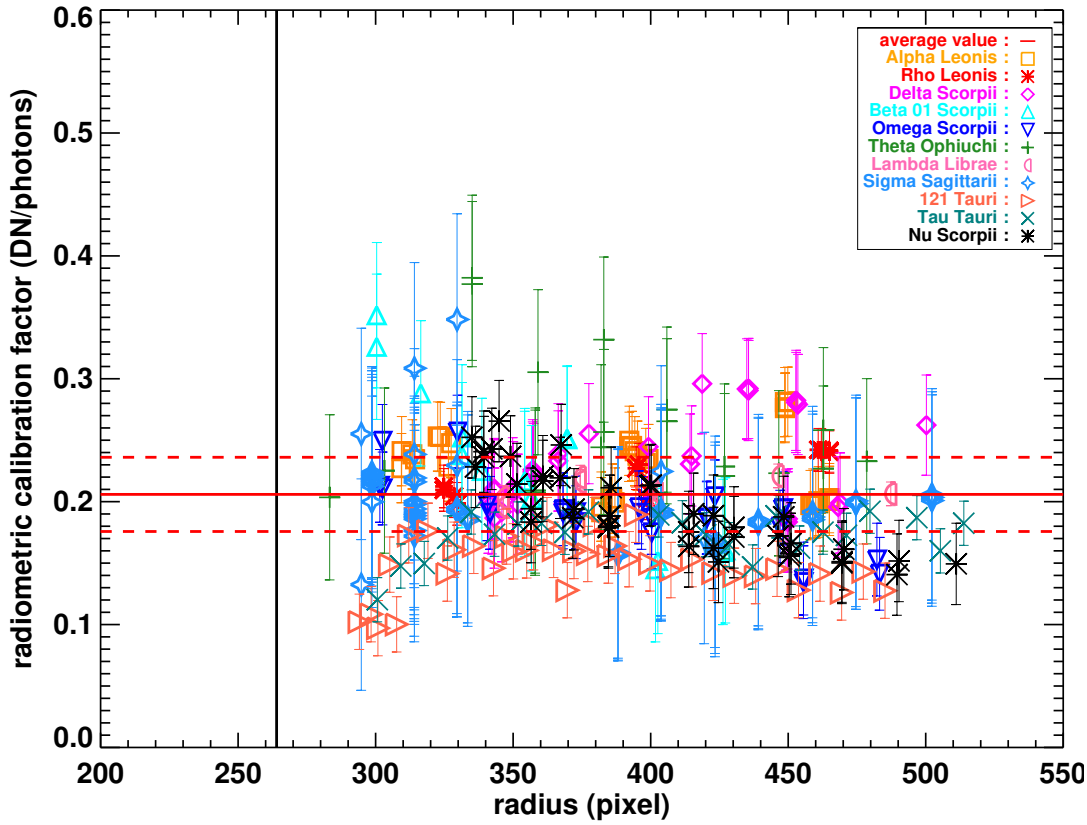

Figure 4.11: Radiometric calibration factors as a function of the radial distance of the star images from the center of the occulter. The solid red line is the average value of the radiometric calibration factor $\overline{\epsilon}_{UV}$. The red dashed lines depict the uncertainties of the in-flight radiometric factors. The vertical black solid line is the radius of the internal occulter in pixels.

vides the average radiometric calibration factor $\overline{\epsilon}_{UV}$ and the modified vignetting function $VF_{flight} = VF \cdot M_{UV2VL}\,(\mathrm{FoV})\,/\,\mathrm{z}$ to produce calibrated (L2) data.

Finally, I checked if there is any trend of the radiometric calibration factor with time. The analyzed data set belongs to a time range which spans through a year of the mission. For some targets I could use a double FoV transit, i.e. 121 Tauri with the first transit in January 2021 and the second one in August 2021, and θ Ophiuchi with the first transit in March 2021 and the second one in December 2021. Figure 4.13 shows the trend of the

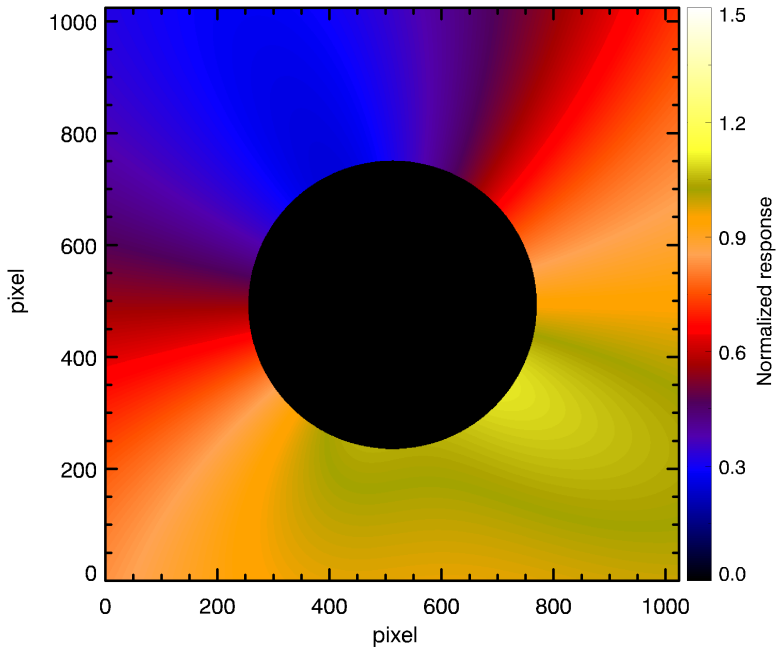

Figure 4.12: The spatial correction map $M_{UV2VL}\,(\mathrm{FoV})$ divided by the linear correction z. See the text for details. Image is in detector (pixels) coordinates.

average value $\epsilon_{UV,*}$ for every star with respect to time starting from June 2020 (the first month of the observations used for this work). The error bars are the standard deviations σ_* associated with the average value $\epsilon_{UV,*}$ for each stellar target. No changes of the average efficiency of the UV channel have been observed until August 2021.

4.3 UVDA anomalies

Since the beginning of the analysis of the star observations anomalies in the UVDA response were noticed. These made the in-flight radiometric calibration very challenging. The UV channel shows readout instabilities with non-linear variations both in the time and spatial domains.

The types of observed anomalies are different and in this section I summarize the ones which mostly affect the radiometric calibration frames. Other phenomenological descrip-

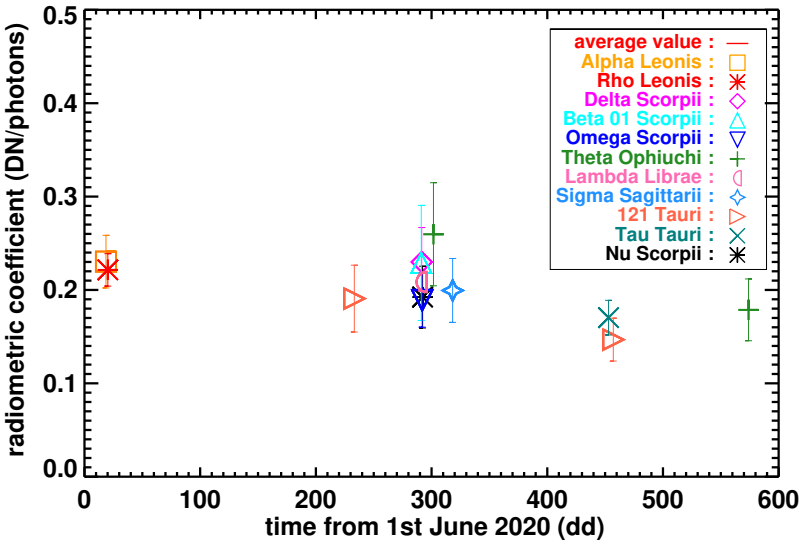

Figure 4.13: Trend of the radiometric calibration factor $\epsilon_{UV,*}$ with respect of time, starting from the month of the star observations used in this work. For every stellar target the reported radiometric calibration factor is the average value (see Table 4.1).

tions of the anomalies can be found in Andretta et al. 2021 and Russano et al. 2023. I already mentioned in Section 4.2.2 the problem related with the noticeable changes of the dark level from frame to frame at different time scales. As a consequence, calibration dark frames acquired with exactly the same detector parameters, do not always correct the UV frames. If appeared at short time scales, the effect is called "flickering". This anomaly does not affect significantly the radiometric calibration results, because with the performed aperture photometry I subtract the image background to the star signal and thus the single image dark contribution is canceled. On the other hand, other images of Metis (i.e. the ones used for the comparison with UVCS data, see Section 5.2) are affected by this problem, thus the implemented procedure of dark normalization described in Section 4.2.2 was necessary.

Metis team refers to another kind of anomaly as "flashes". Episodically until August 2021, UV images of different data set showed an unexpected and sudden increase of the frame brightness. Left panel of Figure 4.6 shows an example of this anomaly with the fourth and fifth values (magenta diamonds) of the count rate of β 01 Scorpii. These values are 50% larger than expected (black crosses), without any apparent explanation (i.e. changes in the

acquisition parameters, transient events, etc.). These episodes are very rare in the frames of the data set and thus I decide to discard them.

Starting from August 2021, significant brightness variations in the UV Metis frames were noticed also. These variations are not consistent with the static background corona at the time of those observations. The behaviour of the UVDA appeared to be bi-modal between two levels of brightness and affected entire data sets. Metis team refers to these two values as "low state" and "high state" of the detector response. Figure 4.14 shows the λ Librae signal and the coronal background around the star with respect of time. Mostly from the background trend it is possible to see the bi-modal behaviour of the UV channel response. The switch between the two levels was continuous and happened randomly.

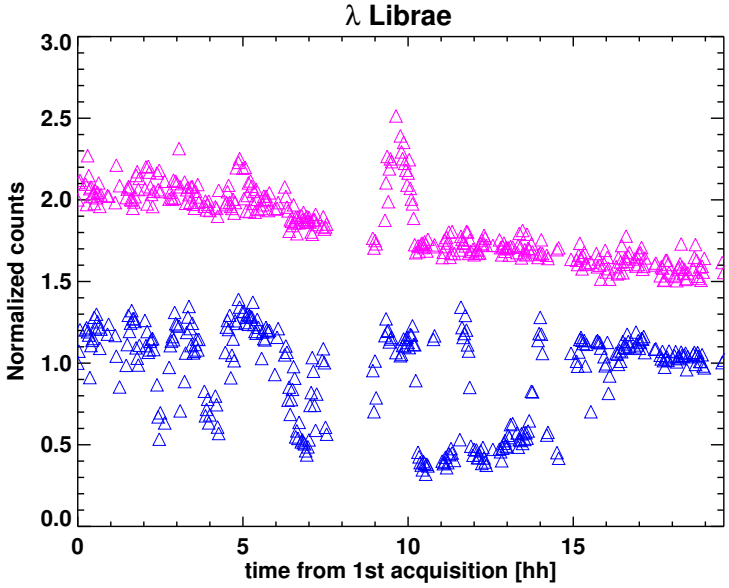

Figure 4.14: Star signal (magenta triangles) and coronal background (blue triangles) as a function of time for λ Librae. The star signal is shifted in the y-direction for the plot clarity. The first image of the series was acquired on November 19, 2021, at 09:14 UT.

Furthermore, sometimes "halos" surrounding bright objects (i.e. stars, planets and prominences) were noticed, when the detector was in a high state. The panels of Figure 4.15 show how the three states of the detector response affect the frames of ζ 04 and λ Librae, observed in November 2021.

The origin of the signal threshold variation is still under investigation, for this reason

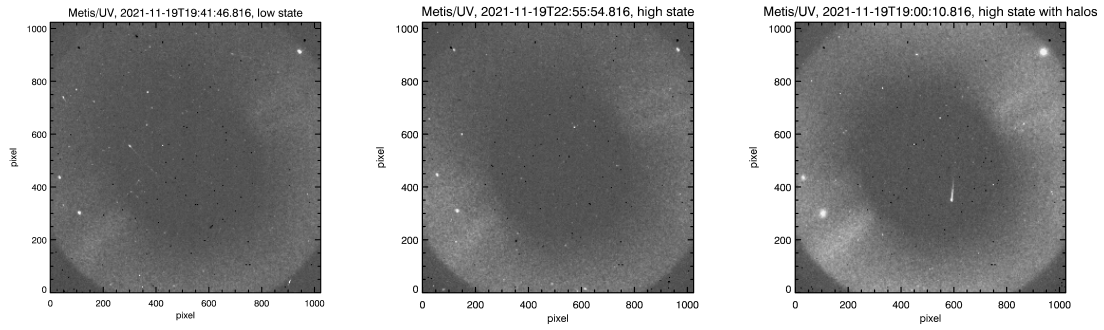

Figure 4.15: Three frames of the ζ 04 and λ Librae observation, happened in November 2021. ζ 04 Librae is the star on the top right of the detector, λ Librae is on the bottom left. The left panel depicts an example of "low state", the middle panel depicts the "high state" and the right panel a "high stat" with "halos" surrounding the stars.

the analysis was limited to stars transits until August 2021.

Chapter 5

First analyses of the calibrated data

After I performed the radiometric calibration of the two channels of Metis, it was possible for me to focus on qualitative and quantitative analysis of Metis data. In this chapter[1] I report such first analysis and the main results. In particular Section 5.1 and 5.2 refer to the comparison of the VL and UV Metis calibrated data with COR2 and UVCS data, respectively, while the topic of Section 5.3 is the observation of six eruptive events obtained by Metis in both channels during 2021.

5.1 Comparing coronal VL images of Metis and COR2

In this section I show the comparison between the total and polarized brightness VL images of the solar corona, obtained with Metis by applying the radiometric calibration described in Chapter 3, with those obtained with COR2. While a preliminary cross calibration of Metis VL channel with Mauna Loa Solar Observatory (MLSO) COronal Solar Magnetism Observatory (COSMO) K-coronagraph (K-cor; see, e.g., de Wijn et al. 2012) and LASCO/SOHO coronagraphs was carried out with the first light data (Fineschi et al. 2021), here I present a more detailed comparison that makes use of the VL data acquired during the superior conjunction of Solar Orbiter with STEREO-A on November 18-21, 2020. Dur-

[1] Section 5.1 is Sect. 3 (after a rewording) of the peer reviewed publication De Leo et al. 2023, paper A, submitted to *Astronomy&Astrophysics* and accepted.

Section 5.2 is Sect. 3 (after a rewording) of the peer reviewed publication De Leo et al. 2023, paper B, to be submitted to *Astronomy&Astrophysics*.

Section 5.3 is based on a journal article that is in preparation (Russano et al. 2023).

ing this period of time, the distance from the Sun and orientation of the plane of the sky (POS) of Metis and COR2 were similar (see Figure 5.1 and Table 5.1). The Metis *tB* and

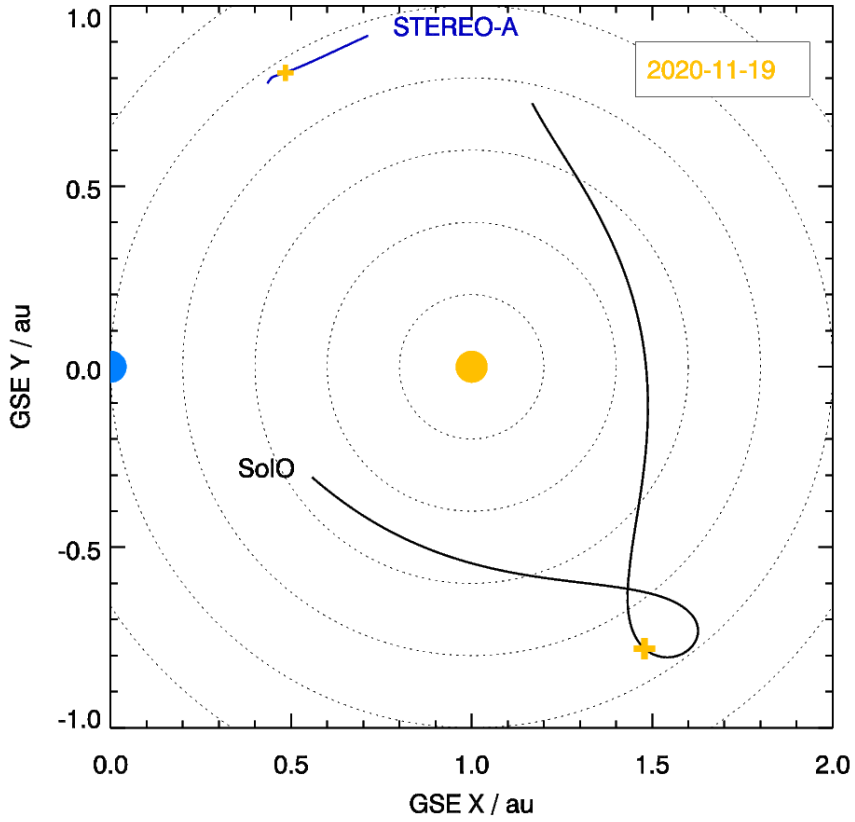

Figure 5.1: Position of Solar Orbiter and STEREO-A at the moment of the superior conjunction, in Geocentric Solar Ecliptic (GSE) coordinate system. The dots representing Earth (blue) and Sun (yellow) are not in scale. The yellow crosses indicate the position of the spacecraft on November 19, 2020.

pB images are level 2 images and were acquired using the polarized brightness acquisition mode (Antonucci et al. 2020) and then processed by means of the VL radiometric calibration procedure (see Chapter 3). The total and polarized brightness images of COR2 were obtained by performing the standard calibration procedure with the `SolarSoft`[2] package (Freeland & Handy 1998), routine `secchi_prep.pro`. This tool converts a raw signal of COR2 into mean solar brightness (MSB) units considering the band pass of its spectral filter (650-750 nm, Howard et al. 2008) and the photometric calibration factor, which

[2] `www.lmsal.com/solarsoft/`

Table 5.1: Superior conjunction of Metis with COR2.

Parameters of conjunction	
Date	Nov 18-21, 2020
d_{Metis}	0.92 au
d_{COR2}	0.95 au
$\lvert\Delta l_{\mathrm{POS}}\rvert$	$< 0.41^{\circ}$
$\lvert\Delta b_{\mathrm{POS}}\rvert$	$< 1.10^{\circ}$
FoV	5.55 - 11.5 $R_{\odot}$

Notes: d_{Metis} and d_{COR2} are the distances of the two instruments from the Sun in astronomical units (au). $\lvert\Delta l_{\mathrm{POS}}\rvert$ and $\lvert\Delta b_{\mathrm{POS}}\rvert$ are the absolute differences in longitude and latitude of plane of the sky (POS) of Metis and COR2, respectively. FoV represents the overlapping part of the fields of view of the two instruments.

was obtained observing numerous stars (for details, see STEREO/SECCHI Calibration and Measurement Algorithms Documents[3]).

The images were oriented in such a way that the northern pole of the Sun points to the top and the west solar equator to the right, in order to unify the format of the different images. The COR2 images were also flipped around the N-S axis passing through the Sun center, since this instrument was observing from the opposite side of the Sun during the superior conjunction with Metis in November 2020. All maps were then converted from Cartesian to polar (r, ϕ) coordinates, by determining a grid of polar coordinates with a step of the radial axis equal to 0.01 $R_{\odot}$ and that of the polar angle axis equal to 1°. The range of the r-axis is defined by the size of the overlapping part of the fields of view of Metis and COR2 (see Table 5.1). The polar angle ϕ is measured counterclockwise from the west solar equator. The intensity at each pixel of the polar coordinate grid was estimated by means of a B-spline interpolation of order 1 (Briand & Monasse 2018) of the surrounding pixels of the original image.

An example of the resulting total and polarized brightness images acquired quasi-simultaneously with Metis and COR2 is shown in Figure 5.2. These images are shown

[3] https://stereo-ssc.nascom.nasa.gov/publications/CMAD/secchi/

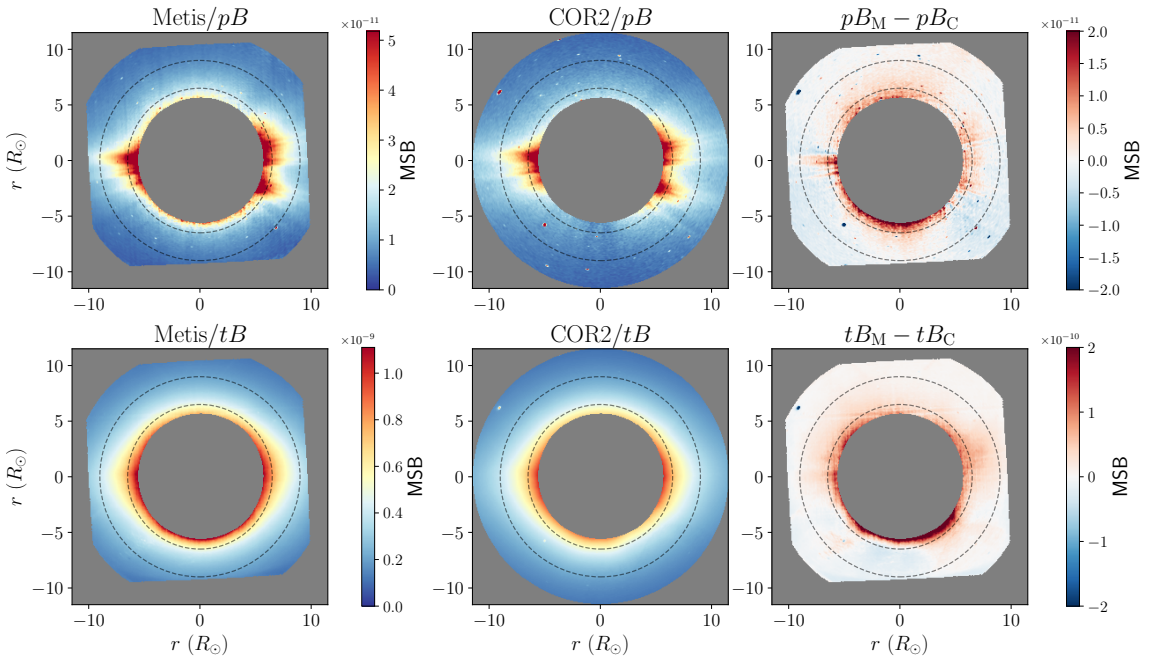

Figure 5.2: Polarized (pB) and total (tB) brightness images acquired on November 18, 2020 with Metis at 18:50:36 (left panels) and with COR2 at 18:53:15 (mid panels). The COR2 images are flipped around the N-S axis passing through the Sun center (see the text for details). Right panels represent the difference between Metis (pB_M and tB_M) and COR2 (pB_C and tB_C) images. The black dashed circles mark the heliocentric distances of 6.5 $R_\odot$ and 9 $R_\odot$, respectively. The color bar represents intensity in mean solar brightness (MSB) units. Horizontal and vertical axes correspond to the heliocentric distance in the $R_\odot$ units. Courtesy of A. Burtovoi.

in Cartesian coordinates for better visualization. The corresponding latitudinal profiles at the heliocentric distance of 6.5 $R_\odot$ and 9 $R_\odot$ can be found in Figure 5.3. In the latter figure the error bars of the pB and tB values are also shown. The relative uncertainties of the COR2 data were taken equal to ±20% as suggested in Frazin et al. (2012), whereas those of the Metis data were estimated propagating errors through the various steps of the calibration procedure mentioned in Section 3.1 and are about 12% for the used data set.

Although the band pass of COR2 differs from that of Metis, the comparison of the pB images of these instruments represented in the fraction of MSB has been carried out directly. At the considered heliocentric distances, the polarized emission is dominated by the K corona, which originates through the Thomson scattering of photospheric light by

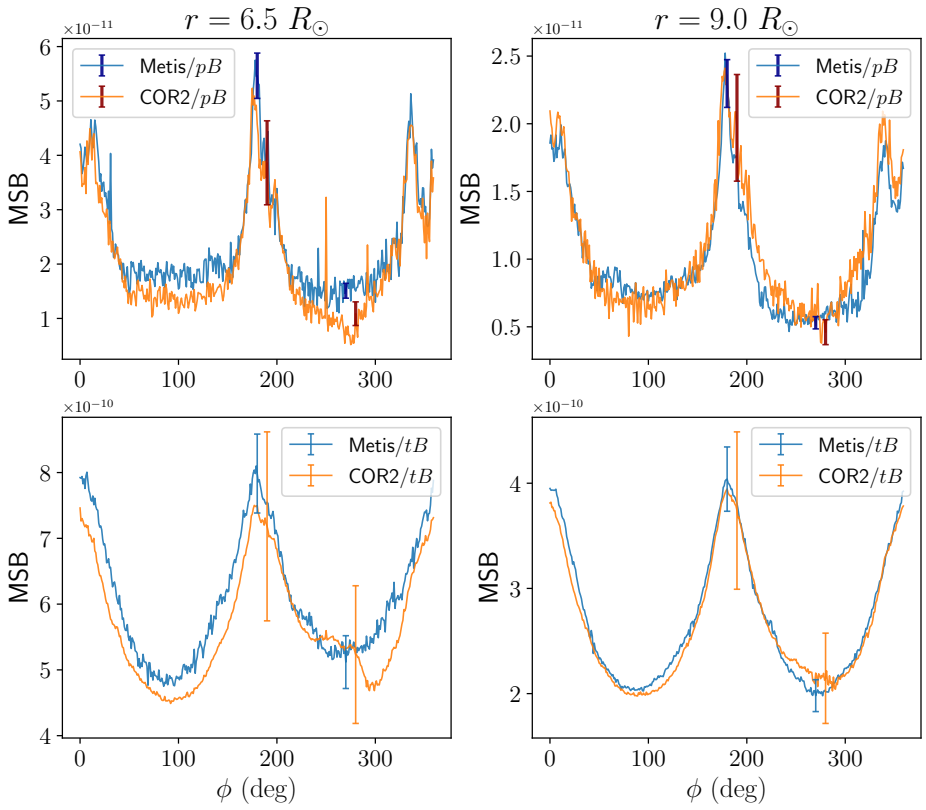

Figure 5.3: Latitudinal profiles of *pB* (top panels) and *tB* images (bottom panels) of Metis and COR2 shown in Figure 5.2 at the heliocentric distance of 6.5 $R_\odot$ (left panels) and 9 $R_\odot$ (right panels). The blue and orange lines show profiles of Metis and COR2, respectively. The error bars represent the uncertainties of the considered data (see the text for details). Courtesy of A. Burtovoi.

free electrons. Since the Thompson cross section does not depend on wavelength, the fraction of light (expressed in MSB) scattered within the band pass of Metis is the same as that of COR2. The polarized brightness images of Metis (pB_{M}) and COR2 (pB_{C}) are in a good agreement (see top panels of Figure 5.2). For example, the average difference of pB intensities at 6.5 $R_{\odot}$ (Figure 5.3, top left panel) is equal to $(3.3 \pm 3.6) \times 10^{-12}$ MSB. This estimate corresponds to the mean and the standard deviation of the distribution of $\Delta pB_{6.5R_{\odot}} = (pB_{\mathrm{M}} - pB_{\mathrm{C}})$ values. The relative difference, calculated as a ratio of $\Delta pB_{6.5R_{\odot}}$ and the amplitude of the pB_{M} profile, is equal to $7.0\% \pm 7.7\%$. At heliocentric distances of 9 $R_{\odot}$ (Figure 5.3, top right panel), $\Delta pB_{9R_{\odot}}$ is equal to $(-0.71 \pm 1.57) \times 10^{-12}$ MSB, which corresponds to lower relative difference: $-3.5\% \pm 7.7\%$. The increase of ΔpB at low altitudes can be explained by the presence of an additional component (e.g., stray light) close to the inner part of the Metis FoV. In any case, it should be noticed that these values of ΔpB are both consistent, given the estimated uncertainties, with no difference between Metis and COR2 measurements.

The direct comparison of the total brightness is less straightforward due to the presence of stray light in both instruments. In addition, tB images of Metis and COR2 most probably have a different contribution from the F corona within their band passes, which arises from the wavelength-dependent scattering of the photospheric emission on the dust grains (Boe et al. 2021). As can be seen from Figures 5.2 and 5.3 (bottom left panel), the Metis tB image is on average brighter than that of COR2 at low heliocentric distances ($\lesssim 8$ $R_{\odot}$). The COR2 image, in turn, clearly contains the stray light component at $\phi \approx 270°$. The absolute and relative differences of the total brightness profiles of Metis (tB_{M}) and COR2 (tB_{C}) at 6.5 $R_{\odot}$ are $(3.8 \pm 2.8) \times 10^{-11}$ MSB and $11.4\% \pm 8.3\%$, respectively. These features become less evident at higher heliocentric distances, where the contamination from stray light is expected to be lower. The latitudinal tB profiles of the two instruments are rather similar at heliocentric distances $\gtrsim 8$ $R_{\odot}$. The absolute and relative values of ΔtB calculated for the latitudinal profiles at 9 $R_{\odot}$ (Figure 5.3, bottom right panel) are equal to $(4.5 \pm 9.5) \times 10^{-12}$ MSB and $2.2\% \pm 4.6\%$, respectively.

Finally, the electron density profiles (n_{e}) were computed by applying the inversion technique of van de Hulst (1950) to the whole pB images of Metis (FoV: 5.55-11.5 $R_{\odot}$) and COR2 (FoV: 3.3-14.8 $R_{\odot}$). Two sets of n_{e} profiles extracted from the north-west sector ($0° \leq \phi \leq 90°$) of these quasi-simultaneous images are shown in Figure 5.4. The values

of electron density estimated for the equatorial regions ($\phi \leq 60^\circ$ in Figure 5.4) are consistent with each other. In addition, they rather smoothly connect with profiles presented in previous studies (e.g., Gibson et al. 1999; Saito et al. 1977). The polar n_e profiles of Metis ($70^\circ \leq \phi \leq 90^\circ$ in Figure 5.4) are systematically higher than those of COR2. This is most probably related to the presence of the above-mentioned additional component (e.g., stray light) in the Metis pB data close to the inner part of its FoV, which becomes significant in the polar region where the coronal emission is faint. In Dolei et al. 2018 a study of the parameter space shows that the solar wind speed is directly affected by changing the values of n_e by a factor of ±30%, thus it is important to characterize the additional component in the pB data and this work is left to forthcoming studies.

5.2 Comparing coronal UV images of Metis and UVCS data

The analysis presented here compares radial profiles of the H I Ly-α line intensity of Metis UV images, obtained by applying the UV radiometric calibration (see Chapter 4), with the profiles calculated using the archive data of UVCS. This comparison makes use of UVCS spectra and images of Metis, which were acquired during the periods of the activity minima of solar cycles 22 (in 1996) and 24 (in 2020-2021), respectively (see Figure 5.5).

5.2.1 Radial profiles of UVCS

As a characteristic period of the solar minimum of cycle 22, I considered a time interval of 6 months from April 1 to September 30, 1996. For this period all the available observations (all the heights) of the polar regions (±10° around the North and South poles) and of the equatorial regions (±10° around the East and West limb) were analysed. The spectral region in which the H I Ly-α was observed was selected and the spectrum fitted with a function that corrects instrumental effects (Giordano, Ph.D. thesis, 1999) in order to determine the total intensity from each observed spectra. Then, analyzing for the same time interval all the observations of C III 977 and Si III 1206.5 spectral lines, which come from the chromosphere and are not expected in the hot corona, the stray light contribution due to the disk emission not suppressed by the occulters was evaluated and removed. Finally,

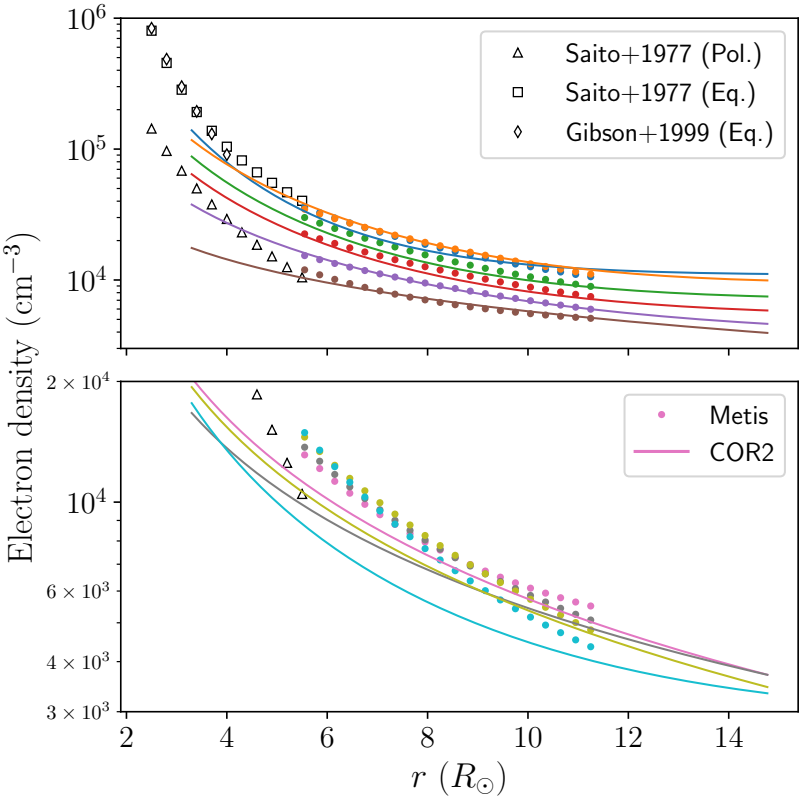

Figure 5.4: Radial electron density profiles calculated inverting *pB* images shown in Figure 5.2. The profiles of Metis and COR2 are depicted by means of the filled circles and solid lines, respectively. They are colored with the blue ($\phi = 0°$), orange ($\phi = 10°$), green ($\phi = 20°$), red ($\phi = 30°$), purple ($\phi = 40°$), brown ($\phi = 50°$) colors (top panel), pink ($\phi = 60°$), gray ($\phi = 70°$), olive ($\phi = 80°$) and cyan ($\phi = 90°$) colors (bottom panel). The COR2 profiles are calculated for the whole field of view of the instrument (3.3-14.8 $R_\odot$). The polar (Pol.) and equatorial (Eq.) electron density profiles reported in Saito et al. (1977) and that of the Eq. region reported in Gibson et al. (1999) are shown for comparison as black triangles, squares and diamonds, respectively. Courtesy of A. Burtovoi.

the H I Ly-α interplanetary (IP) contribution was also removed, which is estimated as $\sim 3 \times 10^7$ ph cm^{-2} s^{-1} sr^{-1} and is in agreement with values reported in previous studies (e.g., Kohl et al. 1997).

As mentioned above, the emission in the polar regions is quite stable for a given heliocentric height, while in the equatorial regions the modulation due to the passage of the active regions, that persist for more than one solar rotation, causes variations of almost an

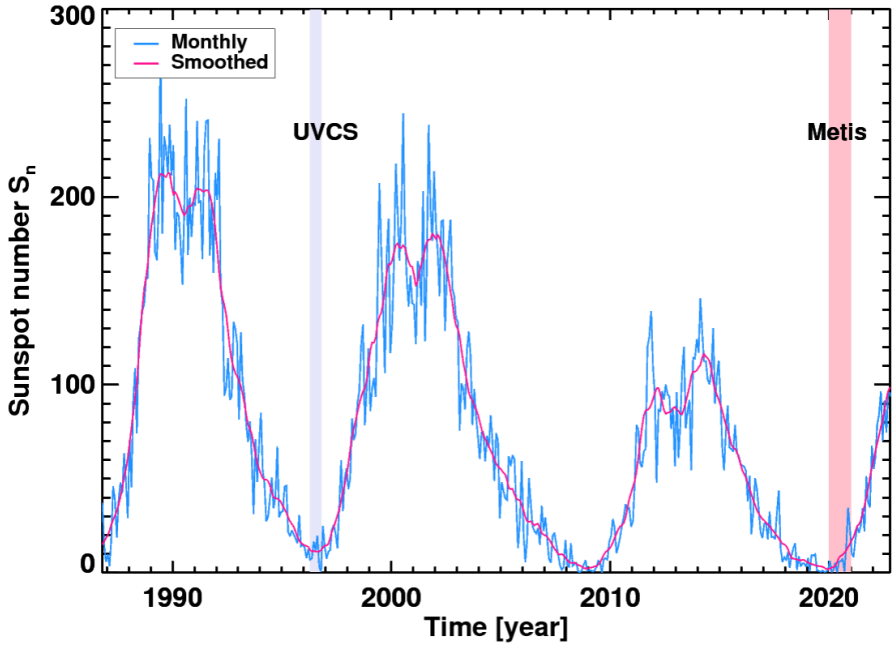

Figure 5.5: Sunspot number S_n with respect of time from cycle 22. The monthly mean total sunspot number and the 13-month smoothed total number are shown in light blue and fuchsia respectively. The lavender shaded area depicts the time interval of the UVCS observations used, while the pink shaded area indicates the Metis observations (see the text for details). Sunspot data from the World Data Center SILSO, Royal Observatory of Belgium, Brussels.

order of magnitude at some heights. Finally, by fitting the intensity as a function of distance with two different power-law functions, the equatorial and polar radial profiles were obtained (Giordano 2023). Figure 5.6 shows these profiles, that can be compared with those observed with Metis.

5.2.2 Average radial intensity profiles of Metis UV images

Radial profiles of Metis images were extracted from calibrated data (see Chapter 4) by means of the following procedure. All images were first oriented in such a way that the northern pole of the Sun points to the top and the west solar equator to the right. Then, all maps were converted from Cartesian to polar (r, ϕ) coordinates determining a grid of polar

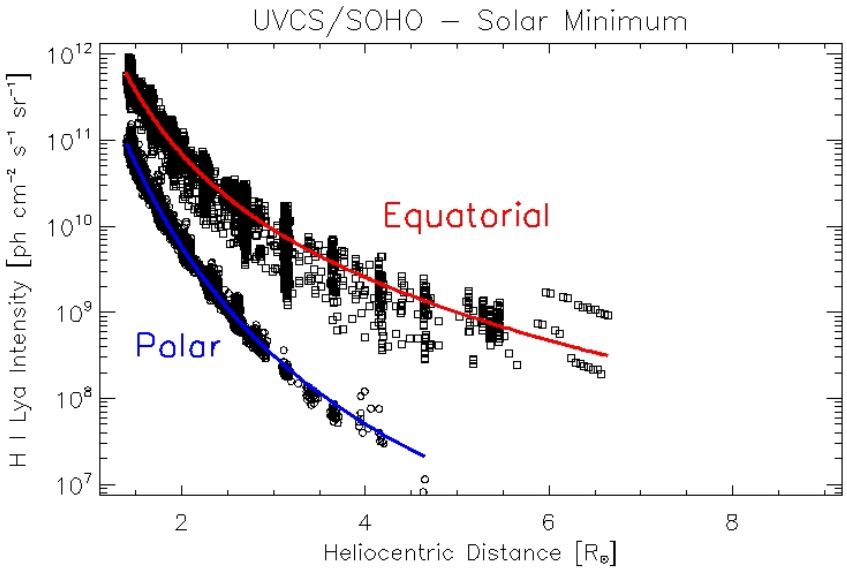

Figure 5.6: H I Ly-α intensity for the polar (blue solid line) and equatorial (red solid line) profiles obtained by fitting the UVCS data at solar minimum (displayed in black). Courtesy of S. Giordano.

coordinates. This grid had the polar angle axis with a step of 1° and the radial axis with a step which varied from one month to another due to the different distance of Metis to the Sun in the range from 0.02 to 0.09 $R_{\odot}$. H I Ly-α line intensity at each polar coordinate was estimated by means of a B-spline interpolation of order 1 (Briand & Monasse 2018) of the surrounding pixels of the original image. The mean radial profiles for each polar angle ϕ were computed using the data acquired with Metis during different months in 2020 and 2021 (see Table 5.2). Finally, it was possible to obtain equatorial and polar radial profiles of Metis by averaging those of the polar regions (±10° around the northern and southern poles) and those of the equatorial regions (±10° around the western and eastern solar equators).

The resulting equatorial and polar radial profiles of Metis are shown in the top panels of Figures 5.7 and 5.8, respectively. Bottom panels, in turn, present the difference between profiles of Metis and UVCS, which was averaged over the range of heliocentric distances. In addition, the width of a distribution of the Metis data at each altitude r as its standard deviation were estimated. The obtained values averaged as well over the range of heliocentric distances are depicted by means of error bars in Figures 5.7 and 5.8 (bottom panels).

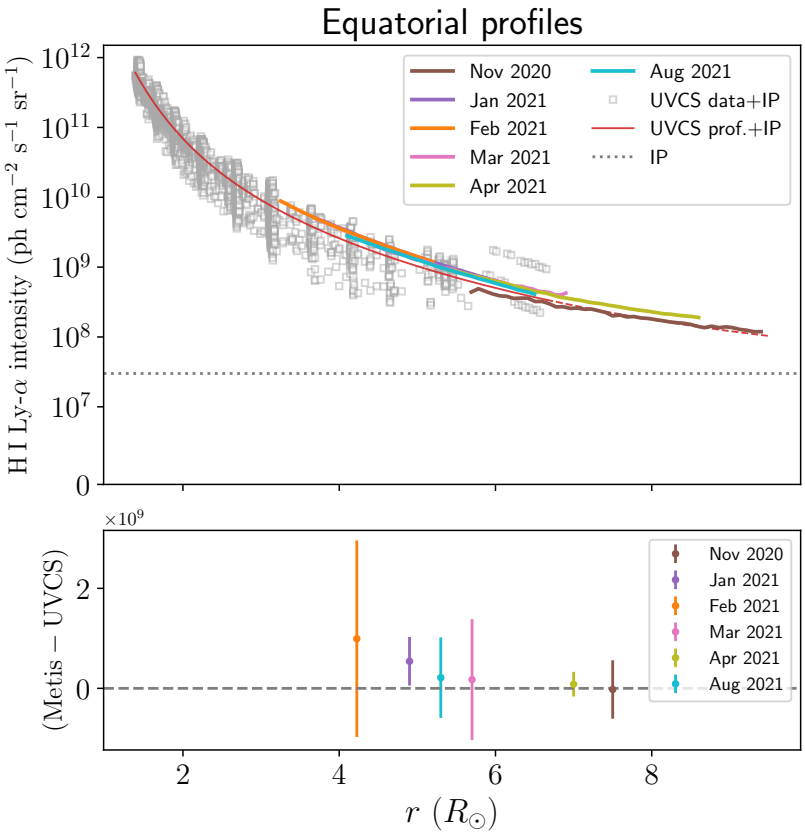

Figure 5.7: *Top panel*: equatorial radial profiles of the H I Ly-α line intensity. Average Metis profiles obtained for different months are shown as green (June 2020), brown (November 2020), purple (January 2021), orange (February 2021), pink (March 2021), olive (April 2021) and cyan (August 2021) lines. UVCS data and intensity profile obtained for equatorial observations and summed with the contribution of the interplanetary H I Ly-α line intensity are depicted as gray squares and red solid line, respectively. The dashed red line shows the extrapolation of the UVCS profile up to 9.5 $R_\odot$. *Bottom panel*: difference between the profiles of Metis and UVCS averaged over the range of heliocentric distances. The error bars represent the width of the distribution of Metis data averaged over the range of heliocentric distances as well (see the text for details). Courtesy of A. Burtovoi.

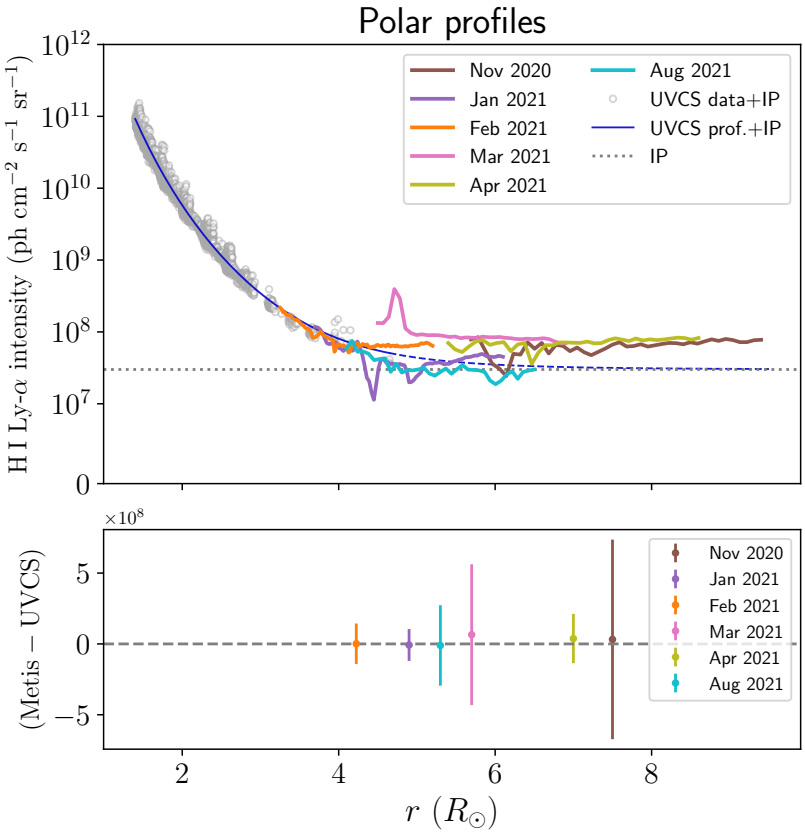

Figure 5.8: Same as Figure 5.7, but for polar radial profiles of Metis and UVCS. *Top panel*: UVCS data and intensity profile obtained for polar observations and summed with the contribution of the interplanetary H I Ly-α line intensity (IP, dotted line) are depicted as gray circles and blue solid line, respectively. The dashed blue line shows the extrapolation of the UVCS profile up to 9.5 $R_\odot$. Courtesy of A. Burtovoi.

Table 5.2: Metis UV data used for calculation of average radial profiles.

Date	$N_{\rm img}$	FoV [$R_\odot$]	$d_{\rm Metis}$ [au]
Nov 18-22, 2020	354	5.6 - 9.4	0.92
Jan 14-17, 2021	23	3.7 - 6.1	0.60
Feb 12-24, 2021	411	3.25 - 5.2	0.51
Mar 15-29, 2021	300	4.5 - 6.9	0.69
Apr 21-28, 2021	730	5.4 - 8.6	0.87
Aug 17-31, 2021	3350	4.1 - 6.5	0.64

Notes: The second column shows the number of images ($N_{\rm img}$) of the corresponding month reported in the first column, which were considered in the analysis. Field of view (FoV, in $R_\odot$) of Metis considered in the analysis and spacecraft distance to the Sun ($d_{\rm Metis}$, in astronomical units, au) are in the third and fourth columns, respectively.

Moving along the orbit, Metis performs observations being at different distances from the Sun. This allowed us to obtain and compare intensity profiles of the solar corona at various ranges of altitude: e.g., from 3.25 - 5.2 $R_\odot$ on February 2021 to 5.6 - 9.4 $R_\odot$ on November 2020. Even though the observations of UVCS have been carried out 25 years earlier than those of Metis, we can say that equatorial intensity profiles of the two instruments are quite similar at heliocentric distances $\leq$6.5 $R_\odot$. The difference of equatorial intensities of Metis and UVCS, which is typically lower than $\sim$ 10^9 photons cm^{-2} s^{-1} sr^{-1}, and the dispersion of the analysed data can be caused by the activity of the solar corona, eventual passages of bright stars and coronal mass ejections (CMEs). At higher altitudes, average Metis profiles are also in a good agreement with that of UVCS extrapolated up to 9.4 $R_\odot$.

During the solar minimum periods there is almost no activity in the polar regions and the UV emission from the corona is low. At high heliocentric distances (>6 $R_\odot$), the UV signal is expected to converge to the interplanetary H I Ly-α line intensity. In these regions, the Metis UV data is significantly affected by the instrumental noise. The polar profiles of Metis obtained for January, February and August 2021 are consistent with UVCS profile and its extrapolation above 4.65 $R_\odot$. The absolute difference of the corresponding intensities is typically lower than $\sim$ 10^7 photons cm^{-2} s^{-1} sr^{-1}. The intensity profiles calculated

for November 2020, March and April 2021, which covers coronal heights from 4.5 to 9.4 $R_\odot$, are a bit higher (by $\sim\ 4 \times 10^7$ photons cm^{-2} s^{-1} sr^{-1}) than that obtained from the UVCS observations. This can be related to the presence of instrumental effects of Metis (e.g., residual instrumental background or stray light) and/or UVCS. Alternatively, such a difference can be due to the presence of additional emission from the solar corona and/or a different level of IP emission observed during November 2020, March and April 2021 (see, e.g., Baliukin et al. 2019). Finally, I would like to note that the pink profile in Figure 5.8 has a peak at 4.7 $R_\odot$ due to the passage of bright stars (ν and δ Scorpii) on March 2021.

5.3 Six eruptive events seen by Metis

In Section 1.1 I already introduced CMEs as large scale and spectacular transient events due to the eruptions of mass and magnetic flux in the solar atmosphere. The largest heritage on the topic comes from VL coronagraphs, which measure the evolution of the plasma electron density and morphologic and kinematic properties from *pB* images. On the other hand, UVCS observations provided detailed information on CME plasma properties like temperature, inflow velocities and thermal energy content, by studying the UV spectral line emission (Giordano et al. 2013; Kohl et al. 2006).

As already remarked, often prominences are associated to CMEs, which are usually considered as erupting flux rope systems. The CME standard morphology is composed by three parts (see Figure 5.9): a bright front loop, an immediately following dark cavity and an embedded bright core (Illing & Hundhausen 1985). This bright core is often identified as an eruptive prominence. The prominences are composed of cool and dense material embedded in the hotter corona and are usually observed above the solar limb in Hα. Sometimes, part of their material escapes the solar gravitational field with a strong radial component of motion away from the solar surface. The remaining part falls back down.

However, it is difficult to prove the "bright core-prominence" association from the VL coronal observations alone and recently it was shown that the inner core of the three-part coronagraph CME in the most common cases is not a filament, which is rarely observed at large distances from the Sun, but a consequence of flux rope launch or part of the flux rope structure (Howard et al. 2017).

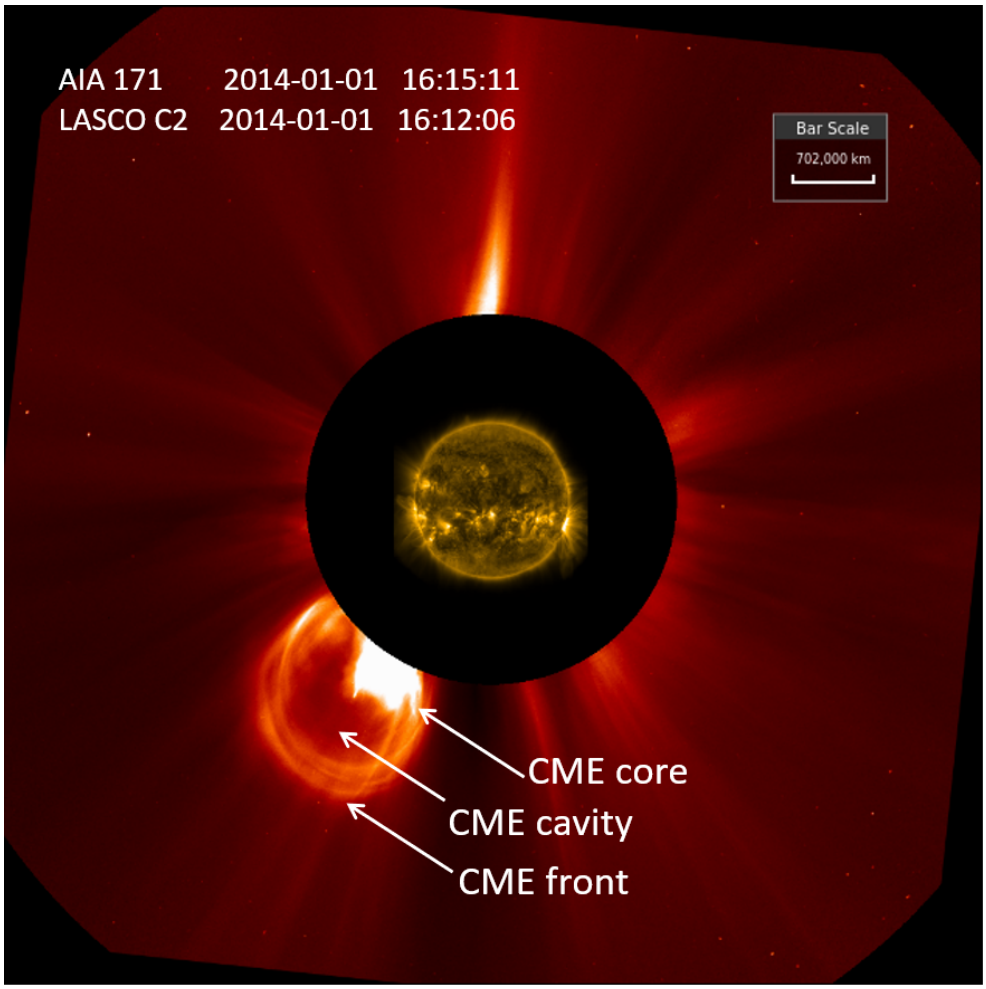

Figure 5.9: Typical three-part CME observed by SDO/AIA 171 and SOHO/LASCO-C2 on January 1, 2014, at around 16:12 UT. The CME structure is highlighted with white arrows which indicate respectively front, cavity and core. Image created with JHelioviewer (Müller et al. 2017).

Metis, by means of the simultaneous observation in the VL and UV band passes, permits for the first time a more comprehensive investigation of CMEs. In fact, it provides informations not only about the CMEs thermodynamic evolution during their propagation, but also about the solar corona (where they expand into) and its conditions like temperatures, densities and solar wind velocity (Romoli et al. 2021; Telloni et al. 2021). During the Cruise phase, Metis carried out long sequences of synoptic observations and detected several CMEs, some of which appeared to be related to compact features characterized by

strong H I Ly-α emission. I contributed to the study of six of such eruptive events and in this section I summarize the work presented in Russano et al. 2023. These events were observed on April 25$^{\text{th}}$, September 11$^{\text{th}}$, October 2$^{\text{nd}}$, October 25$^{\text{th}}$, and two events (North-West, and South-East) on October 28$^{\text{th}}$ (see Figure 5.10). These UV bright features could be identified as eruptive prominences.

The following sections are focused on the kinematics and intensity radial profiles of the six events.

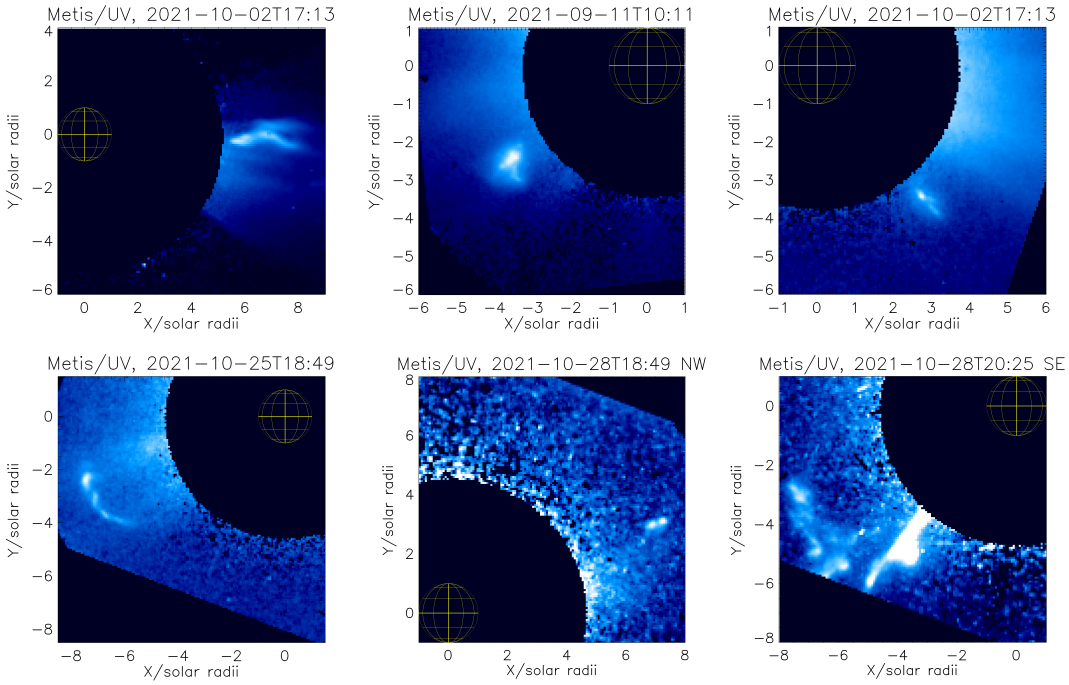

Figure 5.10: For each of the six events, one Metis UV frame where the eruption is visible is shown. The frames are rotated for the spacecraft roll and identified by the date in the title. The Sun disk is plotted in yellow.

5.3.1 Kinematics

All the six events discussed here were observed when Solar Orbiter was at distances greater than 0.5 au from the Sun. The associated CMEs were rather faint in some cases, by contrast all of them exhibited very bright UV structures, visible well beyond 5 $R_{\odot}$, in some cases up to 9 $R_{\odot}$ in the Metis UV frames. Thanks to the fact that the UV features appear

to be compact, it was possible to track their brightest parts through the instrument FOV and consequently to estimate their apparent velocity on the plane of the sky (POS). The acceleration was found by fitting the velocity with respect to the observing time.

The events and the associated CMEs were also observed with different space-based coronagraphs like LASCO-C2 and COR2, from different points of view along their orbits. For all the events, it was possible to observe features in the images of at least one of the other coronagraphs that could be identified as the VL counterparts of the UV features observed by Metis. This was fundamental for estimating the 3D position of the selected points in the eruptive features with the triangulation method provided by the routine called `scc_measure` available in the Solar Soft library (Thompson 2009). The routine estimates the Stonyhurst coordinates of a tie-pointed feature (Inhester 2006) selected manually on the two images from two different instruments, shown simultaneously in a visualization tool. By retrieving the Stonyhurst coordinated it was possible to determine the expansion direction for each event. By means of the 3D coordinates of the eruptive features the de-projection of the apparent velocities determined in the Metis images is performed, in order to obtain the radial velocity with respect to the Sun. Furthermore, the de-projected position vectors of the eruptive events show that in two cases the events remain bright beyond 15 $R_{\odot}$. Since the de-projection was not part of my contribution, the details of the methodology and of the data analysis are not reported here.

The expansion directions of the six events and the relative configurations of the spacecraft are shown in Fig. 5.11. Table 5.3 summarizes the main results from the kinematic analysis for each event.

The POS velocities ranges between 150 and 375 km/s, and they are comparable for the events of October 25$^{\text{th}}$ and April 25$^{\text{th}}$, as well as for October 2$^{\text{nd}}$ and 28$^{\text{th}}$-NW, while the fastest structure is that of October 28$^{\text{th}}$-SE (according to the de-projected speed).

Significant accelerations are evident only for the event of September 11$^{\text{th}}$ and for October 28$^{\text{th}}$-NW eruption, while for April 25$^{\text{th}}$ the residual acceleration contribution is very small and the October 28$^{\text{th}}$-SE eruption is decelerating. Schematically summarizing, CMEs can be classified according to their speed: slow CMES ($v \leq 250\,\mathrm{km/s}$), intermediate ($v < 250 \leq 450\,\mathrm{km/s}$) and fast CMEs ($v > 450\,\mathrm{km/s}$). Typically, slow CMEs show acceleration and most of the fast CMEs show deceleration due to their interaction with the solar wind. Both the de-projected speed (not reported here) and acceleration values in

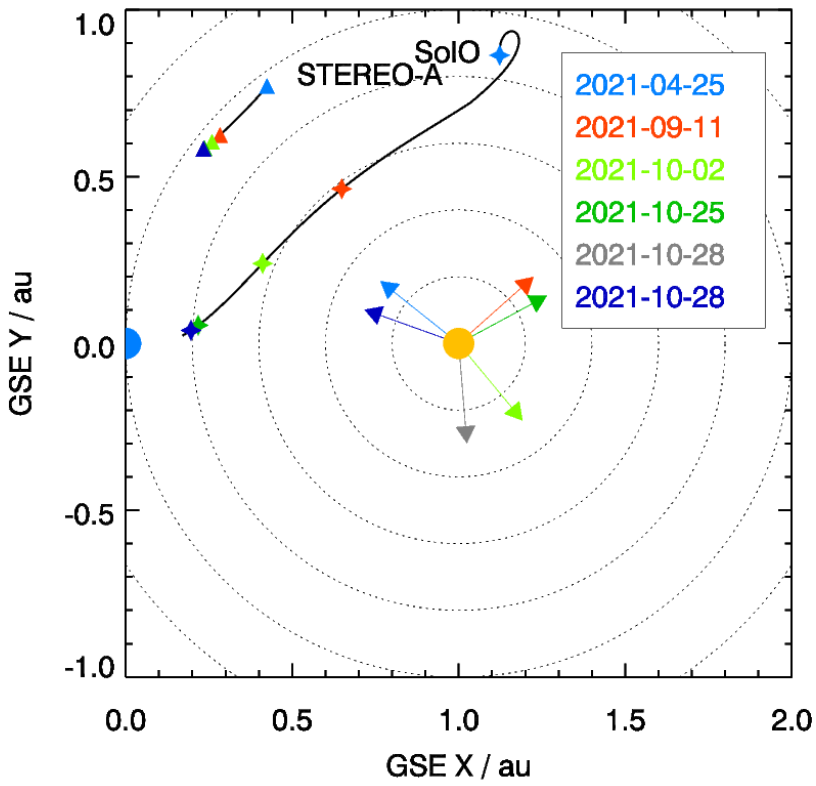

Figure 5.11: Position of Solar Orbiter, STEREO-A, and near-Earth facilities (SOHO) for all the events considered in this section, in GSE coordinate system. The dots representing Earth (blue) and Sun (yellow) are not in scale. The arrows show the estimated directions of the eruption as determined by triangulation (see the text for more details). The color code used for each event is: April 25th event in light blue, September 11th in orange, October 2nd in light green, October 25th in green, October 28th (north-west) in grey, and October 28th (south-east) in blue.

Table 5.3 are compatible with the statistics of CME observations in Yashiro et al. 2004 at solar minimum phase.

5.3.2 Intensity radial profiles

As I already described in Section 2.1.1, the emissivity profiles from the Metis *pB* and UV images can be used as a diagnostic to retrieve information about the physical conditions of the emitting plasma (e.g. density, temperature, outflow velocity).

Table 5.3: Measured parameters for all events.

Event date	Event range [UT]		POS velocity	Residual acceleration	Direction Carr. coord. [deg]	
	pB	UV	[km/s]	[m/s^2]	Lon.	Lat.
25 - 26 Apr. 2021	16:20 - 18:20 on 25/04	22:44 on 25/04 4:44 on 26/04	152 ± 6	1.7 ± 0.4	179.5 ±0.3	-6 ± 1
11 Sep. 2021	07:27 - 07:41	10:05 - 11:17	375 ± 5	7 ± 1	44.1 ± 0.6	-34 ± 1
2 Oct. 2021	14:19 - 15:19	17:05 - 19:49	228 ± 13	compatible with zero	30 ± 1	-28 ± 1
25 Oct. 2021	11:49 - 12:49	14:00 - 16:00 18:00 - 20:00	150 ± 1	0.7 ± 0.1	169.6 ± 0.5	-11 ± 1
28 Oct. 2021 North-West	15:49 - 20:49	18:07 - 19:11	244 ± 10	15 ± 3	15.6 ± 0.5	22.9 ± 0.8
28 Oct. 2021 South-East	19:19 - 20:49	18:05 - 22:57	184 ± 1	-8.5 ± 0.1	258.5 ± 0.4	-8.3 ± 0.6

Notes: the table reports the measured parameters for all events such as the time range selected for analysis, apparent POS velocity, deprojected residual acceleration, and Carrington coordinates of the eruption directions estimated by the triangulation method as explained in the text. Data from Russano et al. 2023.

For each UV frame, first a procedure to remove the coronal background was developed: by considering boxes of about 70×70 pixels centered around the bright structure and selecting only the pixels outside the visible feature, a fit to a surface is performed to estimate the background contribution. Then, the result is subtracted from the original box. After this background removal, only the pixels of the structure with an intensity greater than the background plus 10 % are selected. With this method it is possible to obtain the average UV intensity of selected pixels and their area, frame by frame. The Metis UV H I Ly-α emission profiles of the eruptions are shown in Figure 5.12, with a comparison with the line intensity distribution of the CMEs reported in the UVCS catalog as in Figure 15 of Giordano et al. 2013. The typical intensities in streamers at solar minimum and maximum and in a coronal hole are also shown for comparison. The general trend of the studied eruptions is comparable to the streamers in the range of solar distance above $4R_{\odot}$, except for the event on October 2nd, which shows a completely different trend (and whose interpretation is still under investigation).

Furthermore, the contribution of the interplanetary Ly-α (of $\sim 10^7$ photons cm^{-2} s^{-1}

sr^{-1}) is well below the measured profiles in the considered range of heliocentric distance.

Since the intensity of the resonant component of the UV H I Ly-α emission is also sensitive to the speed of the coronal plasma, a constant but non-negligible component of Doppler dimming effect is taken into account in the analysis of each eruption. The Doppler dimming coefficients are estimated as specific intensity ratios (see Eq. (2) in Dolei et al. 2018), considering a uniform chromospheric intensity profile with an analytical shape defined in Auchère 2005. By using the assumption of hydrostatic equilibrium, the Doppler dimming coefficients depend only on the electron temperature and the radial velocity of the eruption. In our calculations, the electron temperature profiles defined in Vásquez et al. 2003 and Gibson et al. 1999 were used, extrapolated to the heliocentric position of the events, properly converted to radial distances. For all the events, the resonantly scattered component is dimmed by more than 70%, due to the high velocity of the structures and the rapid decrease of the coronal temperature with height (1 MK at 5 $R_\odot$ and 0.2 MK at 20 $R_\odot$). The results will be presented in Russano et al. 2023 (in preparation).

The VL emission of the prominences is evaluated in a different way. It is important to remark that the VL counter part of the UV bright structures is faint for the majority of the events under study. Thus, for each available *pB* base difference, only the peak brightness of the luminosity profile of the recognizable feature along the polar angle corresponding to the feature in UV frames is selected. To account for the coronal background, from each profile the fifth percentile is subtracted. Due to the rather long exposures chosen for the Metis VL channel acquisition, a *smearing* effect affects the *pB* frames, making impossible the evaluation of the areas of the erupted prominences, as done for the UV frames. Figure 5.13 reports the *pB* peak intensity of the eruptions at different heliocentric heights.

From Figures 5.12 and 5.13 it is possible to notice that the structures under study present a progressive decrease in the UV and pB intensity profiles, respectively, due to the decrease in the emission of the outward expanding coronal plasma.

In Russano et al. 2023 a detailed description of the kinematics and of the intensity radial profiles can be found for all events. In that work, for each event, an accurate analysis of the UV intensity is carried out in order to compare it with the *pB* intensity and to evaluate the radiative and collisional components of the H I Ly-α emission. In a couple of events the collisional excitation component appears to be non-negligible and can be related to a cold dense plasma strongly emitting in H I Ly-α, dominating over the radiative component.

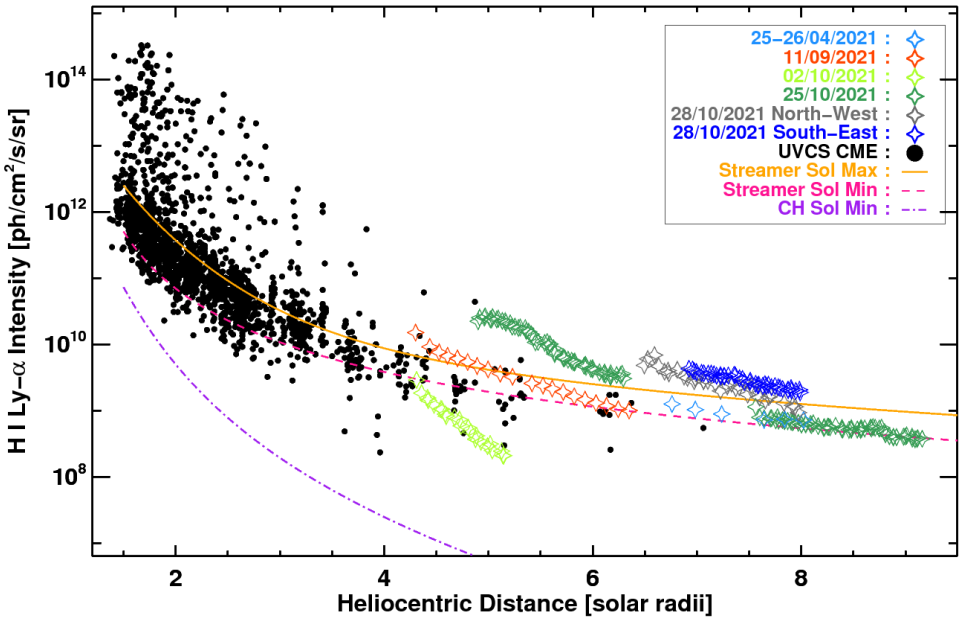

Figure 5.12: UV H I Ly-α mean intensity of the eruptions (colored star points) compared with the UVCS CMEs intensity (black points) taken from Fig. 15 (a) of Giordano et al. 2013 as a function of heliocentric heights. For comparison, the typical intensities of streamers at solar minimum and maximum and of a coronal hole are reported (colored lines). See the text for details.

This indicates how collisional emission processes cannot be considered negligible in the formation of the H I Ly-α emission in bright coronal features, even at large heliocentric distances. However, this final analysis is beyond the scope of this thesis and it is not reported here in further detail.

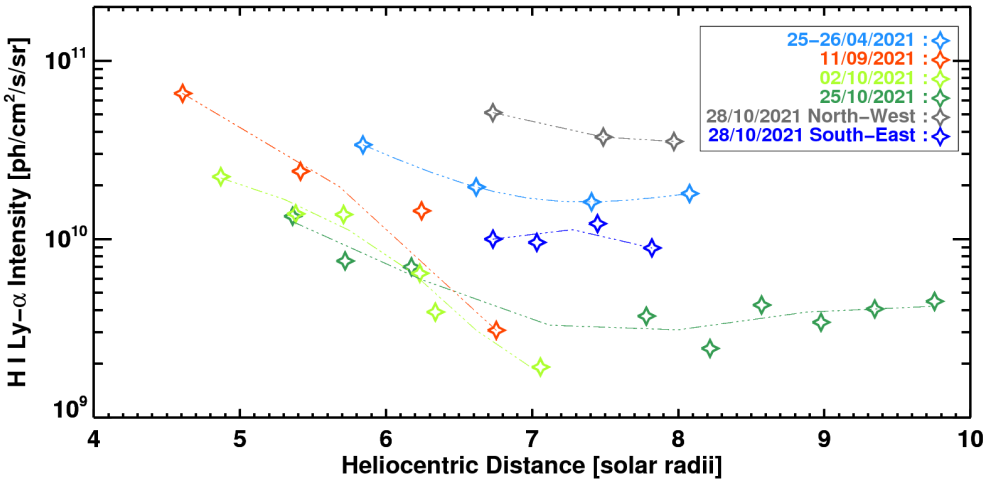

Figure 5.13: Polarized brightness peak intensity of the eruptions (colored star points) as a function of heliocentric heights. See the text for details.

Chapter 6

Conclusions

6.1 Conclusions[1]

Close-up observations of the solar corona provide a new perspective of its longitudinal structure and evolution, especially if they are performed out of the ecliptic.
In the last three solar cycles the space-based coronagraphs largely enhanced our capability to study the solar atmosphere. VL coronagraphs (from LASCO and SECCHI suites) have extended the spatial coverage of coronal imaging out to 30 solar radii, with resolution able to detect faint coronal structures and weak CMEs. In addition, UVCS opened the access to the domain of UV spectroscopy of the outer corona, permitting complete diagnostics of the physical properties and dynamics of the solar atmosphere plasma (see Chapter 1).

Metis, the coronagraph aboard Solar Orbiter, fits in this context. It has the aim of extending the knowledge acquired with UVCS, by performing, for the first time, simultaneous imaging of the off-limb solar corona from 1.7 $R_\odot$ to 9 $R_\odot$ in both VL and UV light, with unprecedented temporal coverage and spatial resolution.
By exploiting the mission profile of Solar Orbiter, Metis performs measurements from different latitudes and permits complete characterization of the parameters and the dynamics of the main plasma components (electrons and neutral hydrogen atoms/protons) in the cru-

[1] This chapter is based on Sect. 4 in the article De Leo et al. 2023, paper A and Sect. 4 in the article De Leo et al. 2023, paper B, respectively accepted and to be submitted to *Astronomy&Astrophysics* for publication. It also summarizes the results reported in the conclusive section of the journal article Russano et al. 2023, which is in preparation.

cial region where the solar wind is accelerated and CMEs are generated and start their propagation. Furthermore, the perihelia observations, when the Sun surface rotational velocity relative to the spacecraft is lower, allow long-term studies of off-limb features and the disentangling of their evolution from solar rotation effects.
The innovative near-Sun multi-band imaging of Metis improves relevantly our understanding of the region connecting the Sun to the heliosphere, addressing the fundamental issues of solar physics such as the heating/acceleration of the fast and slow solar wind components, the origin and the evolution of transients events (CMEs, eruptive prominences) and of SEPs events (see Chapter 2). Furthermore, the synergy with other missions and ground based observatory, including plasma instruments, like those on Solar Orbiter and PSP, provides for the first time a multi-spacecraft and multi-point-of-view perspective to the Sun investigation.

Metis science composes the framework of this thesis, devoted to the development of tools for the data analysis of the coronagraph aboard Solar Orbiter. As already remarked, the in-flight radiometric calibration is a crucial passage in the data processing to obtain the absolute brightness of the solar corona from the imaging performed by Metis. Chapter 3 and Chapter 4 refer to the radiometric calibration I performed for the VL and UV channel, respectively.

The VL radiometric calibration factor ϵ_{VL} was obtained by using planned stars observations in a time period from June 2020 until March 2021. The value of the coefficient is equal to 0.014 ± 0.001 DN/photon across the full field of view, and it is consistent within the uncertainties with the value of 0.014 ± 0.003 DN/photon from the on-ground calibration campaign. Currently, the factor ϵ_{VL} is used in the official pipeline of Metis which produces calibrated (L2) data.

As the results from all stellar targets are consistent within uncertainties with each other and with the ground calibration, no degradation of the channel response has been observed (until March 2021).

The values from the data set present an unexpected trend near the occulter (see Figure 3.7), one possible explanation is an under-correction of the stars signal in the zone of the images close by the occulter, where our knowledge of the VF is poor (e.g, possibly due to the presence of stray light near the occulter during the on-ground calibration measure-

ments). Nevertheless, the star transits across the FoV served also as an in-flight calibrations of the VF (Figure 3.5 left panel).

In turn, in order to obtain the radiometric calibration factor ϵ_{UV}, I made use of stars observations in a time period from June 2020 until August 2021. After the UV vignetting function (derived from the VL one on theoretical bases) correction, it was still necessary to perform additional corrections to account for a strong disuniformity in the spatial response across the FoV: one spatial correction $M_{UV2VL}\,(\mathrm{FoV})$, obtained as the UV-to-VL ratio of the back-illuminated door frames, and a linear correction z, that optimizes such spatial correction by removing a residual systematic spatial trend observed in the calibration coefficients from the individual stars still remaining after multiplying VF by $M_{UV2VL}\,(\mathrm{FoV})$ (see Section 4.2.6 and Section 4.2.7).

The value of the average radiometric calibration factor $\bar{\epsilon}_{UV}$ is equal to 0.21 ± 0.03 DN/photon. As for the VL channel, the radiometric calibration (average calibration factor and modified $VF_{flight} = VF \cdot M_{UV2VL}\,(\mathrm{FoV})\,/\mathrm{z}$ composes part of the official pipeline of Metis. I also checked the trend with time of $\epsilon_{UV,*}$, by exploiting repeated FoV transits of some stellar targets, and conclude that no degradation of the channel response has been observed (until August 2021).

The UVDA anomalies made the characterization of the UV channel response challenging at the beginning (see Section 4.3). However, currently most of the problems have been solved or strongly mitigated and the radiometric calibration presented here contributed to this.

The radiometric calibration I performed for the Metis channels lays the groundwork for the future improvement and the continuous monitoring of the instrument response, which is necessary for the correct quantitative use of the acquired data.

After I performed the VL and UV radiometric calibration and the calibrated data were produced, I had the possibility to contribute to first scientific applications of those. In Chapter 5, I describe the comparison of the Metis calibrated data with other space-based coronagraphs (Section 5.1 and Section 5.2). Furthermore, I report about the study of six eruptive events with exceptionally bright emission in H I Ly-α observed by Metis during 2021 (Section 5.3).

For the VL channel, the comparison is carried out by using images acquired with Metis and COR2 during the conjunction with Solar Orbiter. The values of the total and polarized brightness of the solar corona measured with these two instruments are found to be in a reasonable agreement with each other, even without accounting for the instrumental background (stray light) and likely different contribution of the F corona to the tB images. In addition, the electron density profiles calculated inverting the pB images of Metis and COR2 are consistent with each other and also with those reported in the literature.

The comparison of the average radial profiles of the H I Ly-α line intensity observed with UVCS and Metis makes use of data acquired during the periods of the activity minima of solar cycles 22 and 24, respectively. Although the analysis presented does not account for systematic effects of solar origin (e.g. possible variability of the UV intensity from one solar cycle to another), it is found that the resulting radial profiles are similar. The obtained agreement between the two instruments suggests that the contribution from the stray light and various anomalies (see Section 4.3) to the UV data of Metis was, on average, quite moderate during the observations carried out from June 2020 to August 2021. However, the 25-yr gap between the datasets of UVCS and Metis prevents us from deriving quantitative conclusions.

For the study about the eruptive events, the selected set of observations includes all the events observed by Metis during the Solar Orbiter Cruise phase, i.e. until the end of 2021, that are characterized by remarkably bright emission in H I Ly-α. The observed features remained bright even at heliocentric distances as large as 15 $R_{\odot}$.

By using a triangulation method (Inhester 2006), it was possible to determine the kinematics of the observed structures, obtaining measures of the POS velocity and propagation direction, as well as estimates of the acceleration.

In summary, the results show that only four events out of six present a clear CME three-part structure and in Metis pB frames three events are really faint, while appear clear in LASCO-C2 or COR2 frames. In three cases, the bright UV eruption appears to be the bright core of the expanding CME.

The trend of the H I Ly-α emission as a function of distance (time) from the solar limb is comparable to that of streamers at solar distance above 4 $R_{\odot}$, except for one event (October 2nd). Generally, the structures under study present a progressive decrease in the UV and pB intensity profiles, due to the decrease in the emission of the outward expanding

coronal plasma. The analysis to evaluate the radiative and collisional components of the H I Ly-α emission, described in Russano et al. 2023, shows clearly that in some cases the collisional excitation component appears to be non-negligible or even dominant over the radiative component. This indicates how collisional emission processes have to be taken into account in the formation of the H I Ly-α emission in bright coronal features, even at large heliocentric distances.

By developing appropriate models, it is possible to explore further the physical characteristics of the events described in Section 5.3. For example, several plasma diagnostic techniques can be used to extrapolate the parameters of the plasma embedded in CMEs, as it is described in Bemporad et al. 2018, in which estimation of the CME plasma electron density and temperature is performed by means of a numerical simulation, taking into account Doppler dimming effect when analyzing coronagraphic UV and VL observations.

Bibliography

Andretta, V., Bemporad, A., De Leo, Y., et al. 2021, A&A, 656, L14

Antonucci, E., Romoli, M., Andretta, V., et al. 2020, A&A, 642, A10

Auchère, F. 2005, ApJ, 622, 737

Auchère, F., Andretta, V., Antonucci, E., et al. 2020, A&A, 642, A6

Baldwin, K. & Vourlidas, A. 2008, in AGU Fall Meeting Abstracts, Vol. 2008, SH13B–1532

Baliukin, I. I., Bertaux, J. L., Quémerais, E., Izmodenov, V. V., & Schmidt, W. 2019, Journal of Geophysical Research (Space Physics), 124, 861

Bemporad, A., Pagano, P., & Giordano, S. 2018, A&A, 619, A25

Benz, A. O. 2017, Living Reviews in Solar Physics, 14, 2

Bertaux, J.-L., Korablev, O., Perrier, S., et al. 2006, Journal of Geophysical Research (Planets), 111, E10S90

Bessell, M. S., Castelli, F., & Plez, B. 1998, A&A, 333, 231

Blackwell, D. E. & Petford, A. D. 1966, MNRAS, 131, 399

Boe, B., Habbal, S., Downs, C., & Druckmüller, M. 2021, ApJ, 912, 44

Briand, T. & Monasse, P. 2018, Image Processing On Line, 8, 99, https://doi.org/10.5201/ipol.2018.221

Brueckner, G. E., Howard, R. A., Koomen, M. J., et al. 1995, Sol. Phys., 162, 357

Burlaga, L. F., Ness, N. F., Berdichevsky, D. B., et al. 2019, Nature Astronomy, 3, 1007

Capobianco, G., Casti, M., Fineschi, S., et al. 2018, in Society of Photo-Optical Instrumentation Engineers (SPIE) Conference Series, Vol. 10698, Space Telescopes and Instrumentation 2018: Optical, Infrared, and Millimeter Wave, ed. M. Lystrup, H. A. MacEwen, G. G. Fazio, N. Batalha, N. Siegler, & E. C. Tong, 1069830

Carroll, B. W. & Ostlie, D. A. 2007, *An Introduction to Modern Astrophysics* (2nd Edition), Pearson Addison-Wesley. San Francisco.

Casti, M., Fineschi, S., Capobianco, G., et al. 2019, in Society of Photo-Optical Instrumentation Engineers (SPIE) Conference Series, Vol. 11180, International Conference on Space Optics, ICSO 2018, ed. Z. Sodnik, N. Karafolas, & B. Cugny, 111803C

Chen, P. F. 2011, Living Reviews in Solar Physics, 8, 1

Chipman, E. G. 1981, ApJ, 244, L113

Colaninno, R. C. & Howard, R. A. 2015, Sol. Phys., 290, 997

Cranmer, S. R. 2009, Living Reviews in Solar Physics, 6, 3

Da Deppo, V., Chioetto, P., Andretta, V., et al. 2021, in Society of Photo-Optical Instrumentation Engineers (SPIE) Conference Series, Vol. 11852, International Conference on Space Optics, ICSO 2020, ed. B. Cugny, Z. Sodnik, & N. Karafolas, 1185210

De Leo et al. 2023, paper A, "In-flight radiometric calibration of the Metis VL channel using stars and comparison with STEREO-A/COR2 data", *in press*, A&A

De Leo et al. 2023, paper B, "In-flight radiometric calibration of the Metis UV H I Ly-α channel and comparison with UVCS data", *to be submitted*, A&A

de Wijn, A. G., Burkepile, J. T., Tomczyk, S., et al. 2012, in Society of Photo-Optical Instrumentation Engineers (SPIE) Conference Series, Vol. 8444, Ground-based and Airborne Telescopes IV, ed. L. M. Stepp, R. Gilmozzi, & H. J. Hall, 84443N

Deforest, C., Killough, R., Gibson, S., et al. 2022, in 2022 IEEE Aerospace Conference, 1–11

Dolei, S., Susino, R., Sasso, C., et al. 2018, A&A, 612, A84

Domingo, V., Fleck, B., & Poland, A. I. 1995, Sol. Phys., 162, 1

Durand, E., Oberly, J. J., & Tousey, R. 1949, ApJ, 109, 1

Fineschi, S., Casti, M., Capobianco, G., et al. 2019, 2019 IEEE 5th International Workshop on Metrology for AeroSpace (MetroAeroSpace), 309

Fineschi, S., Naletto, G., Romoli, M., et al. 2020, Experimental Astronomy, 49, 239

Fineschi, S., Romoli, M., Andretta, V., et al. 2021, in Society of Photo-Optical Instrumentation Engineers (SPIE) Conference Series, Vol. 11852, International Conference on Space Optics, ICSO 2020, ed. B. Cugny, Z. Sodnik, & N. Karafolas, 1185211

Fisher, R. R. & Guhathakurta, M. 1994, Space Sci. Rev., 70, 267

Focardi, M., Capobianco, G., Andretta, V., et al. 2014, in Society of Photo-Optical Instrumentation Engineers (SPIE) Conference Series, Vol. 9144, Space Telescopes and Instrumentation 2014: Ultraviolet to Gamma Ray, ed. T. Takahashi, J.-W. A. den Herder, & M. Bautz, 914409

Fox, N. J., Velli, M. C., Bale, S. D., et al. 2016, Space Sci. Rev., 204, 7

Frazin, R. A., Vásquez, A. M., Thompson, W. T., et al. 2012, Sol. Phys., 280, 273

Freeland, S. L. & Handy, B. N. 1998, Sol. Phys., 182, 497

Gaia Collaboration, Prusti, T., de Bruijne, J. H. J., et al. 2016, A&A, 595, A1

Gaia Collaboration, Vallenari, A., Brown, A. G. A., et al. 2022, arXiv e-prints, arXiv:2208.00211

Gan, W. Q., Feng, L., & Su, Y. 2022, Nature Astronomy, 6, 165

García Marirrodriga, C., Pacros, A., Strandmoe, S., et al. 2021, A&A, 646, A121

Gibson, S. E., Fludra, A., Bagenal, F., et al. 1999, J. Geophys. Res., 104, 9691

Giordano, S. 2023, in preparation

Giordano, S., Ciaravella, A., Raymond, J. C., Ko, Y. K., & Suleiman, R. 2013, Journal of Geophysical Research (Space Physics), 118, 967

Hayes, A. P., Vourlidas, A., & Howard, R. A. 2001, ApJ, 548, 1081

Horbury, T. S., O'Brien, H., Carrasco Blazquez, I., et al. 2020, A&A, 642, A9

Howard, R. A., Moses, J. D., & Socker, D. G. 2000, in Society of Photo-Optical Instrumentation Engineers (SPIE) Conference Series, Vol. 4139, Instrumentation for UV/EUV Astronomy and Solar Missions, ed. S. Fineschi, C. M. Korendyke, O. H. Siegmund, & B. E. Woodgate, 259–283

Howard, R. A., Moses, J. D., Vourlidas, A., et al. 2008, Space Sci. Rev., 136, 67

Howard, R. A., Vourlidas, A., Colaninno, R. C., et al. 2020, A&A, 642, A13

Howard, T. A., DeForest, C. E., Schneck, U. G., & Alden, C. R. 2017, ApJ, 834, 86

Illing, R. M. E. & Hundhausen, A. J. 1985, J. Geophys. Res., 90, 275

Inhester, B. 2006, arXiv e-prints, astro-ph/0612649v1, astro

Ivanov, V. D., Rieke, M. J., Engelbracht, C. W., et al. 2004, ApJS, 151, 387

Kaiser, M. L., Kucera, T. A., Davila, J. M., et al. 2008, Space Sci. Rev., 136, 5

Kilpua, E., Koskinen, H. E. J., & Pulkkinen, T. I. 2017, Living Reviews in Solar Physics, 14, 5

Kohl, J. L., Esser, R., Gardner, L. D., et al. 1995a, Sol. Phys., 162, 313

Kohl, J. L., Gardner, L. D., Strachan, L., Fisher, R., & Guhathakurta, M. 1995b, Space Sci. Rev., 72, 29

Kohl, J. L., Noci, G., Antonucci, E., et al. 1997, Sol. Phys., 175, 613

Kohl, J. L., Noci, G., Cranmer, S. R., & Raymond, J. C. 2006, A&A Rev., 13, 31

Koomen, M. J., Detwiler, C. R., Brueckner, G. E., Cooper, H. W., & Tousey, R. 1975, Appl. Opt., 14, 743

Koutchmy, S. & Livshits, M. 1992, Space Sci. Rev., 61, 393

Krimigis, S. M., Decker, R. B., Roelof, E. C., et al. 2013, Science, 341, 144

Krucker, S., Hurford, G. J., Grimm, O., et al. 2020, A&A, 642, A15

Landi degl'Innocenti, E. 2007, *Fisica Solare*, Springer. Firenze. 176-210

Liberatore, A., Fineschi, S., Casti, M., et al. 2023, A&A, 672, A14

Liberatore, A., Fineschi, S., Casti, M., et al. 2021, in Society of Photo-Optical Instrumentation Engineers (SPIE) Conference Series, Vol. 11852, International Conference on Space Optics, ICSO 2020, ed. B. Cugny, Z. Sodnik, & N. Karafolas, 1185248

Lyot, B. 1939, MNRAS, 99, 580

MacQueen, R. M. 1974, Journal of the Optical Society of America (1917-1983), 64, 523

MacQueen, R. M., Csoeke-Poeckh, A., Hildner, E., et al. 1980, Sol. Phys., 65, 91

MacQueen, R. M., Eddy, J. A., Gosling, J. T., et al. 1974, ApJ, 187, L85

MacQueen, R. M., Gosling, J. T., Hildner, E., et al. 1976, Philosophical Transactions of the Royal Society of London Series A, 281, 405

Maksimovic, M., Bale, S. D., Chust, T., et al. 2020, A&A, 642, A12

McComas, D. J., Angold, N., Elliott, H. A., et al. 2013, ApJ, 779, 2

Mihalas, D. & Binney, J. 1981, Galactic astronomy. Structure and kinematics

Moses, J. D., Antonucci, E., Newmark, J., et al. 2020, Nature Astronomy, 4, 1134

Müller, D., Marsden, R. G., St. Cyr, O. C., Gilbert, H. R., & Solar Orbiter Team. 2013, Sol. Phys., 285, 25

Müller, D., Nicula, B., Felix, S., et al. 2017, A&A, 606, A10

Müller, D., St. Cyr, O. C., Zouganelis, I., et al. 2020, A&A, 642, A1

Newkirk, Gordon, J. & Eddy, J. A. 1962, S&T, 24, 77

Noci, G., Kohl, J. L., & Withbroe, G. L. 1987, ApJ, 315, 706

Owen, C. J., Bruno, R., Livi, S., et al. 2020, A&A, 642, A16

Parenti, S. 2014, Living Reviews in Solar Physics, 11, 1

Pesnell, W. D., Thompson, B. J., & Chamberlin, P. C. 2012, Sol. Phys., 275, 3

Quémerais, E. & Lamy, P. 2002, A&A, 393, 295

Rochus, P., Auchère, F., Berghmans, D., et al. 2020, A&A, 642, A8

Rodríguez-Pacheco, J., Wimmer-Schweingruber, R. F., Mason, G. M., et al. 2020, A&A, 642, A7

Romoli, M., Antonucci, E., Andretta, V., et al. 2021, A&A, 656, A32

Romoli, M., Capobianco, G., Da Deppo, V., et al. 2007, in ESA Special Publication, Vol. 641, Second Solar Orbiter Workshop, ed. E. Marsch, K. Tsinganos, R. Marsden, & L. Conroy, 79

Romoli, M., Frazin, R. A., Kohl, J. L., et al. 2002, ISSI Scientific Reports Series, 2, 181

Russano et al. 2023, "Eruptive events with exceptionally bright emission in H I Ly-α observed by the Metis coronagraph", in preparation

Saito, K., Poland, A. I., & Munro, R. H. 1977, Sol. Phys., 55, 121

Shopov, Y. Y., Stoykova, D. A., Stoitchkova, K., et al. 2008, Journal of Atmospheric and Solar-Terrestrial Physics, 70, 356

Solanki, S. K., del Toro Iniesta, J. C., Woch, J., et al. 2020, A&A, 642, A11

SPICE Consortium, Anderson, M., Appourchaux, T., et al. 2020, A&A, 642, A14

Stix, M. 2002, The sun: an introduction

Stone, E. C. 1977, Space Sci. Rev., 21, 75

Telloni, D., Andretta, V., Antonucci, E., et al. 2021, ApJ, 920, L14

Thernisien, A. F., Morrill, J. S., Howard, R. A., & Wang, D. 2006, Sol. Phys., 233, 155

Thompson, W. T. 2009, Icarus, 200, 351

Tripathi, D., Chakrabarty, D., Nandi, A., et al. 2022, arXiv e-prints, arXiv:2212.13046

van de Hulst, H. C. 1950, Bull. Astron. Inst. Netherlands, 11, 135

Vásquez, A. M., van Ballegooijen, A. A., & Raymond, J. C. 2003, ApJ, 598, 1361

Webb, D. F. & Howard, T. A. 2012, Living Reviews in Solar Physics, 9, 3

Wenger, M., Ochsenbein, F., Egret, D., et al. 2000, A&AS, 143, 9

Willis, A. J. 2013, in Organizations, People and Strategies in Astronomy Vol. 2, ed. A. Heck, Vol. 2, 395–416

Withbroe, G. L. 1972, Sol. Phys., 25, 116

Withbroe, G. L., Kohl, J. L., Weiser, H., & Munro, R. H. 1982, Space Sci. Rev., 33, 17

Yashiro, S., Gopalswamy, N., Michalek, G., et al. 2004, Journal of Geophysical Research (Space Physics), 109, A07105

Zouganelis, I., De Groof, A., Walsh, A. P., et al. 2020, A&A, 642, A3

Acknowledgements

Time to write the *Acknoledgements*...
It is a nice part of the thesis because it makes me remind of this long journey that was my PhD, but on the other hand, it's difficult to express my gratitude with few words to all the people that were beside me during this journey.

I start by thanking my many supervisors: Prof. Francesca Zuccarello, Prof. Marco Romoli, Dr. Daniele Spadaro and Dr. Luca Teriaca. I thank you all for your guidance, support and encouragement throughout my PhD, also during the difficult period of the pandemic. Working with you made me grow significantly as a scientist and this is precious.

Many thanks go to my TAC member Dr. Regina Aznar Cuadrado for her kindness and availability and to both the coordinators of the PhD program, Prof. Sebastiano Albergo (UNICT) and Dr. Sonja Schuh (IMPRS). Sometimes it has been hard to conciliate the requirements of the Ph.D. of two different countries, but thanks to your help I am convinced that it was worth it and a great enrichment.

I would like to thank my colleagues in Arcetri and the ones from the Metis group. Their expertise and support have been important for this work. Furthermore, feeling part of this group was really helpful when I had to move from Florence to Göettingen and it was still Covid-19 time.

New and old friends have always had a special place in my life and of course they deserve to be mentioned here for their constant and reliable presence and for their ability to cheer me up in the worst moments. I would like to thank the other PhD students in Catania and at MPS who helped me live these PhD years more joyfully.

A special thank goes to MegaGAUSS, the institute band: sometimes band dramas pop

out but we all know that music is passion! I feel honored to sing for you and I'm going to miss you terribly when I will leave Göettingen.

Un ringraziamento speciale va al mio amore Bernhard che mi rende profondamente felice finalmente, dopo tanti anni tristi. Ringrazio anche la sua famiglia per averlo cresciuto così.

Un altro profondo grazie va a mio fratello Dario, alla mia cognata Ella e alla piccola Alessia che sono la mia allegria quando torno a casa. Allo stesso modo ringrazio tutta la mia famiglia e gli amici di famiglia, che mi hanno supportata affettuosamente e che hanno sempre trovato il tempo di vedermi tutte le volte che sono tornata a Firenze.

Il ringraziamento più grande me lo tengo per la fine e va al mio babbo Aldo e a mia mamma Sonia, che mi hanno cresciuta libera e mi hanno insegnato a lavorare e a lottare per inseguire i miei sogni.